Graphene derivatives for Li-ion batteries

Niranjala Roshani Fernando

The thesis is submitted in partial fulfilment of the requirements of the Faculty of Science and Technology, Bournemouth University for the degree of Doctor of Philosophy

March 2024

Advanced Materials Lab (AML)

Faculty of Science and Technology, Bournemouth University, UK

Copyright Statement

Reprint Permission

Reprints from published papers can be made subject to permission from the respective publishers.

Dedication

As I approach one of the most significant milestones of my academic and professional journey, the completion of my PhD dissertation, I am reminded of my incredible mother who has been my North Star throughout.

She has been my constant source of support and inspiration throughout my life's twists and turns. Despite being a single mother and raising three kids by the age of 25, she remained determined to ensure our upbringing was marked by respect and dignity. Losing her to cancer at the beginning of my PhD journey remains one of the most sorrowful days of my life.

But her amazing strength, resilience, and positivity have made me into what I am today.

I dedicate this hard-earned achievement to you Amma. I hope you are looking down upon me with tears of joy and pride at what your dear Rosi has achieved.

Forever and always, I carry your love in my heart, Mage Amma.

Abstract

The growing demand for reducing carbon footprints in today's economy underscores the urgent need to transition from fossil fuels to renewable alternatives. Depleted reserves of fossil fuels and escalating environmental concerns further highlight the necessity for viable alternatives to conventional energy sources. Among these alternatives, lithium-ion batteries have emerged as premier renewable energy reservoirs for consumer electronics, electric vehicles (EVs), and power networks due to their exceptional energy density, extended lifespan, lightweight design, and minimal maintenance requirements. However, conventional Li-ion batteries with graphite anodes fall short of meeting the escalating energy demands due to their limited nominal capacity of 372 mAh g^{-1}. To address this shortfall, there has been significant interest in replacing graphite anodes with high-capacity materials such as silicon and transition metal oxides (TMOs). Silicon possesses an impressive nominal Li-ion storage potential of 4200 mAh g^{-1}, while TMOs offer a storage capability of approximately 700 mAh g^{-1}, far surpassing that of graphite anodes. Yet, the adoption of silicon and TMOs faces significant challenges including restricted electrical conductivity, pronounced particle/electrode pulverisation during continuous lithiation/delithiation cycles, and rapid deterioration of Li-ion storage capacity. To mitigate these challenges effectively, integrating these materials with carbon nanostructures such as carbon nanofibers, graphene, and carbon nanotubes has emerged as a highly promising approach. Being highly electric conductive and mechanically robust, graphene is well-suited support for these high-capacitive materials. This PhD project introduces two graphene-based nanocomposites, graphene/NiO and graphene/Si, as

promising anode materials for Li-ion batteries, offering potential solutions to the challenges.

In **Chapter 4**, a graphene-incorporated NiO nanohybrid is introduced as an advanced anode for Li-ion batteries. The integration of graphene into NiO nanostructures is achieved through a novel one-step in situ hydrothermal process, yielding distinctive porous and conductive peony-like graphene/NiO nanohybrids. The integration of graphene enhances the current flow of NiO while also effectively regulating the restacking and aggregation of nanoparticles. Despite these advantages, practical challenges arise for NiO as a commercial anode in Li-ion batteries due to its limited availability and cost.

As an alternative system, **Chapter 5** presents an exfoliated graphene (EG) -Si nanocomposite as a commercial anodic product for Li-ion batteries. In addition to its rich presence on earth, silicon (Si) discloses the highest known gravimetric anode Li-ion storage potential of 4200 mAh g^{-1}, making it a favourable choice for Li-ion batteries. It is widely utilised as the second most used industrial anode, following graphite. However, Si encounters critical challenges with severe volume alterations during Li-ion battery charging and discharging processes, leading to poor electrochemical performances. To address these drawbacks, the study presents an EG-Si composite, where the exfoliated graphene network acts as a mechanically supportive framework for high-capacity Si electrodes. The composite enhances electrode conductivity, preserves electrode integrity, and serves as a buffer to regulate Si volume alteration throughout the cycling. The exfoliated graphene composite showed an enhanced Li-ion storage capacity compared with natural graphite. Furthermore, the study investigates the influence of the mass ratio between Si

and exfoliated graphene on the electrochemical energy storage performance to determine the optimal Si content for Li-ion batteries.

List of Publications

Journal Publications

1. **Fernando, N.,** Kannan, H., Hernandez, F.C.R., Ajayan, P.M., Meiyazhagan, A. and Abdelkader, A.M., 2023. Graphitic nanostructure integrated NiO composites for high-performance lithium-ion batteries. Journal of Energy Storage, 71, p.108015.

Supplementary Journal Publications

2. **Fernando, N.**, Veldhuizen, H., Nagai, A., Van der Zwaag, S. and Abdelkader, A., 2021. Layer-by-layer electrode fabrication for improved performance of porous polyimide-based supercapacitors. Materials, 15(1), p.4.
3. **Fernando, N.**, Chinnappan, A., Aziz, A., Abdelkader, A., Ramakrishna, S. and Welland, M.E., 2021. Flexible free-standing Ni–Mn oxide antenna decorated CNT/nanofiber membrane for high-volumetric capacitance supercapacitors. *Nanoscale*, *13*(45), pp.19038-19048.
4. **Fernando, N.**, Swaminathan, J., Hernandez, F.C.R., Priyadarshana, G., Sandaruwan, C., Yang, W., Karunaratne, V., Wang, Z., Amaratunga, G.A., Kottegoda, N. and Meiyazhagan, A., 2021. Pseudobrookite based heterostructures for efficient electrocatalytic hydrogen evolution. *Materials Reports: Energy*, *1*(2), p.100020.
5. Kong, L., Li, Z., Zhu, W., Ratwani, C.R., **Fernando, N.**, Karunarathne, S., Abdelkader, A.M., Kamali, A.R. and Shi, Z., 2023. Sustainable regeneration of high-performance LiCoO2 from completely failed

lithium-ion batteries. *Journal of Colloid and Interface Science*, *640*, pp.1080-1088.

Conferences Presented

1. **Fernando, N.,** Abdelkader, A., 2019. Hydrothermal growth of Iron titanate (Fe2TiO5) nano-flowers from natural ilmenite. SciTech PGR Conference 2019, Bournemouth University (UK).
2. **Fernando, N.,** Veldhuizen, H., Abdelkader, A and Van der Zwaag, S, 2020. A novel polyimide porous organic polymer for high-energy supercapacitors. Graphene 2020, June 02-05 Grenoble, France.
3. **Fernando, N.,** Abdelkader, A, 2023.The mobility revolution: Next-generation Li-ion battery materials. 14th Annual Postgraduate Research Conference at Bournemouth University, UK.
4. **Fernando, N.,** Abdelkader, A, 2023.The mobility revolution: Next-generation Li-ion battery materials. SciTech PGR Research Festival at Bournemouth University, UK.
5. **Fernando, N.,** Meiyazhagan, A and Abdelkader, A, 2023. NiO-anchored expanded graphite nanoflowers for high-performance lithium-ion batteries. Materials Today Conference 2023, 2nd to 5th August 2023, Singapore Expo, Singapore.

Table of Contents

List of Figures

List of Tables

Nomenclature

EV Electric vehicle

PHEVs Plug-in hybrid electric vehicles

CB Carbon black

EG Exfoliated graphene

NPs Nanoparticles

CE Coulombic efficiency

ICE Initial coulombic efficiency

N/P ratio- capacity ratio between the negative and positive electrodes

CNTs Carbon nanotubes

TMOs Transition metal oxides

CV Cyclic voltammetry

GCD Galvanostatic Charge/Discharge

CVD Chemical vapour deposition

rGO Reduced graphene oxide

LIBs Lithium-ion batteries

SEI Solid electrolyte interphase

SEM Scanning electron microscopy

EIS Electrochemical impedance spectroscopy

TEM Transmission electron microscopy

EDX Energy dispersive X-ray

XRD X-ray diffraction

Acknowledgements

I wish to extend my sincere gratitude to Dr. Amor Abdelkader for entrusting me with this research opportunity. His continuous guidance and support have been invaluable to me. Especially during challenging times with my health, his assistance has meant a great deal. I am confident that the experiences I have gained under his mentorship will continue to positively influence all areas of my life.

Furthermore, I extend my heartfelt appreciation to my industrial supervisors, Dr. Sai Shivareddy, Dr. Fengming Liu, and Dr. Anna Motta, whose invaluable contributions in industrial training and technical guidance.

I want to convey my appreciation to Mr. Robert Gardiner, manager of the Design & Engineering Innovation Centre at Bournemouth University, for his persistent support in the laboratory.

I also extend special thanks to Naomi Bailey, our doctoral school research administrator, for her kind support and understanding during challenging times. Furthermore, I am immensely grateful to Bournemouth University, UK, and Talga Technologies Limited for their generous funding of this research endeavour.

Lastly, I wish to convey my utmost respect and gratitude to my precious family, friends, and colleagues for their selfless and unwavering support, motivation, and encouragement throughout this journey.

Declaration of Authorship

I declare that the contents of this dissertation are original and have not been submitted, in full or in part, for consideration for any other degree or qualification, either at this university or elsewhere, unless explicitly stated otherwise. This dissertation reflects my own work, and any contributions made in collaboration with others are duly acknowledged within the text.

Niranjala Roshani Fernando

19/03/2024

Chapter 1 Introduction

1.1 Motivation

Energy consumption has evolved throughout human history, progressing from the firewood era to the coal era and ultimately reaching the modern fuel era. However, hydrocarbon fuel sources have drawn worldwide attention due to their adverse consequences on the environment, inclusive of pollution and global warming. Additionally, the increasing demand for energy supply has exacerbated these concerns, further highlighting the need for alternative solutions. Moreover, the reliance on traditional energy sources has resulted in a surging price trend, compounding the urgency to explore and adopt more sustainable options. A growing awareness of renewable energy sources such as solar rays, breeze, and waves has already taken place (Sorensen 2004). Given the location restrictions of renewable reserves, it becomes essential to reserve sustainable energy in the form of chemical energy. This stored energy can then be efficiently transported to the desired location of consumers, where it can be converted back into electricity for use.

The battery is the most convenient and commonly used energy storage method, offering several advantages. They offer portability and convenience, allowing for flexible deployment and utilisation in various applications. Batteries excel at converting stored chemical energy into electrical energy with high efficiency. Most importantly, batteries produce no gaseous exhaust, making them environmentally friendly and contributing to cleaner energy consumption (Diouf and Pode 2015; Amrouche et al. 2016).

The history of batteries dates back approximately 200 years. In 1792, Alessandro Volta invented the first galvanic battery, often called ‘Volta's pile’ (Pancaldi 2005). In 1836, John Daniell invented the Daniell cell, which marked the next major advancement in battery technology (Huggins and Huggins 2010). As the first commercially viable electrochemical battery, Daniell's cell is considered a milestone. Another significant breakthrough in battery technology came from the French scientist Gaston Planté in 1859 (Kordesch 1977). Planté invented the earliest secondary cell for commercial use, also acknowledged as a rechargeable lead-acid battery. In the late 1970s, a significant milestone in battery technology was reached with the creation of the earliest lithium-ion battery (LIB) by academics at Oxford University in the UK (Dell and Rand 2001). The early 1990s witnessed the initial commercialisation of LIBs by Sony, leading to remarkable success in portable electronic device applications (Li et al. 2018).

1.2 Lithium-ion batteries and anode materials challenge

In recent decades, there has been a growing interest in the progress of high-energy Li-ion batteries (LIBs) primarily since their rising applications in electric vehicles (EVs), hybrid electric vehicles (HEVs), and plug-in hybrid electric vehicles (PHEVs) (Dubarry et al. 2011; Duan et al. 2020). Additionally, LIBs have seen a surge in production because of pressing concerns such as global warming, diminishing oil reserves, and the urgent necessity to substitute fossil fuels with clean, sustainable energy sources. It is anticipated that battery-

powered vehicles are expected to replace fossil fuels in the near future (Handwerker et al. 2021).

Lithium-ion batteries surpass other commercially existing batteries in terms of energy density, service life, and weight, making them the top performers in the energy storage market (Li et al. 2018). However, the advancement of lithium-ion batteries is an ongoing process and significant challenges lie in the cost, power/energy density, and service life. The extraordinary power characteristics of Li-ion batteries enable fast charging, while their high energy density contributes to extended range, both of which are crucial factors for the replacement of energy modules in EVs and electronic devices.

Nevertheless, modern technology may face limitations in meeting the market demand, resulting in a growing need to develop new Li-ion battery (LIB) systems that offer superior characteristics. For instance, the demand in the market for Li-ion batteries featuring Si/NMC 811 chemistry exceeds specifications such as a discharging rate of over 10C, a charging capacity of at least 5C, an energy density of 350 Wh/Kg, and a cycle life of 1000 cycles with 80% capacity retention. Meeting these targets poses significant challenges, attributed to the limitations of the electrode's active components, with particular emphasis on the significance of anode materials.

Anode materials have a major impact on the energy density, service life, and safety aspects of the battery. The anode, or negative electrode, stores and releases lithium ions during charge and discharge cycles. Graphite stands out as the most widely employed anode material because it has stable cycling characteristics, demonstrated by achieving up to 3500 cycles with NMC 622 and is relatively inexpensive, priced between $10 and $20 per kilogram.

However, the nominal energy density of graphite is only 372 mAh g^{-1}, which falls considerably below the market demand for anode half-cell capacity, set at over 1000 mAh g^{-1} at C/10 rate (Zhang et al. 2021; Zhao et al. 2022).

The primary challenge in lithium-ion battery materials lies in discovering anodes capable of storing more lithium ions without compromising their structural integrity. Promising candidates for achieving higher energy density include silicon and transition metal oxide-based anode materials, such as those derived from nickel, niobium, tin, manganese, and titanium. These materials exhibit exceptional nominal capacities, making them highly desirable for enhancing battery performance (Zhu et al. 2022).

1.3 Scope

In materials science, innovative materials for advanced Li-ion batteries have consistently been a major focus. As high-capacitive anode materials, NiO and Si are promising for modern-day LIBs due to their remarkable nominal energy storage capabilities of 710 and 4200 mAh g^{-1}, respectively (Dash and Pannala 2019; Liu et al. 2022). The utilisation of pristine NiO and Si as anodes for LIBs has proven to be ineffective due to several factors. Firstly, their insulation nature limits their electronic conductivity, resulting in poor performance as anodes. Additionally, these materials experience substantial volume alterations throughout continuous lithiation/delithiation cycles, leading to mechanical stress and structural instability within the battery. This ultimately causes severe capacity decay over time, further diminishing their effectiveness as LIB anodes (Gu et al. 2015; Fu et al. 2020).

There are two commonly used approaches for enhancing the performance of these materials. Nanostructured materials can be used to shorten the electronic and ionic transport pathways. This strategy can facilitate faster electron and ion movement within the electrode (AbdelHamid et al. 2022). Although nano-size structures can effectively reduce the Li-ion diffusion and limit particle cracking, they tend to aggregate, resulting in poor battery performance. Another technique is to encourage the Li-ion transport kinetics by incorporating conductive carbon additives such as CNTs, graphite, and graphene (De las Casas and Li 2012; Mazar Atabaki and Kovacevic 2013; Li et al. 2017b; Wu et al. 2019). The additives form a network of electron-conducting pathways, allowing for more efficient electron transport throughout the electrode.

Graphene is a single sheet of hexagonally arranged sp^2 carbon atoms and has demonstrated its effectiveness in stabilising NiO and Si materials for use in LIB anode applications (Zou and Wang 2011; Mai et al. 2012; Zhang et al. 2017b; Cen et al. 2018). Its exceptional electrical conductivity, mechanical properties, and chemical solidity contribute to enhancing the performance and stability of LIB anodes. Furthermore, graphene offers the advantage of storing a greater amount of lithium ions compared to graphite, making it a promising candidate for anodes. As a result, graphene is capable of storing lithium ions both on the surface and on its edges as well (Xu et al. 2013).

The research objectives of this thesis are to create two distinct graphene-based composite electrodes, graphene/NiO and graphene/Si to accelerate the characteristics of lithium-ion batteries. This attempt takes into consideration the following factors.

1. Hydrothermal exfoliation of graphite will be employed in an eco-friendly, scalable, and cost-effective manner for producing graphene sheets for LIBs.
2. A novel in-situ hydrothermal synthesis approach will be incorporated to prevent the severe aggregation of NiO nanostructures. This method helps to maintain the homogenous dispersion of NiO within the graphene matrix and ensures its effective integration and enhances the cycle life performance in LIBs.
3. The exfoliated graphene sheets will be used to address the significant volume changes experienced by silicon nanoparticles during cycling. By incorporating graphene, the electrical conductivity and ionic conduction of the electrode will be boosted, mitigating the negative effects of volume changes, and ultimately advancing the overall performance of the battery.

1.4 Thesis outline

This thesis comprises six chapters that are organised in the following sequence:

Chapter 1 Introduction: This chapter serves as the introductory section of the thesis. First, the motivation for the study is recognised by explaining the significance of the batteries, their historical development, and the evolution of Li-ion batteries. Next, discusses the challenges and limitations associated with traditional anode materials and emphasises the need for innovative materials that can improve the electrochemical characteristics and stability of Li-ion batteries. Finally, the chapter concludes by outlining the scope and objectives of the thesis, providing an overview of the research and the specific focus areas that will be explored throughout the subsequent chapters.

Chapter 2 Literature Review: Initially, the chapter describes the fundamentals of battery electrochemistry and then Li-ion batteries. Afterwards, Li-ion batteries are analysed regarding their structure and basic components, as well as their operation. Next, a discussion of cathode and anode electrode components for Li-ion batteries follows, which provides a basic understanding of current battery materials. Next, the synthesis techniques for graphene and its exfoliation mechanism are discussed. Finally, graphene, graphene/NiO and graphene/Si anodic substances for Li-ion batteries are examined, and their latest research achievements are discussed in detail.

Chapter 3 Fundamental Experimental Approach: This chapter describes the main material characterisation techniques utilised, such as X-ray diffraction, scanning electron microscopy, Brunauer-Emmett-Teller specific

surface area measurement, Raman spectroscopy, and transmission electron microscopy. Additionally, the preparation techniques of electrodes, assembly of Li-ion batteries (LIBs), and battery characterisation techniques are thoroughly explained.

Chapter 4 Graphene-integrated NiO for Advanced Lithium-ion Batteries: This chapter illustrates an innovative approach to incorporating graphene into NiO nanostructures, showcasing its utilisation as an advanced anode for lithium-ion batteries. The incorporation of graphene not only provides the electrode conductivity, but also improves the overall integrity of the electrodes, enhances Li-ion storage capabilities, and effectively buffers the stress experienced by NiO.

Chapter 5 Graphene Incorporated Si for Lithium-ion Batteries: A comprehensive study on the advancement of graphene/Si nanohybrid anodes for lithium-ion batteries is presented in this chapter by introducing exfoliated graphene into silicon (Si) nanoparticles. The graphene is produced through hydrothermal graphite exfoliation. The primary focus is to investigate the impact of the mass ratio between silicon and exfoliated graphene on the cell characteristics of the anode, aiming to identify the optimal Si to graphene ratio.

Chapter 6 Conclusions and Future Works: This chapter serves as the conclusion of the thesis, providing a comprehensive review of the research undertaken, highlighting the significant findings, and proposing suggestions for prospective research field.

Chapter 2 Literature Review

2.1 Battery chemistry fundamentals

The battery works as an electrochemical device that transfers chemical energy into electrical energy. This process entails the transfer of electrons from materials through an electric circuit. A classic battery cell entails four essential components such as electrodes (negative anode and positive cathode), a separator, an electrolyte, and an enclosure. Negative and positive electrodes are positioned closely together to minimise the cell's internal resistance. The separator is a thin, non-conductive, porous, and insulating substance that plays a key role in isolating the electrodes from each other, preventing a short circuit. The pores of the separator are soaked with electrolytes, allowing ions to move through (See **Figure 2.1**) (Dell and Rand 2001).

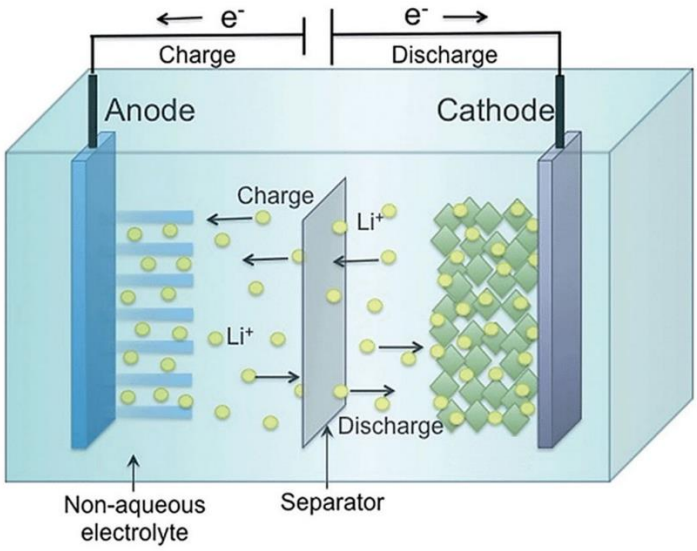

Figure 2.1 Schematic of the Lithium-ion battery.

Adapted from (Zhang et al. 2018).

Chemical reactions take place between the two electrodes, resulting in electrical energy. The materials contribute to the chemical reactions referred as active materials and play a key responsibility in storing and releasing energy during the battery's operation. Each electrode experiences a half-cell reaction, and they are driven by the deviation in electrode potential between the electrodes. The electrode in one half-cell undertakes oxidation, releasing electrons and generating positively charged ions, while the electrode in the other half-cell experiences reduction, receiving electrons and generating negatively charged ions. When the process occurs spontaneously, it is referred to as a galvanic cell (See **Figure 2.2(a)**). Galvanic cells are characterised by the following electrode chemistries (Dell and Rand 2001):

At the negative electrode:

$$M \rightarrow M^{n+} + ne^{-} \qquad \text{Equation 2.1}$$

At the positive electrode:

$$nX + ne^{-} \rightarrow nX^{-} \qquad \text{Equation 2.2}$$

Where: M represents a metal as demonstrated by lithium (Li) in lithium-ion batteries, X acts as an oxidizing agent, such as metal oxide in a high oxidation state, and e^{-} denotes an electron.

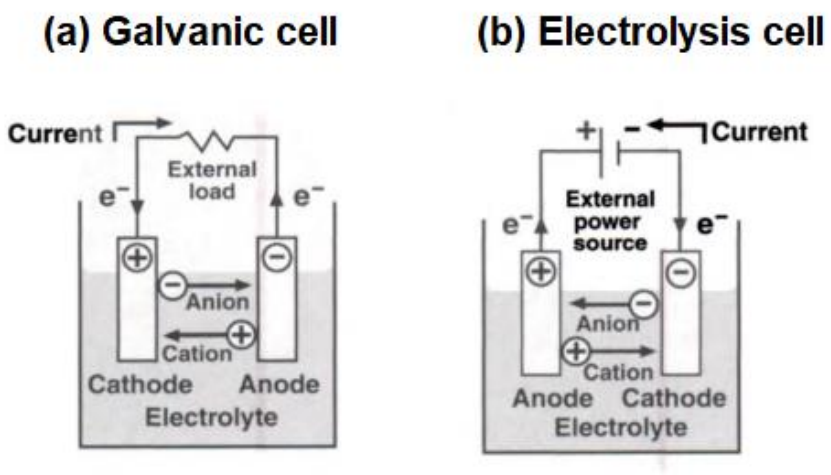

Figure 2.2 Graphic representations demonstrating the operational principles of electrochemical devices: (a) a galvanic and (b) an electrolysis. Adapted from (Amrouche et al.).

During battery discharge, the negative electrode undergoes oxidation, resulting in the loss of electrons. Simultaneously, the positive electrode experiences reduction, gaining those electrons through the external circuit. Furthermore, anions carrying negative charges migrate towards the negative electrode, while cations with positive charges migrate towards the positive electrode via electrolyte (See **Figure 2.2(a)**).

In charging, the cell transforms into an electrolysis mode, as depicted in **Figure 2.2(b)**, where the flows of electrons and ions are reversed. The charging is a non-spontaneous activity and requires an external power supply. When an exterior power source supplies a potential that exceeds the original potential, the electrolysis cell enters a charging mode. During this mode, cations migrate towards the negative end, while anions move towards the positive end of the electrodes (Dell and Rand 2001).

Battery electrodes can also be named based on the chemical processes occurring at each electrode. The electrode where oxidation occurs (release electron) is called the anode, while the electrode where reduction occurs (accept electrons) is referred to as the cathode. In batteries, that operate in discharge mode, the negative electrode is devoted to the anode, and the positive electrode is stated to the cathode (Dell and Rand 2001).

2.2 Lithium-ion (Li-ion) batteries

The lightweight nature of lithium (6.94 g mol^{-1}) and minimal nominal electrode potential (-3.045 V versus hydrogen electrode standard) make it a highly desirable material for negative electrodes in batteries. Nevertheless, the consumption of lithium metal in rechargeable batteries, particularly with liquid organic electrolytes, is constrained by significant safety concerns that arise during the charging process of the cells. During the deposition of lithium at the negative conductor, the formation and expansion of dendrites pose a significant risk of short circuits, which can subsequently result in cell failure. A battery system's safety can be further compromised by these dendritic structures, which can exacerbate the potential for thermal runaway and explosion hazards (Tarascon and Armand 2001).

In response to these safety concerns, battery researchers have made significant advancements in the progress of inherently reliable lithium-ion battery (LIB) technology. This technology involves storing lithium in the ionic state within both the negative and positive conductors of the battery. A battery system using this approach is more reliable and secure since dendrite

formation and its associated hazards are greatly reduced (Tarascon and Armand 2001; Armand and Tarascon 2008).

Sony broadcasted the first commercial lithium-ion battery (LIB) in 1991, following a series of earlier breakthroughs that involved the notable contributions of Whittingham, Goodenough, and Yazami (Whittingham 1976; Goodenough and Mizuchima 1981; Yazami and Touzain 1983; Dell and Rand 2001). During the 1970s, Whittingham demonstrated the first secondary Li-ion battery utilising metallic lithium as the negative end and TiS_2 as the positive end, resulting in a cell potential of 2V (Whittingham 1976). Building upon this progress, Goodenough and his team achieved a breakthrough by developing a rechargeable Li-ion battery with a higher energy and cell potential of 4V (Goodenough and Mizuchima 1981). The positive electrode was lithium cobalt oxide, while the negative electrode was metallic lithium. Despite this, metallic lithium negative electrodes presented safety challenges due to lithium dendrite formation during charge and discharge cycles. These dendrites could perforate the separator film of the battery, which would compromise its safety (Armand and Tarascon 2008). To address the safety concerns, Lazzari and co-authors replaced metallic lithium with lithium intercalation materials (Lazzari and Scrosati 1980). This modification helped mitigate the risks associated with dendrite growth as the intercalation materials operate at a higher potential vs. Li/Li^+(Lazzari and Scrosati 1980).

Intercalation compounds, while improving safety, resulted in a reduced cell potential. To compensate for the voltage loss, academics began investigating materials with lower electrode potentials as anodes (Nagaura and Cells 1990). Because of graphite's minimal voltage of 0.2V (vs. Li/Li^+), graphite was

selected as a negative electrode (Nagaura and Cells 1990). In 1990, an enhanced electrochemical Li-ion battery was developed by employing coke as the anode, $LiCoO_2$ as the cathode, and incorporating an organic electrolyte (Nagaura and Cells 1990).

Based on these discoveries, engineers at Sony group in Japan successfully marketed Lithium-ion batteries in 1991, launching a new era for portable electronic devices and further advancements in battery technology (Dell and Rand 2001). Rechargeable lithium-ion batteries power our modern world today and are driving the transition toward a cleaner and more sustainable energy future.

2.2.1 Operating principles and battery parameters

The operational mechanism of a Li-ion battery can be written as follows (Li 2016):

Positive electrode:

$$LiCoO_2 \underset{Discharge}{\overset{Charge}{\rightleftharpoons}} Li_{1-x}CoO_2 + xLi^+ + xe^- \qquad \text{Equation 2.3}$$

Negative electrode:

$$6C + xLi^+ + xe^- \underset{Disharge}{\overset{Charge}{\rightleftharpoons}} Li_xC_6 \qquad \text{Equation 2.4}$$

Overall reactions:

$$LiCoO_2 + 6C \underset{Discharge}{\overset{Charge}{\rightleftharpoons}} Li_{1-x}CoO_2 + Li_xC_6$$ Equation 2.5

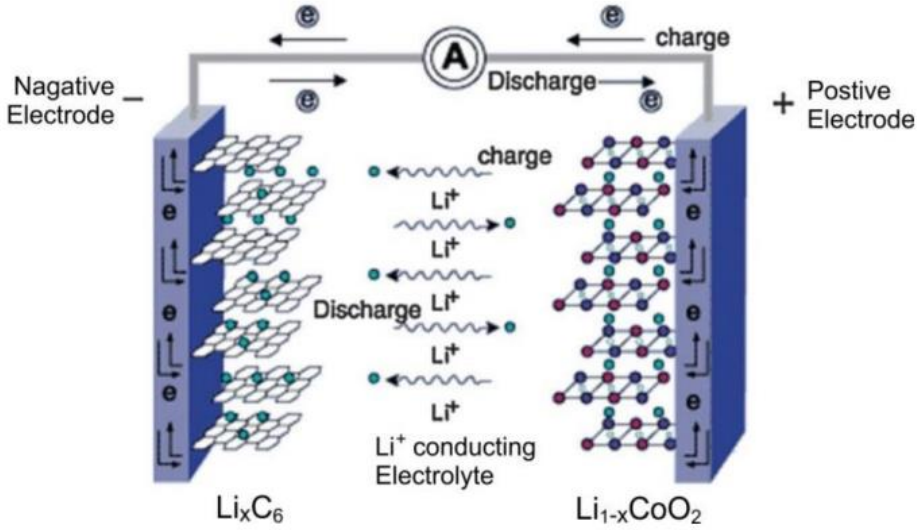

Figure 2.3 Principles of commercially available rechargeable Li-ion batteries, highlighting the movement of Li^+ ions linking the anode and cathode. Adapted from (Lu 2015; Martinet 2016).

At the charging, the cathode (positive electrode) undergoes oxidation, introducing the transfer of electrons from the positive to the negative end through an exterior circuit. Simultaneously, Li^+ ions are freed at the positive end and added to the negative end of the electrodes using an electrolyte. This process allows the battery to store energy at the negative electrode. On the other hand, during discharge, the reverse process follows, resulting in the release of the stored energy (See **Figure 2.3**).

LIBs are typically evaluated on many parameters, including capacity, mass loading, energy density, power density, cyclability, Coulombic efficiency, and safety.

Battery capacity refers to the quantity of charge that can be obtained through charging and discharging processes, while specific capacity represents the charge stored per unit mass.

The following equation can be employed to calculate the nominal capacity of a battery:

$$C_o = 26.8n\frac{m_o}{M} = \frac{1}{q}m_o\ (Ah) \qquad \text{Equation 2.6}$$

Where C_o in ampere-hours (Ah) represents the nominal capacity, m_o in grams (g) represents the active component weight involved in the electrochemical reactions, M in g/mol represents the active material molecular weight, n represents the number of electrons, and q represents the electrochemical equivalency.

Accordingly, the nominal capacity of graphite LiC_6 can be determined as follows:

$$LiC_6 \rightarrow Li^+ + C_6 + e \qquad \text{Equation 2.7}$$

$$LiC_6 = 26.8 * \left(\frac{1}{78.94}\right) * 1000 = 339.50\ mAh/g \qquad \text{Equation 2.8}$$

The practical battery capacity at a constant current can be estimated utilising the following equation:

$$C = I * t$$ Equation 2.9

Where C in ampere-hours (Ah) represents the charge/discharge Li-ion storage potential, I is in amperes (A) represents the constant current employed to the battery, and t is the charge/ discharge time in hours.

In certain applications with limited physical space, high power density requirements, and a focus on lightweight design, the volumetric Li-ion storage potential or capacity (mAh cm^{-3}), which represents the quantity of charge stored per unit volume, takes priority over the gravimetric Li-ion storage potential or capacity (mAh g^{-1}).

Mass loading indicates the amount of active material present per unit area of the electrode (mg/cm^2). Mass loading can impact the overall performance and characteristics of the battery, such as capacity, safety, and service life.

The specific energy density (specific energy) of a cell can be explained in two different terms. Gravimetric energy density discusses the amount of energy accumulated per unit mass and is denoted in Wh/kg. In contrast, volumetric energy density is relative to its volume and explained in Wh/L.

$$E = \frac{V * Ah}{M}$$ Equation 2.10

Where, E, specific energy density is in Wh/kg or Wh/L, V is nominal voltage in V, Ah is rated battery capacity and M is battery weight or volume.

The specific power density (specific power) of a battery explains how rapidly energy can be released, rather than how much energy it can store. Power density discusses the power yield per unit volume of a system or device (W dm^{-3}), while specific power discusses the power yield per unit mass (W kg^{-1}).

$$P = \frac{V*A}{M} \qquad \text{Equation 2.11}$$

Where P is specific power density in W/kg or W/L, V is nominal voltage in V, A is current, and M is battery weight or volume.

Coulombic efficiency (CE) is stated as the ratio of lithiation to delithiation capacities. In many cases, due to side reactions between the anode material and the electrolyte, the first-cycle CE tends to be lower. This is especially noticeable in high-capacity anode materials, which possess a large surface area, contributing to the reduced first-cycle CE (Xiao et al. 2020).

Cycle life refers to the competence of a battery to undergo repeated charge and discharge cycles while maintaining its electrochemical performance. It is a critical consideration in determining the commercial viability of the battery. The cycle life requirements for LIBs typically vary depending on the specific application. For instance, LIBs used in portable electronic devices are expected to maintain a stable capacity for around 300 to 1000 cycles (Nishijima et al. 2014). On the other hand, electric vehicles and industrial applications

demand much higher cycle life, often requiring batteries to endure thousands of charge and discharge cycles(Karden et al. 2007).

Li-ion battery cycle life is influenced by many factors, including state of charge (SOC), depth of discharge (DOD), operating temperature, and battery chemistry. Minimizing extreme SOC swings and avoiding deep DOD cycles can help increase the service life of the battery. Additionally, it is important to prevent exposure to high temperatures, as elevated temperatures can accelerate capacity degradation and reduce the cycle life. Furthermore, low-temperature charging can lead to the establishment of lithium dendrites on graphite anodes, which should be avoided to maintain the battery's cycle life and safety (Xiao et al. 2020).

C-rate is used to express the charging or discharging rate of an electrochemical cell. In this context, C represents the nominal or nominal charge capacity in ampere-hours (Ah), while Δt typically denotes the time interval in hours. The C-rate used in this study represents the flow of current required for a cell to reach its full nominal charge capacity (in Ah). A 1C indicates the current intensity needed for a complete charge or discharge within an hour. As an example, C/5 is a current that theoretically allows full charge or discharge in 5 hours.

The **safety** of LIBs is a vital aspect of large-scale functions, particularly for electric vehicles and grid energy systems, which require higher energies. To reduce the likelihood of accidents and minimise potential damage, a Battery Management System (BMS) has been implemented.

Numerous Lithium-ion battery accidents have been reported around the world. The Boeing 787 Dreamliner experienced a few accidents in January 2013,

most of which were caused by backup batteries. In response, the United States Federal Aviation Administration (FAA) ordered a thorough assessment of the model and manufacturing processes of the Boeing 787 to address safety concerns. Subsequently, several air companies implemented new constraints on the carrying of LIBs by the end of 2014 due to the potential safety concerns associated with them. Another notable example is the Tesla Model S electric vehicle, which encountered four critical fire incidents in 2013. These incidents were triggered by the destruction of the battery packs (Modarres 2018). Consequently, there is an increased urgency to enhance the safety of LIBs to ensure their safe and widespread use in various applications.

2.2.2 Components of Li-ion batteries

Lithium-ion batteries are composed of several constituents, such as an electrolyte, a separator, a cathode, and an anode. The anode and cathode are formed by applying materials onto copper and aluminium current collectors. Commercial lithium-ion batteries come in various shapes and sizes, such as button, cylindrical, pouch, and prismatic (See **Figure 2.4**) (Tarascon and Armand 2001).

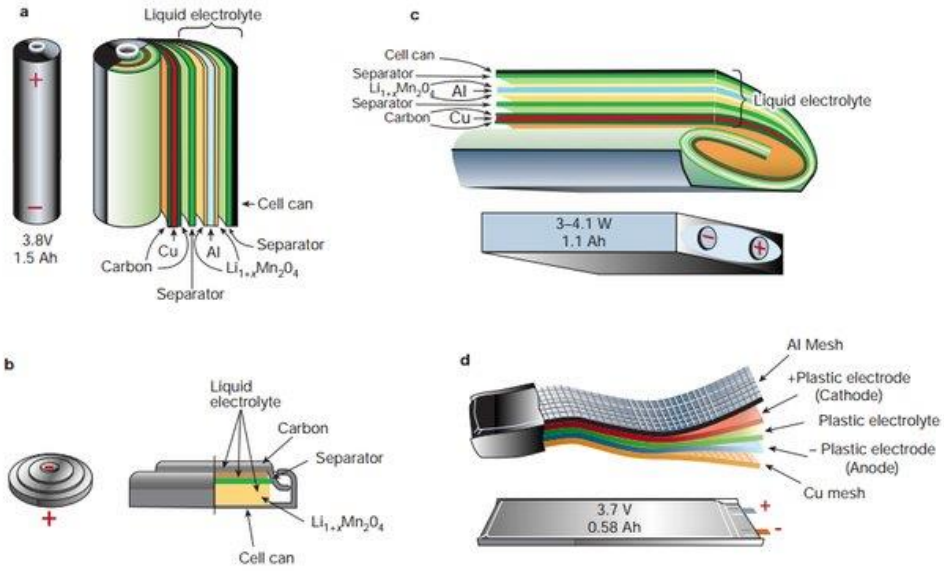

Figure 2.4 A schematic drawing illustrating the different configurations of Li-ion batteries, displaying the (a) cylindrical (b), coin (c), prismatic, and (d) thin and flat designs, along with their corresponding components.

Adapted from (Tarascon and Armand 2001).

2.2.2.1 Electrolyte

In lithium-ion batteries, the electrolyte is a Li-ion carrier that functions as both an ionic carrier and an electronic insulator. Typically, electrolytes are formulated by dissolving inorganic lithium salts in a blend of organic solvents. The electrolyte plays a centralised responsibility in ensuring battery safety and meeting battery requirements (Wakihara and Reports 2001).

The electrolyte should have a wide potential window to prevent its decomposition (Xu 2004). Lithium ionic conductivity should also be high ($\sigma Li > 10^{-4}$ S/cm) throughout the battery's operating temperature spectrum (Goodenough and Kim 2010). Additionally, electrolytes must exhibit minimal electron conduction (e < 10 S/cm) to prevent interior shorts in the battery (Goodenough and Kim 2010). Moreover, the electrolyte needs to assist in the

rapid establishment of an SEI layer on the anode surface (Xu 2004). Organic solvents, specifically carbonates, have been primarily chosen for the composition of the electrolyte due to their ability to fulfil these requirements. (Tarascon and Armand 2001; Wakihara and Reports 2001). **Table 2.1** presents a list of commonly utilised solvents and salts for Li-ion battery electrolytes (Huggins 2008; Sole 2017).

Table 2.1 Commonly used solvents and salts in Li-ion battery electrolytes.

Solvents	**Salts**
Propylene carbonate (PC)	LiPF6
Ethylene carbonate (EC)	LiClO4
Diethyl carbonate (DEC)	LiBF4
Dimethyl carbonate (DMC)	LiAsF6
Ethyl-methyl carbonate (EMC)	LiTFSi
Fluoroethylene carbonate (FEC)	LiFSi

Among these, ethylene carbonate (EC) is commonly integrated as it facilitates the SEI film establishment on the negative electrode during the initial discharge cycle.

However, recent attention has been devoted to the progress of solid electrolytes and polymer gel systems, as they seek to further improve the safety properties of electrolytes across diverse applications (Lu et al. 2023).

2.2.2.2 Separator

The efficient and safe operation of lithium-ion batteries critically depends on the separator, which plays a crucial task in physically isolating the anode and cathode. The separator's primary function involves the transport of lithium ions while preventing electrical contact that could lead to internal shorts and explosive electrolyte decomposition.

In addition to being puncture-resistant, separators must also be stable when in contact with electrolytes. Moreover, the separator's mechanical strength stands as an essential, allowing it to endure the rigidities of handling, assembly, and the expansion-contraction dynamics intrinsic to the charging and discharging cycles of cell (Gaskell 2017).

Li-ion separators play a crucial role in battery safety and performance. Typically, they require a degree of permeability, characterised by pore sizes ranging from 30 to 100 nm, coupled with a porosity of 30 to 50%. This design ensures that in the event of cell overheating, pores can close to maintain sufficient retention of liquid electrolytes.

Polyethylene (PP) and polypropylene (PE) stand out as preferred materials for separators due to their chemical inertness toward electrolytes, thermal stability (melting between 130-170°C), favourable mechanical strength, flexibility, and excellent porosity. Consequently, these materials are widely utilised in commercial Li-ion cells, either individually or as laminates. For instance, in many mobile phones and tablets, a single PE separator be sufficient. However, in the case of industrial batteries subjected to extreme temperatures and comprising multiple cells, a trilayered separator configuration has become standard practice for enhanced safety (Arora and Zhang 2004).

Figure 2.5 illustrates a common trilayered separator design, featuring a layer of PE sandwiched between PP layers (PP/PE/PP). This configuration offers added protection: when the inner polyethylene layer reaches 130°C, its pores close, while the outer polypropylene layer remains solid until 155°C. This sequential melting behaviour ensures that the PE layer closes its pores before

the PP layer, effectively interrupting current flow and strengthening battery safety.

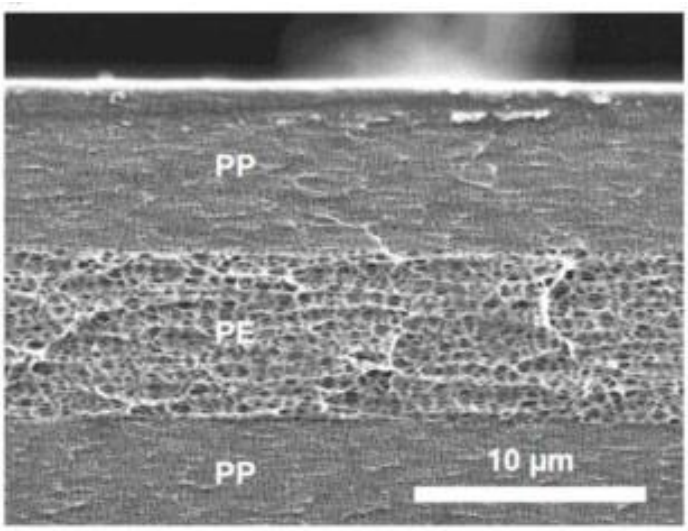

Figure 2.5 Cross-sectional scanning electron micrograph illustrating a trilayered separator (Celgard 2325) comprising PP-PE-PP layers. Adapted from (Arora and Zhang 2004).

2.2.2.3 Cathode

Battery cathodes, made from oxides of transition metals with layered structures, store and release lithium ions as they are charged and discharged. The cathode material undergoes various chemical reactions during the charge/discharge operations. A battery's cathode material significantly affects its capacity, voltage, energy density, cycle life, and overall performance.

Various materials can serve as cathodes in lithium-ion batteries, each with its characteristics and advantages. **Table 2.2** provides a comparative analysis of the electrochemical properties of commonly utilised cathode materials (Buchmann 2001; Zhao et al. 2015).

Table 2.2 A comparison of some common cathode materials.

Properties	$LiCoO_2$	$LiMn_2O_4$	$LiFePO_4$	NCA	NMC
Diffusion coefficient (cm^2/s)	10^{-10} to10^{-8}	10^{-11} to10^{-9}	10^{-11} to10^{-15}	~10^{-8}	10^{-12} to10^{-10}
Electrical conductivity (S/cm)	10^{-2} to 10	10^{-5} to 10^{-6}	10^{-8} to 10^{-9}	–	–
Average voltage (V)	3.84	3.86	3.22	3.65	3.7
Theoretical/practical capacity (mAh/g)	274/148	148/120	170/165	279/200	280/170
Specific energy (Wh/Kg)	193.3	154.3	162.9	219.8	140-180
Cycle life-graphite	500-1000	300-700	2000	500	1000-2000
C-rate graphite (charge/discharge)	1C/1C	1C/10C	1C/25C	0.7C/1C	1C/2C
Thermal runaway	150°C	250°C	270°C	150°C	210°C
Applications	Portable electronics	Power tools, medical devices	Portable and stationary	Medical devices, industrial, electric powertrain	E-bikes, medical devices, EVs, industrial

Lithium Cobalt Oxide ($LiCoO_2$):

$LiCoO_2$ (LCO) was patented by Goodenough in 1980, and its incorporation into commercial LIBs began with Sony's adoption in 1991 (Zhang and Ramadass 2012). LCO stands out due to its impressive attributes such as exceptional energy and voltage, making it a top choice for devices that require both compactness and significant capacity (Fang et al. 2005). Nonetheless, its practical application is restricted by challenges like limited availability and high cost of Co. Furthermore, concerns regarding its thermal stability and safety further impact its widespread use.

Lithium Manganese Oxide ($LiMn_2O_4$):

$LiMn_2O_4$, also known as LMO, provides benefits in terms of cost-effectiveness, reduced toxicity, and superior power output compared to LCO. Nonetheless, LMO is challenged by substantial capacity fading at elevated temperatures, along with the dissolution of manganese ions into the electrolyte (Jang et al. 1996; Ngala et al. 2004)

Lithium Iron Phosphate (LiFePO4):

LiFePO4, commonly known as LFP, is a cathode material known for its outstanding thermal stability, safety, and long cycle life. While LFP exhibits a slightly lower capacity, typically around 150-160 mAh g^{-1}, compared to certain other cathode materials, its exceptional safety characteristics have made it a preferred choice for applications demanding reliability, such as electric vehicles (Quan et al. 2022).

Lithium Nickel Manganese Cobalt Oxide (NMC):

In NMC cathodes, there are various ratios of nickel, manganese, and cobalt, such as NMC111 (equal parts of nickel, manganese, and cobalt), NMC532, NMC622, and NMC811. The NMC offers a balanced combination of energy density, cycle life characteristics, and power competence making it appropriate for a wide range of products (Nitta et al. 2015; Tran et al. 2021).

Lithium Nickel Cobalt Aluminium Oxide (NCA):

$LiNiCoAlO_2$, shares similar characteristics with NMC, including high specific energy, power and a long life expectancy making it very suitable for electric vehicles (Buchmann 2001).

2.2.2.4 Anode

The anode in a primary cell serves as the negative electrode. In the scope of LIBs, the anode can be categorised into three material classes based on their mechanisms for storing Li-ions: intercalating, alloying, and conversion.

Materials employed for intercalation and deintercalation processes incorporate carbonaceous materials and lithium titanates (LTO). In most commercial Li-ion batteries, carbonaceous anode materials take the spotlight, which includes variants such as graphite, hard carbon, soft carbon, and graphene. The widespread success of carbon-based negative electrodes can be attributed to several key factors. These include the relatively low cost of graphite, its exceptional ability for reversible lithium intercalation, rapid Li-ion intercalation kinetics, robust structural integrity, minimal side reactions with electrolytes, and its capacity to form stable solid electrolyte interface (SEI) films when interacting with various electrolyte systems (Cheekati 2011; Nitta et al. 2015; Gaskell 2017; Modarres 2018).

The intercalation/deintercalation mechanism involves the insertion of Li ions into the anode through a first-order phase transformation as explained in **Equation 2.12** (Liang et al. 2013). This process minimally alters the volume of the anode material's basic structure, leading to improved cycle life (>10000 cycles) and rate capability (>10 C).

$$MO_x + yLi^+ + ye^- \leftrightarrow Li_yMO_x \qquad \text{Equation 2.12}$$

M represents a metal.

Anode materials capable of alloying with lithium include silicon (Si) and tin (Sn). These materials engage in partially reversible electrochemical reactions with lithium, occurring at lower voltages than pure lithium itself. Notably, these

alloying reactions promise a significantly higher nominal specific capacity, with silicon (Si) offering the highest as 4200 mAh g^{-1} and tin (Sn) providing 994 mAh g^{-1}, related to the specific Li-ion capacity of intercalation-based anodes like graphite, which stands at 372 mAh g^{-1}.

The following equation represents the alloying/dealloying mechanism.

$$M + xLi^+ + xe^- \leftrightarrow Li_xM \qquad \text{Equation 2.13}$$

However, a critical drawback associated with alloying anodes is the substantial volume changes and phase transitions they undergo while accommodating lithium. During the alloying and de-alloying processes, mechanical strain is generated, leading to the electrode's cracking and disintegration. Consequently, this results in a noticeable loss of charge storage capacity after only a few cycles of use (Cheekati 2011; Nitta et al. 2015; Gaskell 2017; Modarres 2018).

Materials suitable for anodes in conversion processes encompass a diverse array of substances, including transition metal oxides, sulfides, phosphides, nitrides, and others. Theoretical capacities extend from 350 mAh g^{-1}, shown by Cu_2S, to as high as 1800 mAh g^{-1}, as evidenced by MnP_4. Despite their promising properties, these materials have not yet found a solid position in the commercial lithium-ion battery market. This is primarily due to their restricted availability, higher production cost, limited availability, lower coulombic efficiencies, and issues associated with volume changes. Moreover, a noteworthy drawback is the relatively high reaction voltage associated with most conversion metal oxide anodes, frequently exceeding 1.0 V, such as in the case of Nb-oxide. Consequently, this leads to a reduced cell voltage and a successive decrease in energy density (Cheekati 2011; Nitta et al. 2015;

Gaskell 2017; Modarres 2018).The anode resources utilised in lithium-ion batteries are outlined in **Table 2.3**, while **Figure 2.6** illustrates charge-discharge curves for several commercially available anode materials (Marka and Srikanth 2015).

Table 2.3 The anode materials for lithium-ion batteries.

Material	**Theoretical Capacity/ $mAhg^{-1}$**	**Benefits**	**Drawbacks**
Insertion type			
Graphite	372	• Low cost • High cycle life (>1000) and average power(>1C)	• Limited energy density
Graphene	744	• Low impedance	• High irreversible capacity loss
Lithium Titanates (LTO)	175	• Excellent safety • high power (>10C) and cycle life (>10 000) • Low cost	• Limited energy density
Alloying type			
Silicon **Tin** **Silicon oxide** **Tin oxide**	4200 994 1600 790	• High capacity and energy density	• High irreversible capacity loss • Poor cycle life • Large cell impedance • Poor Coulombic efficiencies • Unstable SEI layer formation
Conversion type			• High irreversible capacity loss
Metal oxides (NiO, MnO, Fe_2O_3	500-1200	• High capacity and energy density	• Poor cycle life

Nb_2O_5 etc.)	• Large cell impedance • Poor Coulombic efficiencies • Unstable SEI layer formation

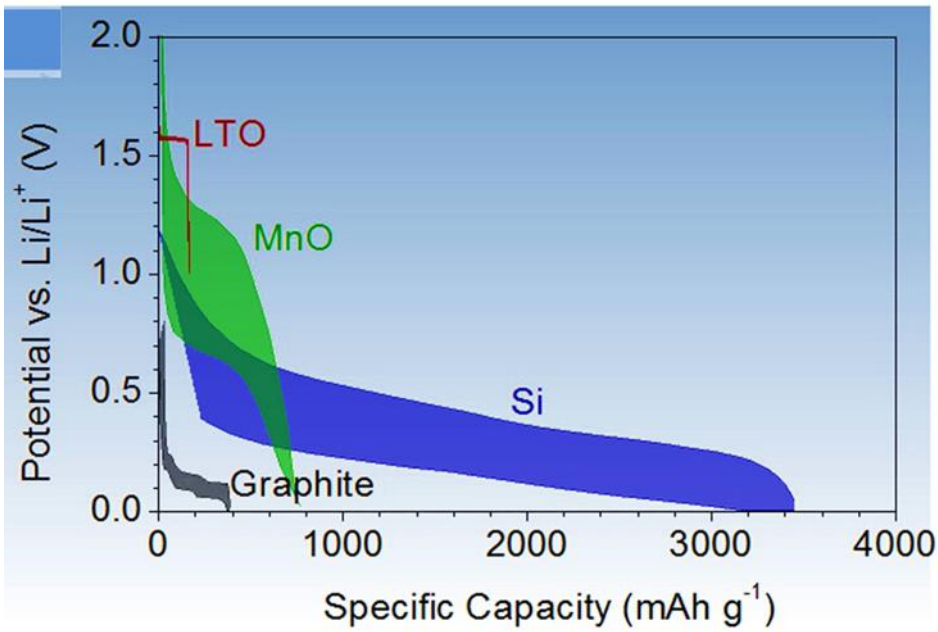

Figure 2.6 Charge–discharge profiles of common anode materials, showing voltage hysteresis.

Adapted from (Nitta et al. 2015).

In addition to the materials mentioned earlier, the idea of blending several materials appears to be the latest promising approach. For instance, modern commercial silicon-based anodes typically incorporate silicon along with one or a few of the following: graphite, graphene, carbon, or carbon nanotubes (CNTs). In this setup, silicon serves as the primary lithium-storing material, while the others act as conductive buffers. As an excellent example, commercial Amprius Si anode with conductive carbon coating stands out as

the latest breakthrough, with its highest reported cell energy density of 500 Wh/kg and discharge power of 10C (**Table 2.4**) (Amprius Technologies 2024).

Table 2.4 Comparison of conventional graphite and Amprius Si anodes.

Performance	**Graphite anode cell**	**Amprius Si anode cell**
Specific energy (Wh/kg)	~ 215-285	320-500
Energy density (Wh/L)	~530-715	805-1300
Charging time 80%	30 minutes	< 6 minutes
Cycle life	500-1000 cycles	200-1200 cycles
Operating temperature (°C)	-20 to 60	-30 to 55

2.2.2.4.1 Graphite

Graphite stands out as the top choice for anode in modern lithium-ion batteries. Its selection is primarily driven by its exceptional electrochemical properties, cost-effectiveness, and widespread availability. Despite these advantages, it's worth noting that graphitic carbon has a relatively modest theoretical lithium intercalation capacity, measuring 372 mAh g^{-1}, based on the LiC_6 stoichiometry. In contrast, lithium features a significantly higher charge density, registering 3862 mAh g^{-1}.

Graphite's structure is displayed in **Figure 2.7.**

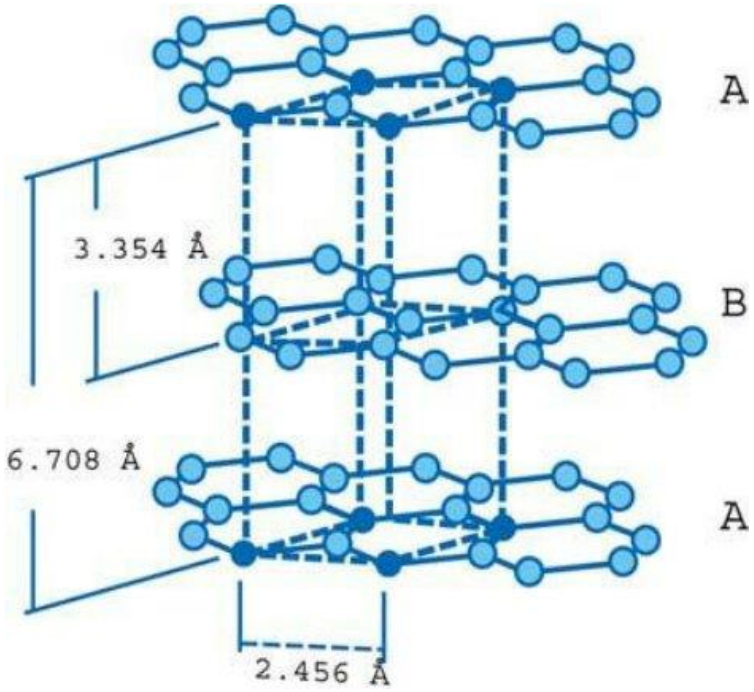

Figure 2.7 The crystal structure of graphite (15 and 16) reveals a hexagonal primitive unit cell with dimensions a = 2.46 Å and c = 6.71 Å. Within this structure, the in-plane bond length measures 1.42 Å, and each unit cell contains four atoms, denoted as A and B.

Adapted from (Celasco et al. 2019).

As a result of its unique atomic arrangement and bonding, graphite has several key structural characteristics (Celasco et al. 2019).

- Graphite is composed of layers of carbon atoms arranged hexagonally, spaced 1.42 Å apart, and these layers are separated by 3.35 Å.
- Graphitic comprises sp^2 hybridised stacked layers of carbon organised in a planar "honeycomb-like" network, forming a graphene sheet. Cohesion between these graphene sheets is facilitated by weak Van der Waals forces, giving rise to the layered structure of graphite.

- Graphite is a good electrical conductor, attributed to the existence of a delocalized valence electrons system. However, the electrical conduction is restricted exclusively to the plane of these layers.
- Within lithium-ion batteries, the crystallinity, texture, microstructure, and micro morphology of graphite has a substantial influence on both the intercalation capacity and its interaction with the electrolyte.
- Graphite powder typically exhibits a surface area of approximately 8.5 m^2/g, with a bulk density ranging between 1.3 and 1.95 g/cm^3.

The lithium storage mechanism in a graphite anode entails the intercalation and de-intercalation of Li ions, occurring within an electrode potential spectrum of 0.005 to 0.2 V versus Li^+/Li. This process results in the formation of a set of compounds known as graphite intercalation compounds (GICs). In addition, during the initial cycle, in contact with various electrolyte solutions, graphite develops a protective surface film, commonly referred to as the Solid Electrolyte Interface (SEI). This SEI film plays a pivotal function as an efficient passivation barrier on the graphite surface. Essentially, it prevents unwanted interactions between solvent molecules and their decomposition. Consequently, it facilitates the migration of lithium ions exclusively, enhancing battery performance and longevity (Cheekati 2011; Nitta et al. 2015; Gaskell 2017; Modarres 2018).

Research has been conducted over the last three decades to investigate the mechanism of graphite anodes and to boost their characteristics in Li-ion batteries (Wang et al. 2000; Aurbach et al. 2002; Yao et al. 2020). However, graphite still hampers the high-power capability, especially in fast-charging scenarios. Additionally, there's a need to improve its cycle stability and

coulombic efficiency for cost-effective, large-scale energy storage facilities. Finally, addressing safety concerns related to lithium dendrite formation through surface engineering of graphite and the utilisation of electrolyte additives is of utmost importance. These efforts are crucial for alleviating concerns about electric vehicles and extensive energy storage systems.

2.2.2.4.2 Silicon

Silicon emerges as a desirable anode option in LIBs, primarily due to its notable characteristics. Its excellent nominal Li-ion storage potential and low discharge voltage make it an appealing choice. In its fully lithiated form, denoted as $Li_{4.4}Si$, silicon creates a lithium-silicon alloy with a theoretic specific Li-ion storage potential of ~ 4,200 mAh/g, surpassing the capacities of both metallic lithium (3,600 mAh/g) and graphite (372 mAh/g) by a substantial margin (**Figure 2.8**) (Kasavajjula et al. 2007). Si, being an abundant natural material, exhibits strong electrical conductivity when doped or in a polycrystalline state. Furthermore, its electrochemical potential of formation closely resembles that of metallic lithium, enabling batteries incorporating silicon anodes to attain a notably high open circuit voltage. Lastly, silicon boasts low reactivity and low toxicity, attributes of significant importance when assessing the safety of a vehicle battery system.

Another advantageous aspect of silicon lies in its abundant natural availability, which, when doped or in a polycrystalline state, exhibits strong electrical conductivity. Moreover, its electrochemical potential of formation closely mirrors that of metallic lithium. This property enables batteries incorporating

silicon anodes to achieve a notably high open circuit voltage, a key factor in enhancing their electrochemical performance (Bourderau et al. 1999).

However, a major challenge linked to the use of bulk silicon in anodes is its substantial volume expansion of ~ 400% during the lithiation/delithiation circumstances. This drives the fracture of the anode, resulting in unrecoverable capacity loss and severe electrode degradation since the broken pieces lose electrical contact with current collectors (Bourderau et al. 1999; Wu and Cui 2012).

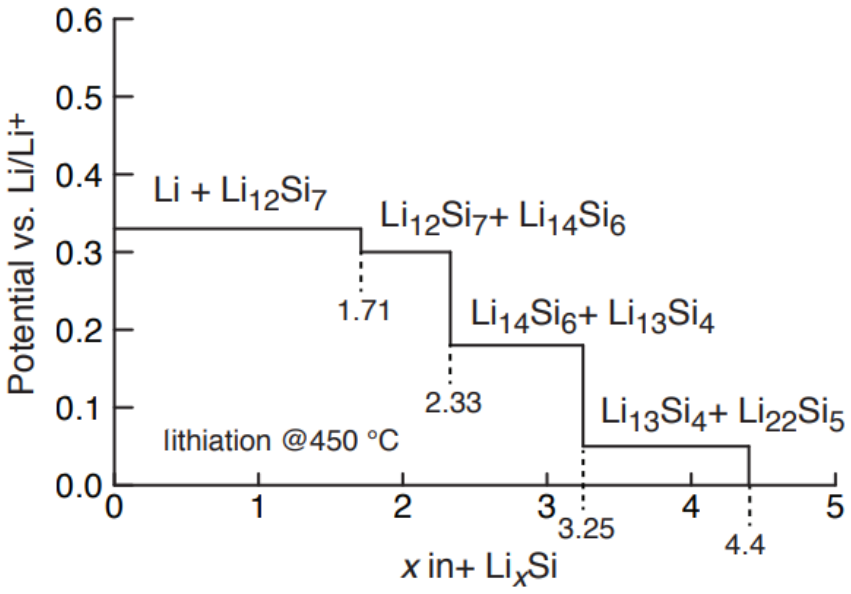

Figure 2.8 High-temperature lithiation curve of Si.

Adapted from (Wu and Cui 2012).

To address this issue and extend the cycle life of silicon-based anodes, various approaches have been proposed (Wu et al. 2019; Li et al. 2021a). These methods involve size reduction of silicon particles to the nanoscale, involving thin films, nanowires, or nanoparticles, as well as the integration of Si

nanomaterials into a carbon matrix (Wu et al. 2019). The incorporation of carbon-based materials is believed to help alleviate volume fluctuations and improve both electronic and ionic conductivities, ultimately enhancing the overall performance of the Si anode.

2.2.2.4.3 Transition metal oxides (TMOs)

Transition metal oxides (TMOs) demonstrate remarkable electrochemical performance, delivering a significant Li-ion storage potential of approximately 700mAh/g, exceptional power output capabilities (for instance, Nb_2O_5 can function at up to 30C), extended cycle life reaching 10,000 cycles, and enhanced safety due to certain metal oxides having a working potential that exceeds the lithium deposition potential (Griffith et al. 2020). Transition metal oxide-based lithium-ion cells have the advantage of having about twice the capacity of carbon per unit mass and three times its density (Zhao et al. 2016; Griffith et al. 2020). Unlike the common lithium insertion or lithium-alloying processes, the lithium storage mechanism for these metal oxides deviates, involving the synthesis and disintegration of Li_2O, accompanied by redox reactions of metal particles. To illustrate, a reversible Li-storage mechanism for NiO can be expressed as follows (Fernando et al. 2023):

Anode

$$NiO + 2Li^+ + 2e^- \leftrightarrow Li_2O + Ni$$ Equation 2.14

Cathode

$$2Li \leftrightarrow 2Li^+ + 2e^-$$ Equation 2.15

Overall

$$NiO + 2Li \leftrightarrow Li_2O + Ni$$ Equation 2.16

This process includes the reversible synthesis and decomposition of Li_2O, during which significant microstructural transformations occur, often accompanied by the recrystallization of active materials. However, despite their impressive capacity, these materials tend to experience low electronic conductivity, significant volume alterations during cycling, potential hysteresis, and lowered coulombic efficiency, typically falling below 75% (Yu et al. 2005). To address this challenge, researchers frequently utilise a composite approach involving carbon-based materials (Cao et al. 2017).

2.3 Graphene

Graphene is a hexagonal one-layer sheet of carbon atoms that has enormous potential in many scientific and technological fields (Huang et al. 2012).The two-dimensional layered arrangement of graphene is represented in **Figure 2.9**.

A single sheet of graphitic carbon known as graphene possesses numerous benefits owing to its exceptional conductivity, substantial surface area, and commendable mechanical characteristics. Specifically, graphene can accommodate a lithium atom for every three carbon atoms, thereby yielding an impressive nominal storage capability of 744 mAh g^{-1} through the formation of Li_2C_6 (Huang et al. 2012). This phenomenon can be interpreted by the adsorption of lithium ions on both sides of the graphene sheet, resembling an arrangement akin to a "house of cards" within hard carbons. Additionally,

lithium can also find storage within nano-cavities situated among the graphene nanosheets, a result of scrolling and crumpling processes.

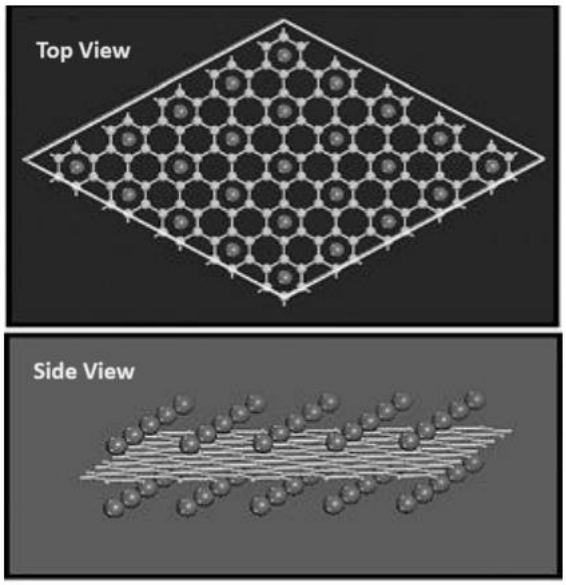

Figure 2.9 Atomic model for the LiC_3 graphene.

Adapted from (Cheekati 2011).

2.3.1 Graphene and exfoliated graphene synthesis

Graphene can be produced using various methods, which leads to different properties concerning the quality, cost, scalability, purity, and yield **Figure 2.10**.

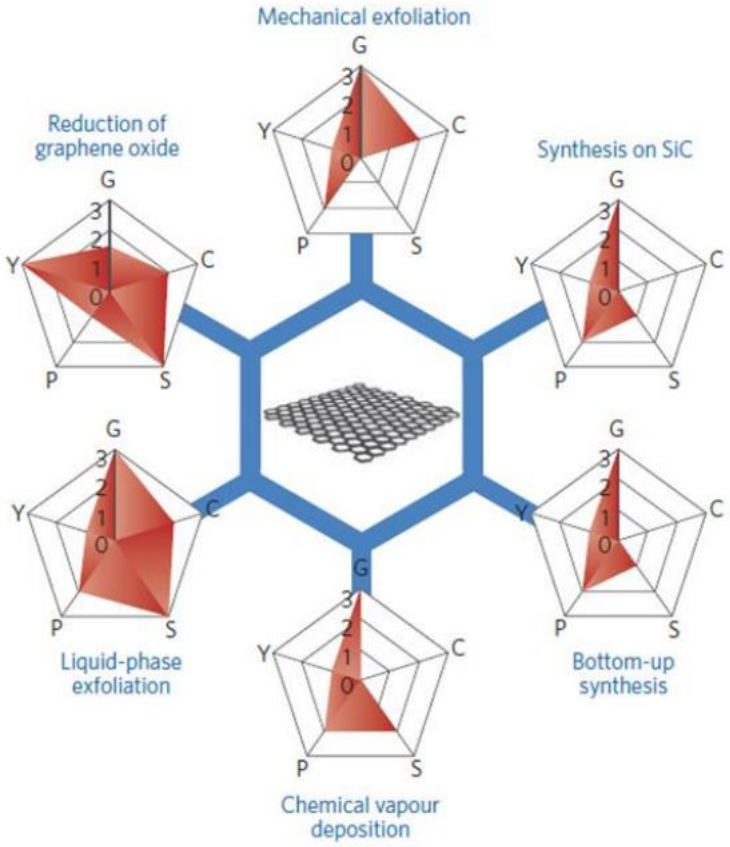

Figure 2.10 A schematic showing the common techniques of producing graphene. The assessment of fabrication processes has been conducted using a five-point criteria system, containing graphene quality (G), cost considerations (C), scalability (S), purity (P), and yield (Y). This scale ranges from 0 (indicating no relevance or applicability) to 3 (representing high significance).

Adapted from (Raccichini et al. 2015).

Mechanical exfoliation, initially used to isolate graphene, yields exceptionally high-quality and pure graphene sheets at a low cost. The process is called as 'scotch tape' technique and involves repeatedly peeling graphene layers off from graphite using adhesive tape, resulting in a single or few layers of high-

quality graphene sheets. However, the drawback lies in its low yield and the inherent lack of scalability, making it suitable primarily for fundamental research purposes (Novoselov et al. 2004).

Graphene can be produced with precise thickness control using epitaxial growth or chemical vapour deposition (CVD). Despite this, these substrate-based techniques are limited by constrained dimensions and high costs, preventing them from fulfilling the requirements for commercially viable graphene applications (Yi and Shen 2016).

Alternatively, the top-down approach involves oxidative exfoliation of graphite to obtain graphene oxide (GO), followed by chemical reduction to yield reduced graphene oxide (rGO), providing a cost-effective, efficient, and scalable production method. Nonetheless, rGO frequently exhibits reduced purity and an abundance of deficiencies and oxygen-containing edges, thereby enhancing its chemical reactivity but compromising its electrical conductivity (Wang et al. 2009; Lian et al. 2010).

By employing high-shear mixing, sonication, or a hydrothermal/solvothermal approach, liquid phase exfoliation (LPE) emerges as an innovative top-down technique for achieving a stable dispersion of defect-free monolayer or few-layer graphene, thus enhancing the clarity and smoothness of the process (Liu et al. 2014; Randviir et al. 2014). This is achieved through the application of an electrochemical or mechanical driving force to either pristine or expanded graphite, which effectively reduces the strength of Van der Waals attraction among the graphitic sheets.

In the research led by Qian and their team, they achieved the effective extraction of graphene from expanded graphite within an acetonitrile solution

through the solvothermal exfoliation method (Qian et al. 2009). Following this, the mixture was subjected to centrifugation, which resulted in the separation of monolayer and bilayer graphene sheets, varying in thickness from 0.5 to 1.2 nm.

In a separate study, researchers utilised solvothermal treatment in N-Methyl-2-pyrrolidone to demonstrate the direct transformation of pristine graphite into graphene, as illustrated in **Figure 2.11** (Tang et al. 2010). Notably, the resulting graphene maintained its inherent characteristics throughout the entire process, all without the need for any additional stabilisers or contaminants. The authors assert that the solvothermal treatment elevated both internal pressure and temperature, subsequently decreasing the free energy. This increase in temperature and pressure led to solvent molecules infiltrating between the layers of graphite, weakening the bonds holding the layers together, ultimately resulting in the successful exfoliation of the graphite.

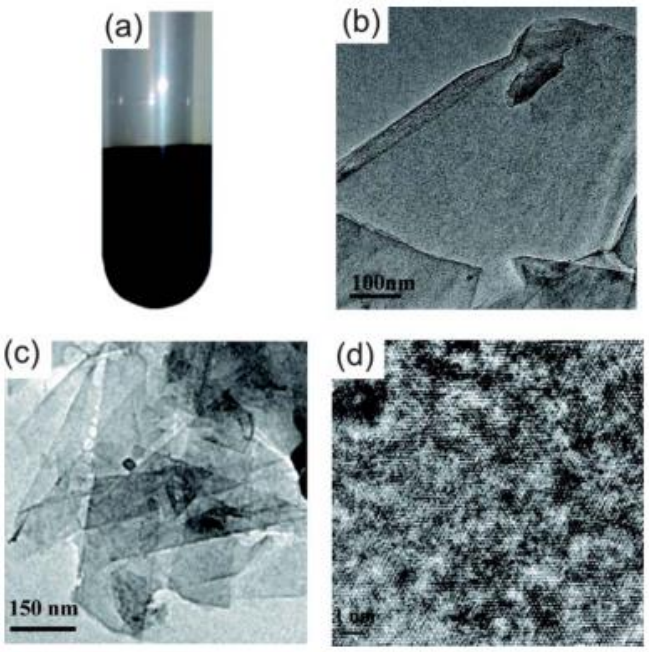

Figure 2.11 (a) Graphene suspension in NMP after thermal treatment (b) TEM micrograph of monolayer graphene (c) TEM picture of multilayer graphene sheets (d) HRTEM analysis of monolayer graphene. Adapted from (Tang et al. 2010).

In an alternative approach, Zheng and colleagues employed oleyl amine both as a solvent and as an intercalating agent for the solvothermal exfoliation of expanded graphite (Zheng et al. 2010) (**Figure 2.12**). Following dispersion and subsequent centrifugation, they successfully obtained 60% monolayer sheets, each possessing a surface area of approximately 300 mm^2. The authors attributed the intercalation of oleyl amine molecules within the expanded graphite to the ionic interactions that occurred between oleyl amine molecules, and the acidity presence in the graphitic layers.

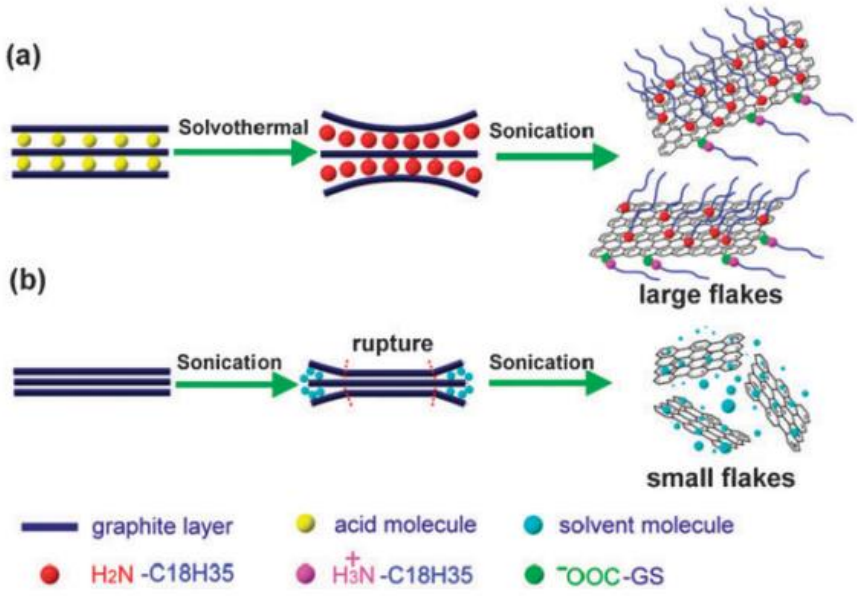

Figure 2.12 Schematic diagrams illustrating the exfoliation of graphite (a) through solvothermal aided sonication and (b) conventional sonication. Adapted from (Zheng et al. 2010).

2.3.2 Graphite to graphene exfoliation mechanism

Bulk graphite consists of parallel layers separated by 3.41 Å. The bonding between these sheets is still solid, despite their relatively poor Van der Waals attraction. Back in 1859, Brodie made a groundbreaking achievement by successfully producing the first single-layer graphene sheet through exfoliation (Brodie 1859). Since that historic milestone, numerous attempts have been undertaken to scale up graphene production, but these efforts have generally encountered significant challenges and achieved only limited success (Zhong et al. 2015).

For a successful exfoliation, it is critical to overcome the Van Der Waals attractions that exist between neighbouring graphite layers. As an example, these attractions can be mitigated by oxidation and chemical intercalation

reactions, leading to an increased separation between these layers. Since Van Der Waals forces decrease as the separation between atoms increases, this leads to a significant reduction in attraction forces. For instance, the oxidation of graphite introduces functional groups like hydroxyls and epoxides into the graphitic layers, causing the graphite's structure to become disordered and increasing the d-spacing from 3.4 Å to approximately 7.0 Å. This substantial increase in d-spacing significantly enhances the exfoliation process (McAllister et al. 2007).

Another approach to reducing the Van der Waals attractions is to immerse the graphite in a solvent, thereby reducing the energy between adjacent layers. Coleman et al. demonstrated that by aligning the refractive indices of the substances and the solvent, the potential energy can be brought close to zero (Coleman 2009). It was advised to employ solvents with a surface tension of around 40 mJ/m^2 for graphene dispersion. As a result, solvents like N-methyl-2-pyrrolidone and dimethylformamide are commonly utilised for the exfoliation of graphite.

Mechanical exfoliation methods, like ultrasonication and thermal treatment, offer effective processes to neutralise the attractive Van Der Waals interactions. Ultrasonication influences the shear forces and cavitation, which is the formation and subsequent collapse of bubbles, to induce exfoliation. On the other hand, thermal processes operate by decomposing functional groups, effectively overcoming the interaction between layers due to high pressure.

2.3.3 Graphene anode for lithium-ion batteries.

Lithium intercalation characteristics of graphite particles are significantly influenced by their dimensions. With the development of techniques for manufacturing single and few-layer graphene, numerous researchers have embarked on experiments to assess these materials as potential anode candidates for LIBs. The primary motivation compelling these investigations is the expectation that monolayer graphene could potentially double the theoretical lithium storage capacity when compared to graphite. To put it simply, if two layers of Li^+ ions were to adsorb onto each graphene sheet, this could result in the formation of Li_2C_6 rather than LiC_6, leading to a substantial increase in Li-ion storage potential from 372 mAh g^{-1} to 744 mAh g^{-1} (Nitta et al. 2015).

In a study conducted by Wang and colleagues (Wang et al. 2009), graphene nanosheets were generated in large quantities through a modified version of the Hummer's method. These nanosheets displayed impressive Li-ion battery performances, including a first Li-ion storage of 945 mAh g^{-1} and a reversible energy of 650 mAh g^{-1}. Notably, even after undergoing 100 cycles, the graphene anode preserved a Li-ion storage capability of 460 mAh g^{-1}, surpassing traditional graphite anodes (**Figure 2.13**). This underscored the enhanced lithium storage potential of these nanosheets in lithium-ion cells, showcasing remarkable cyclic performance.

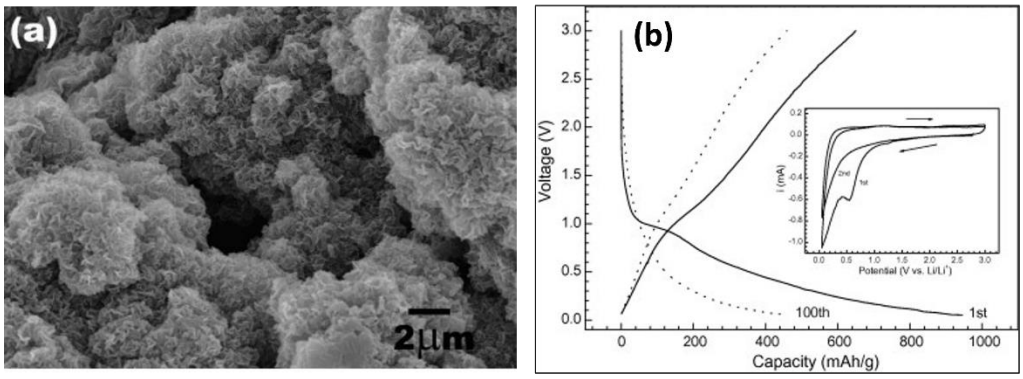

Figure 2.13 (a) Low magnification FEG-SEM observation of graphene nanosheets (b) Lithiation/delithiation patterns of graphene nanosheets and the inset showing the cyclic voltammograms.

Adapted from (Wang et al. 2009).

In a separate study, Peichao Lian and his research team (Lian et al. 2010) produced characteristic graphene sheets by initially subjecting graphite to an oxidation process and subsequently performing instant thermal enlargement in a nitrogen atmosphere. The resulting graphene sheets exhibited a unique curled morphology, resembling thin, crinkled paper-like structures, and featured only a few layers as shown in **Figure 2.14**.

Remarkably, these graphene sheets possessed a substantial specific surface area, measuring 492.5 m^2/g. What's particularly noteworthy is that their initial discharge and charge energies were exceptionally high, reaching 2035 mAh g^{-1} and 1264 mAh g^{-1}, respectively. Graphene sheets with fewer layers exhibit a significantly greater reversible Li-ion storage in comparison to their abstract Li-ion storage capability of 744 mAh g^{-1} (Khan et al. 2023). It is widely recognised that disordered carbon materials, like graphene, have the potential to achieve higher capacity values in contrast to graphite.

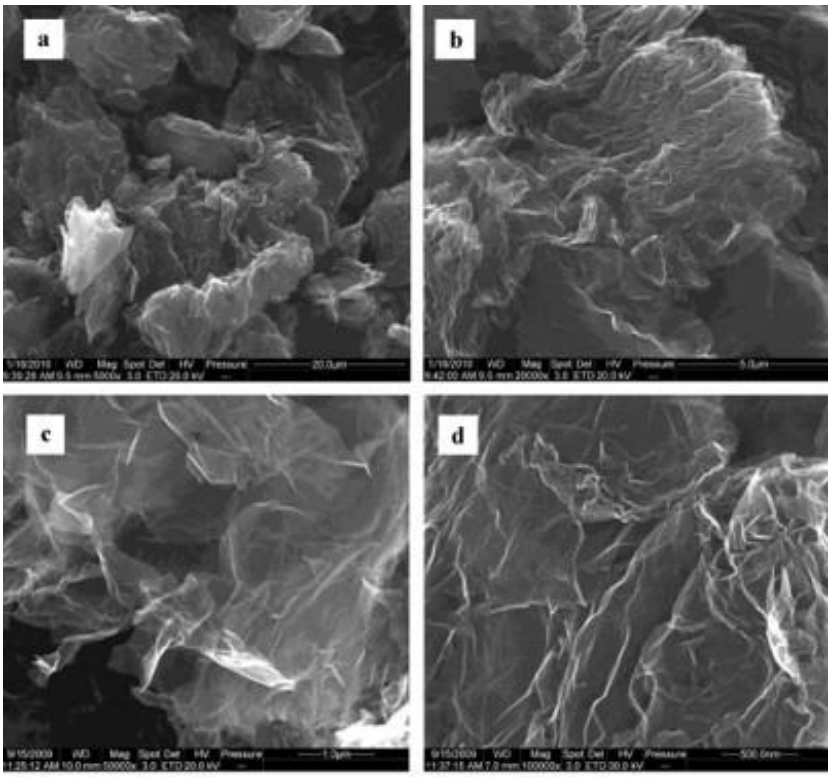

Figure 2.14 SEM observation of graphene sheets: (a and b) low-magnification, (c and d) moderate-magnification.

Adapted from (Lian et al. 2010).

Graphene sheets with fewer layers may possess this superiority because of their larger surface area and unique curled morphology, which provide an abundance of active sites for lithium insertion, including edge-type sites and nanopores (Concheso et al. 2006; Khan et al. 2023).

In a similar study, Ye and colleagues presented a binder-free anode structure comprising graphene-on-graphene, showcasing initial discharge/charge capacities of 2556.4 and 1218.6 mAh g^{-1} respectively. However, a notable 52.3% loss in capacity occurred during the first formation cycle due to SEI formation. Conversely, remarkable initial capacities of graphene were attributed to the presence of oxygen-related groups, which induce additional structural defects facilitating enhanced lithium-ion storage (Ye et al. 2014a).

Nonetheless, an extensive analysis carried out on graphene-based substances for lithium-ion batteries demonstrated that pure graphene did not perform as anticipated in practical applications (Raccichini et al. 2017). For example, the chemically reduced graphene (rGO) frequently exhibited low purity, numerous defects, and oxygen-holding areas. These characteristics increased the material's chemical reactivity with the electrolyte while simultaneously lowering its electrical conductivity. Additionally, the significant initial lithiation capacities were discovered to be irreversible and connected to the specific surface area. These factors, combined with the low packing density of graphene, impose limitations on the feasibility of using only graphene as the active material in the battery's anode (Sole 2017).

A more promising approach involves the integration of graphene as a conductive scaffold within composites or hybrids, alongside other active materials, to create an assembly for LIBs that offer enhanced Li-ion storage potential, extended lifespan, and rapid charging/discharging capabilities. Graphene serves as a platform for anchoring electrochemically active substances, such as transition metal oxides and sulphides (e.g., NiO, SnO, and SnS_2), as well as materials with Li-ion storage mechanisms based on alloying/dealloying, such as Si and Sn (Chang et al. 2012; Beck et al. 2014; Deng et al. 2016; Gaskell 2017; Sundar et al. 2023).

This enrichment in the electrochemical performance through the assembly can be credited to several factors:

- Flexible graphene sheets prevent the detachment, aggregation, and pulverization of nanoparticles during repeated lithiation and delithiation processes.

- Graphene's outstanding electron conductivity ensures effective electrical connectivity of the nanoparticles.
- The active material distributed on the graphene sheets not only prevents their restacking but also maintains their high surface area, a crucial factor for achieving optimal performance.

In composites, graphene and active nanoparticles work together to enhance each other's properties. Graphene can be employed in several configurations, as demonstrated in **Figure 2.15**: encapsulating nanoparticles, blending them, anchoring them onto graphene sheets, stacking them in a sandwich-like arrangement, or layering them between graphene sheets (Wu et al. 2015).

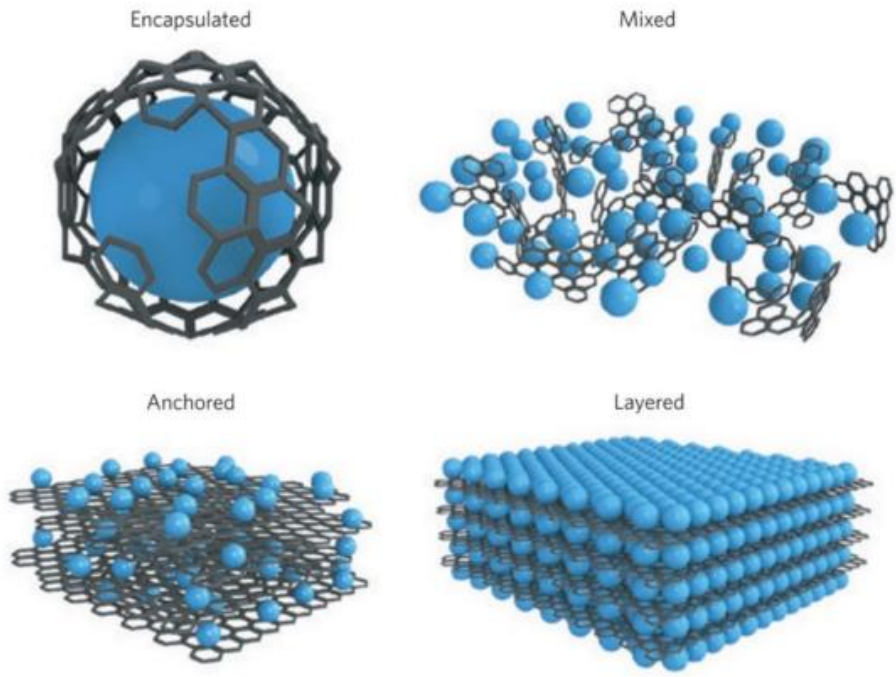

Figure 2.15 Schematic illustrations depicting graphene composite materials with varied structures.

Adapted from (Wu et al. 2015).

2.4 Graphene/NiO anode for Li-ion batteries

Transition metal oxides (TMOs), including oxides of Co, Ni, Fe, Cu, Ti, and Zn, have garnered substantial interest in research as viable alternatives to graphite (Zhu et al. 2022). Beyond their non-toxic nature, these materials possess high power and energy densities and are readily available, all while being cost-effective to manufacture, making them an appealing choice as anode materials. Furthermore, the utilisation of TMOs as an anode material resolves a major issue with commercial graphite, eliminating the problem of Li-plating. TMOs have the potential to deliver a promising Li-ion storage potential of approximately 700 mAh/g, as indicated by the chemical equation $MO + 2Li^{+} + 2e = M + Li_2O$ (Cheng et al. 2021).

Out of all the transition metal oxides (TMOs), nickel oxide stands out for its affordability, environmentally friendly attributes, abundant availability, and significantly higher nominal Li-ion storage potential (718 mA h g^{-1}, nearly two-fold that of graphite) (Rai et al. 2013). NiO has a density of 6.81 g cm^{-3}, which is three times greater than graphite's density of 2.26 g cm^{-3}. In theoretical terms, NiO anode has a higher energy density than graphite anode by 5.8 times (Li et al. 2011).

However, the utilisation of NiO in practical applications for lithium-ion batteries (LIB) has endured substantial hurdles. These challenges encompass significant volume alterations, structural failure of the NiO electrode, and a significant shortfall in ionic conductivity. Consequently, this compromises the electrochemical performance, including service life and power capability.

As shown in the equation below, NiO anode undergoes the following conversion reaction with Li-ions:

$$NiO + 2Li^{+} + 2e^{-} \leftrightarrow Ni + Li_2O$$ Equation 2.17

Lithium oxide (Li_2O) can become complex and electrochemically inactive when its size increases significantly, resulting in a decrease in anode conductivity and capacity degradation (Liang et al. 2013).

Hence, numerous researchers have undertaken investigations to address these challenges by exploring different structures of NiO and incorporating various strategies to enhance its performance (Tao et al. 2012; Zhang et al. 2016; Chen et al. 2018). An effective approach frequently employed in the literature involves the combination of NiO with graphene.

Besides increasing the available surface area, the assembly design also enhances electrical conductivity and provides mechanical flexibility essential to mitigating NiO's volume alteration.

Chen and their colleagues created ultrafine NiO nanocrystals, which were then integrated into a 3D graphene network using an in situ hydrothermal process followed by forging (Chen et al. 2018). The distinctive morphological arrangement represented in **Figure 2.16** allows the hybrid assembly to exhibit an exceptionally superior reversible Li-ion storage capability of 1104 mAh g^{-1} completing 250 cycles at a 0.2 C rate. Furthermore, it demonstrates excellent power competence, retaining a Li-ion storage capability of 440 mAh g^{-1} at a 3 C rate, while also maintaining superior capacity retention throughout the charge/discharge reactions.

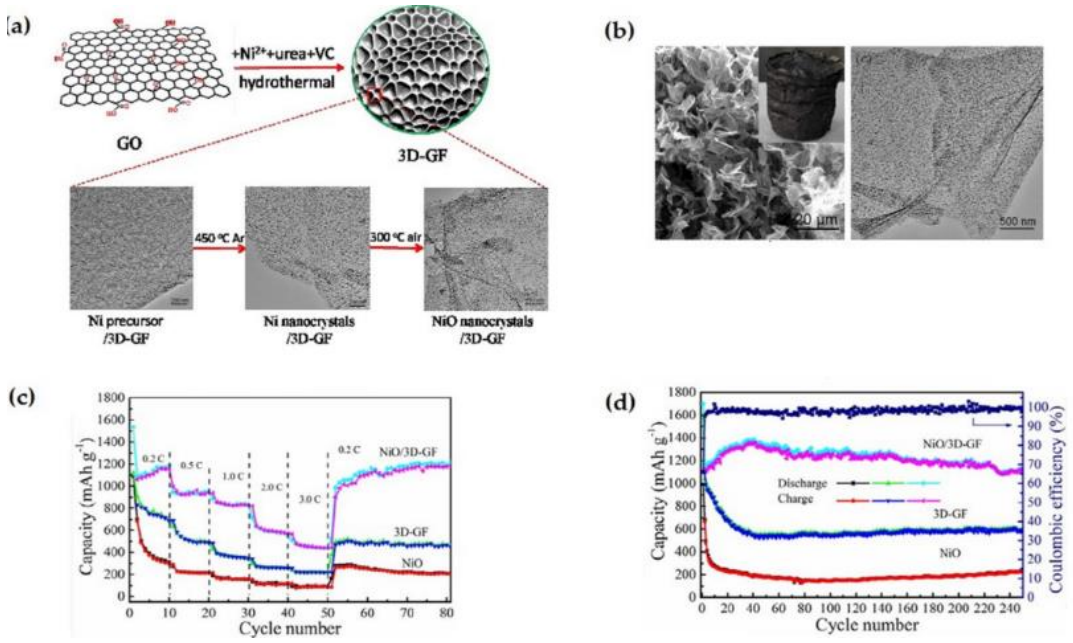

Figure 2.16 (a) A graphic illustration of the NiO/3DGF construction procedure. (b) SEM and TEM images of the nanohybrids (c) The rate capability of the nanocomposite with three different electrodes at different current rates. (d) A comparison of cycling performance and coulombic efficiency of the nanocomposite.

Adapted from (Chen et al. 2018).

Tao and his research team observed that when they utilised a 3D-hierarchical composite containing NiO and graphene nanosheets (GNS) as the anode as shown in **Figure 2.17**, it resulted in a substantial enhancement in lithium storage capacity, achieving an impressive specific discharge Li-ion storage of 1400 mAh g^{-1} (Tao et al. 2012).Furthermore, the NiO–GNS assembly manages to maintain an approximate specific Li-ion storage potential of 1065 mAh g^{-1} even completing 50 cycles at a current flow of 200 mA g^{-1}. The significant characteristics improvement can be assigned to the effective management of NiO volume changes and the enhanced electrical conduction of the NiO–GNS assembly throughout the cycling process.

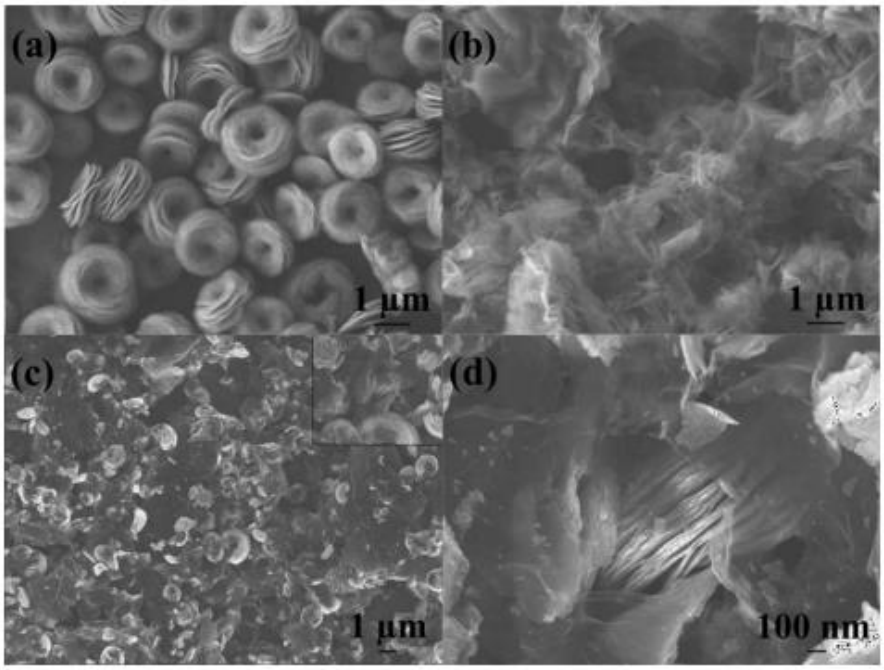

Figure 2.17 The SEM images of NiO carnations (a) GNS (b) 3D-hierarchical NiO–GNS composites (c) and (d). The inset in (c) reveals individual NiO carnations surrounded by GNS.

Adapted from (Tao et al. 2012).

Zhang and their team formulated NiO-graphene-carbon nanotubes (NiO-G-CNTs) through a hydrothermal technique, as illustrated in **Figure 2.18** (Zhang et al. 2016). These nanohybrids demonstrated a first Li-ion discharge capability of 1515.1 mAh g^{-1}. They also exhibited a durable and reversible Li-ion storage capability of 1022 mAh g^{-1} at a current flow of 100 mA g^{-1}, and a specific capacity of 858.1 mAh g^{-1} following 50 cycles at the same specific current flow. When subjected to a higher specific current flow of 1000 mA g^{-1} and after 40 cycles, the nanohybrid maintained a storage capability of 676 mAh g^{-1}. This enhancement can be credited to the gradual activation of graphene sheets within the nanohybrids during the cycling process.

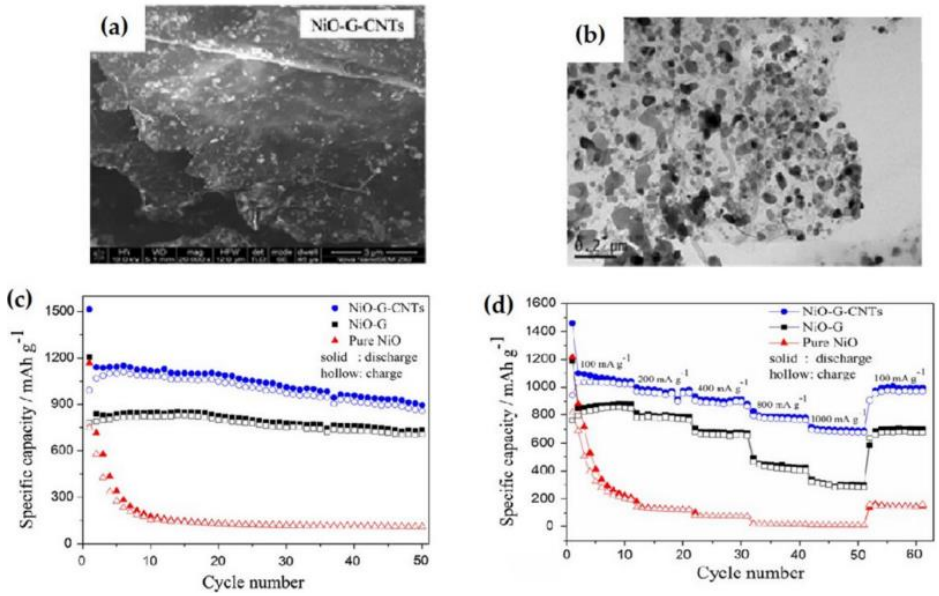

Figure 2.18 (a, b) SEM and TEM micrographs of 3D NiO–G–CNTs (c) Cycling performance comparisons of NiO–G–CNTs, NiO–G, and pure NiO electrodes at a specific current flow of 100 mA g^{-1} (d) Power delivery assessments of the NiO–G–CNTs, NiO–G, and NiO electrodes at different current densities.

Adapted from (Zhang et al. 2016)

Fu et al. recently achieved the successful fabrication of a 3D porous NiO flower/graphene flexible anode as illustrated in **Figure 2.19** (Fu et al. 2020). This electrode demonstrated a remarkable reversible storage capability of 359 mAh g^{-1}, even following approximately 600 cycles at a notably great specific current flow of 1 A g^{-1}. The flower-like structures were observed to hold a substantial quantity of nano-macro pores and voids, contributing substantially to the growth of the specific surface area, and effectively preventing the re-stacking of graphene sheets.

Nano-macro pores and voids were identified in the flower-like structures, increasing their specific surface area, and preventing re-stacking.

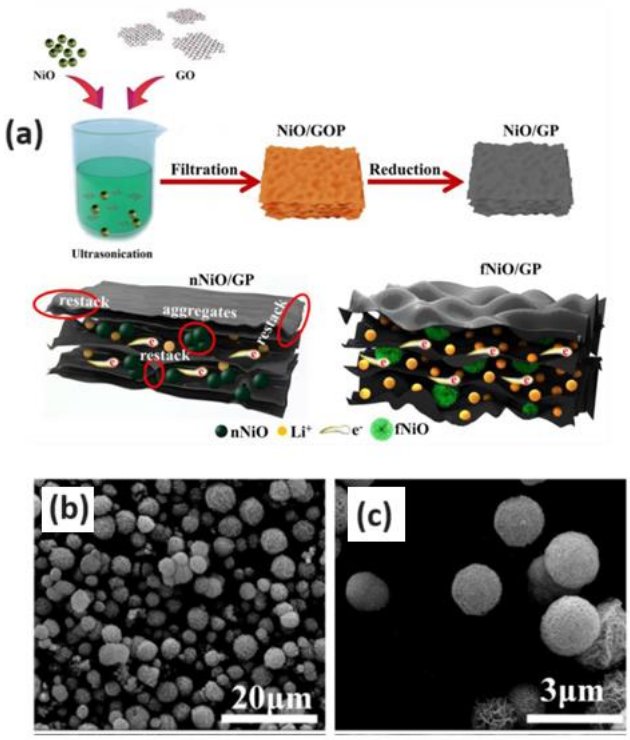

Figure 2.19 (a) A graphical representation of the typical process for fabricating NiO/GP and the subsequent paper structures, which incorporate nanoparticles (nNiO) and micro-flowers (fNiO). (b and c) SEM illustrations of NiO micro-flowers.

Adapted from (Fu et al. 2020).

Zhu and coauthors developed a reduced graphene oxide/NiO (RGO/NiO) assembly through a homogeneous co-precipitation process, pursued by successive annealing see **Figure 2.20** (Zhu et al. 2012). This composite demonstrated impressive initial specific discharge and charge energies of 1641 mAh g^{-1} and 1097 mAh g^{-1}, respectively. Notably, the RGO/NiO assembly displayed outstanding lifespan performance, maintaining an extraordinary specific discharge energy of 1041 mAh g^{-1} following 50 cycles

at a current flow of 100 mA g^{-1}, and exhibited excellent rate capability, achieving 727 mAh g^{-1} at a high current flow of 1600 mA g^{-1}.

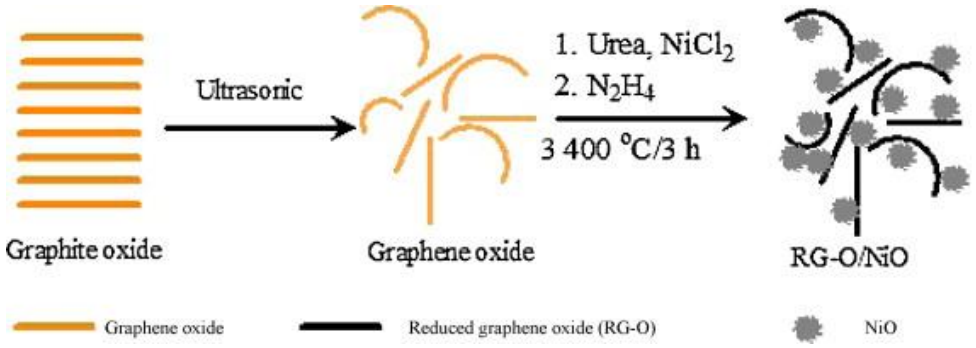

Figure 2.20 A schematic representation of the process for creating an RG-O/NiO composite.

Adapted from (Zhu et al. 2012).

To create a nano assembly of cross-linked rGO/NiO nanosheets, a simple hydrothermal reaction supported by heat treatment was utilised, as outlined in (Ren et al. 2019). This nanocomposite, when employed as a lithium-ion battery (LIB) anode, demonstrated exceptional characteristics, including high discharge capacity, service life, and impressive rate competence. Three variations of the rGO/NiO were created by adjusting the $NiCl_2$·6H2O content. Among these variants, the rGO/NiO-3 nanocomposite exhibited specific discharge and charge energy capabilities of 1570 and 1193 mAh g^{-1}, respectively, with a coulombic efficiency of 75.6% (as depicted in **Figure 2.21**). This coulombic efficiency was consistently conserved above 99.4% during the third cycle. The nanocomposite also demonstrated notable power competence, with a specific energy storage of 756 mAh g^{-1} at a current flow of 1.6 A g^{-1}. Moreover, it displayed exceptional service life, maintaining a specific energy storage of 1141 mAh g^{-1} even following 130 lifecycles,

representing 96.9% of the initial value. The nanocomposite further exhibited stable capacity retention, with a consistent value of 1023 mAh g^{-1} sustained throughout 200 cycles, highlighting its remarkable long-term cycle stability.

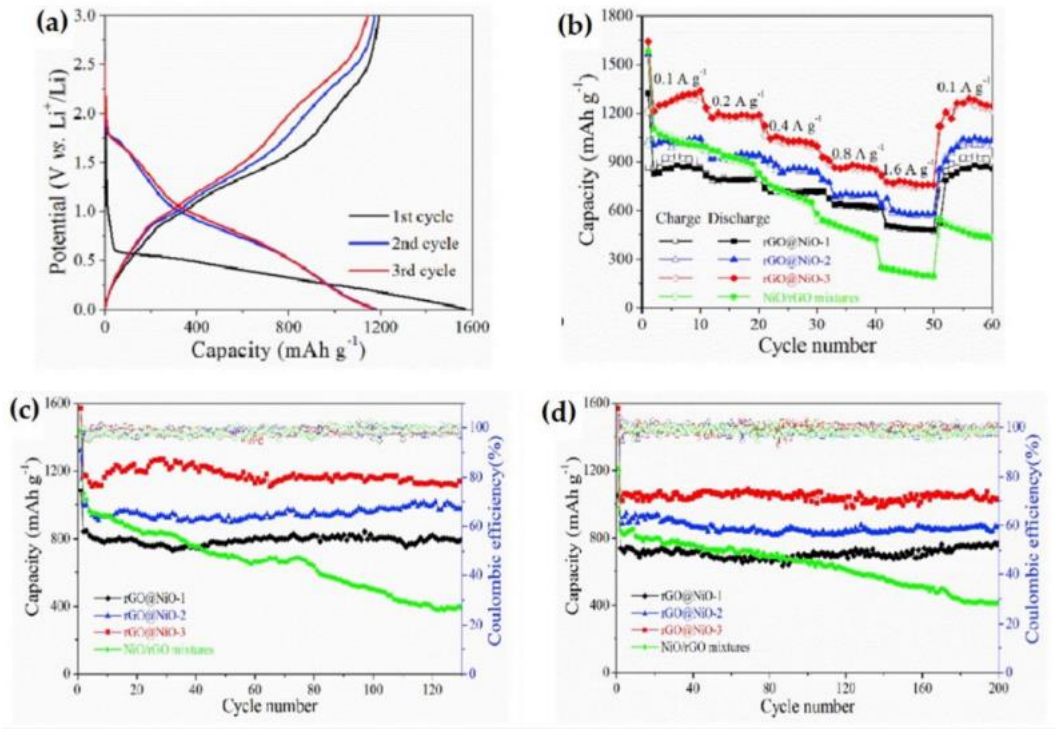

Figure 2.21 (a) Galvanostatic profile of rGO/NiO-3 nanocomposite. (b) Rate performance. (c,d) Cyclic performance at 100 and 400 mA g^{-1}.

Adapted from (Ren et al. 2019).

Wu and colleagues have successfully constructed a composite of NiO on holy graphene for lithium-ion battery (LIB) anode. This composite exhibited remarkable stability, maintaining a Li-ion storage potential of 659 mAh g^{-1} over 140 operational cycles at a high current flow of 500 mAh g^{-1}. Furthermore, the power assessment of this assembly was demonstrated with an energy of 940 mAh g^{-1} at 100 mA g^{-1} and 595 mAh g^{-1} at 1 Ag^{-1} (Wu et al. 2020). The distinctive arrangement of hollow NiO structures on the holy graphene

substrate effectively mitigates volumetric strains during charge and discharge processes, working in synergy to prolong the enhanced capacity **(Figure 2.22**)

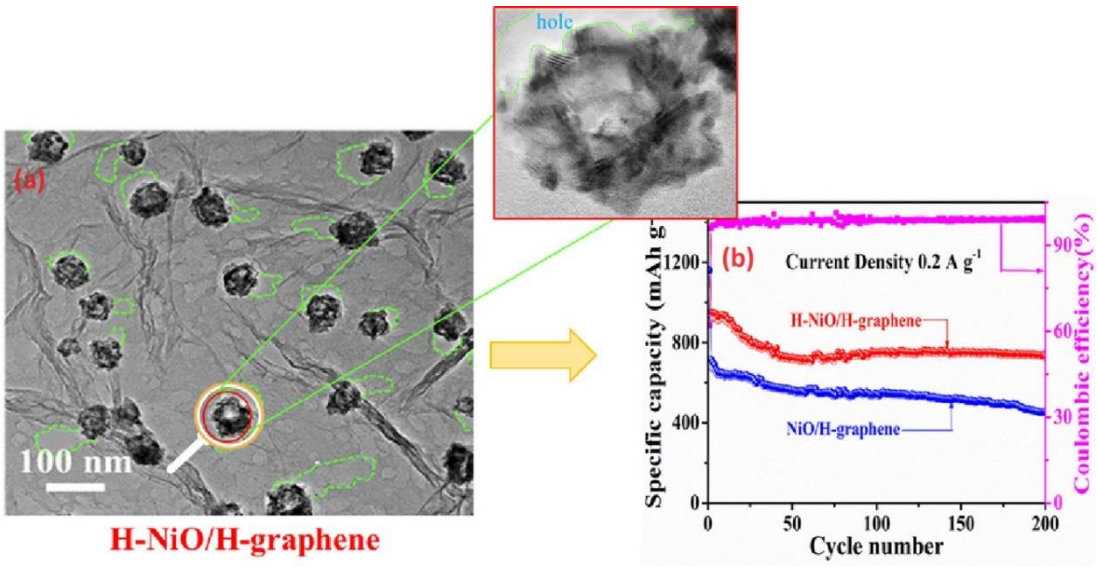

Figure 2.22 (a) TEM images of H-NiO/H-graphene (the green cycles indicate the etched holes on the graphene surface) (b) cycle life performance of the composite.

Adapted from (Wu et al. 2020).

Despite numerous efforts in the development of NiO/graphene composites, countless hurdles persist on the path to commercialisation. Due to intrinsic challenges, such as pulverisation, low electrical conduction, and compatibility issues with organic binders, particle aggregation during electrochemical reactions can result in irreversible capacity losses.

As discussed before, the conventional approaches used to tackle these challenges, including methods like 3D nanostructuring, doping, composite creation, and the integration of carbon-based materials and conductive

polymers, frequently fall short of providing a thorough understanding of the underlying causes of capacity degradation.

To bridge this knowledge gap, novel approaches must be considered, for advancing the development of NiO/graphene composites and overcoming the persisting obstacles to their commercial viability.

2.5 Graphene/Si composite anode for Li-ion batteries

Silicon (Si) exhibits an exceptional nominal gravimetric Li-ion storage potential of ~ 4200 mAh g^{-1}, based on its $Li_{22}Si_5$ stoichiometry, allowing it to store up to 4.4 lithium atoms. This remarkable capacity is ten times higher than that of carbonaceous materials. Furthermore, its widespread availability and lower cut-off working potential (0.3 V vs. Li/Li^+) underscores its substantial potential in various battery industry applications (Wu et al. 2019).

However, silicon (Si) demonstrates limited electrical conductivity, which elevates the overall impedance of the cell. Furthermore, during formation cycles, Si experiences significant capacity fading of around 2650 mAh g^{-1}(Wu et al. 2019). In contrast to carbonaceous anodes, Si is susceptible to substantial capacity loss due to its extensive volume alteration of nearly 400% throughout the continuous lithium-ion insertion and extraction processes (An et al.). Si serves as an alloy-type anode in LIBs and undergoes alloying and dealloying reactions with lithium ions, resulting in a considerable volume

expansion in Si particles. This expansion places mechanical stress on the Si particles, leading to cracking and detachment from the current collector.

Moreover, when Si particles rupture, they expose fresh Si surfaces, exacerbating the situation by promoting the growth of an excessive solid electrolyte interface (SEI). An excessive SEI thin sheet can hinder the efficiency of lithium-ion diffusion, increase internal cell resistance, electrode fracture and diminish overall battery performance (**Figure 2.23**).

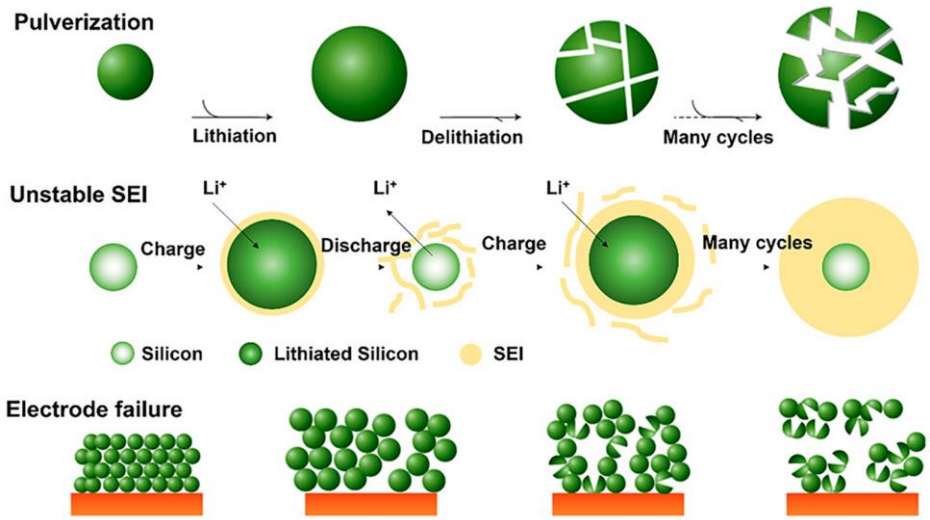

Figure 2.23 The diagram illustrates silicon anode failure modes during repeated lithiation/delithiation cycles: particle pulverization, SEI formation, and electrode fracture.

Adapted from (Sun et al. 2016c).

The over-expansion of the electrode, ongoing electrolyte deterioration, gas generation, and SEI formation can pose significant safety concerns. Excessive cell package inflation can lead to mechanical stress and pressure accumulation within the battery, potentially causing battery cell rupture or

deformation, which may result in leaks, thermal runaways, or even explosions (Sun et al. 2022).These safety concerns underscore the critical importance of addressing the challenges related to volume expansion and swelling in Si anodes within LIBs to ensure the overall stability and reliability of the battery system.

To mitigate the consequences of Si, many techniques have been reported since the 1990s such as utilising various Si nanostructures (Gu et al. 2015) different varieties of binders (Li et al. 2021b), dispersion of Si within inactive or active matrices (Wu et al. 2019) and Si thin films (Salah et al. 2019). Liu and Co-authors discovered that the use of nano Si could effectively reduce the particle fracturing in Si, with the research findings demonstrating that the particles smaller than 150 nm for crystalline Si and less than 870 nm for amorphous Si exhibit keen resistance to fracturing during the initial lithiation cycle (Liu et al. 2012). Furthermore, the investigation also researched the exploration of nano-sized Si in various structures including porous/hollow structures, nano-sheets, nano-spheres, nanotubes, and nanowires, resulting in the demonstration of enhanced capacity and cycle life performances (Ashuri et al. 2016). Nano Si materials are well known to have added lithiation/delithiation active sites compared to the bulk Si, attributed to their exceptional surface-to-volume ratio, which consequently enhances their capacity and electron transfer kinetics. In addition, it is also anticipated to yield high-rate performance and limited volume change, due to low charge transfer resistance and reduced electrode stress (Ashuri et al. 2016).

In general, Si nanowires exhibit notable stability against particle cracking due to their mechanical flexibility and resistance to strain. However, they are often

prone to detachment from the current collector, primarily because of stress accumulation at their roots during volume changes caused by lithium insertion. A recent study by Hung et al. introduced an interconnected system of Si nanowires to mitigate individual detachment and regulate capacity degradation (**Figure 2.24**). Their findings revealed sustained charge retention even after 40 cycles, operating within a voltage range of 1.50 to 0 V vs. Li/Li^+ at a C/2 rate, alongside an impressive power capability of 8C (Nguyen et al. 2011).

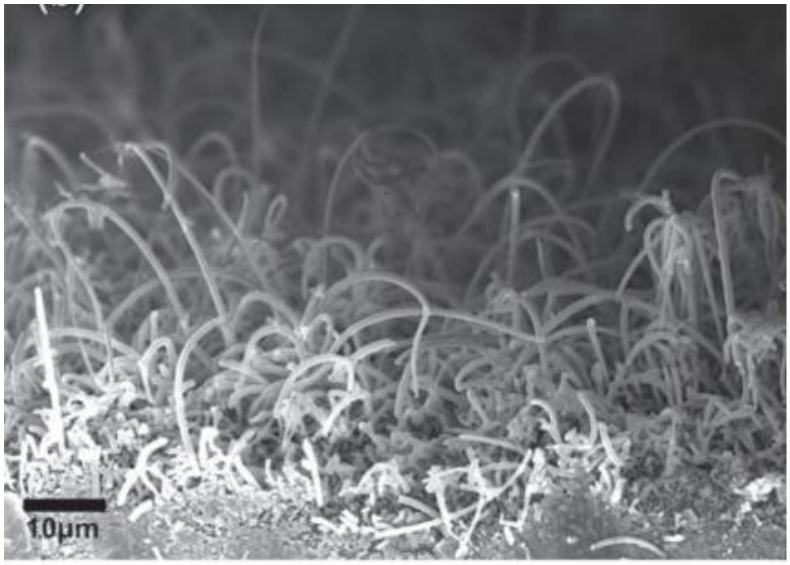

Figure 2.24 SEM cross-sectional view of interconnected Si nanowires. Adapted from (Nguyen et al. 2011).

An interesting recent publication by Yao et al. introduces a Si hollow nanospheres architecture with an initial Li-ion discharge energy of 2725 mAh g^{-1} and demonstrates excellent energy storage retaining over 700 cycles (Yao et al. 2011). The exceptional cyclability demonstrated by these Si hollow nanospheres represents one of the longest reported lifespans observed for bare Si anodes.

Nevertheless, the utilisation of pristine silicon (Si) in industrial LIBs faced significant challenges primarily because of the extensive requirement for

binder and conductive materials, as well as its low initial Coulombic efficiency (CE) and enormous volume change over lithiation and delithiation. A crucial factor to note is that while silicon exhibits a higher theoretical capacity in comparison to graphite, achieving substantial volumetric and areal capacities for industrial equipment proved to be difficult due to its poor mass loading capability (Wu et al. 2019).

To encounter the limitations of Si, the latest research attraction redirected to the co-utilisation of Si and carbon-based nanomaterials for a practical LIB anode (Wu et al. 2019). The composite demonstrates encouraging Li-ion battery performances as a result of the synergistic properties of the two nanomaterials. In this approach, silicon (Si) contributes a high capacity, while the carbonaceous material ensures excellent conductivity and mechanical elasticity to accommodate the Si volume change.

Most importantly, carbonaceous materials show a critical responsibility in preventing the Si and electrolyte direct contact, leading to a stable solid electrolyte interface (SEI) formation. The enhanced areal and volumetric capacities and longer cycle life are observed as added benefits. For example, recently reported ant-nest-like bulk porous silicon composite with carbon coating, demonstrated a promising specific Li-ion storage potential of 1271 mAh g^{-1} and an impressive areal Li-ion storage potential of 5.1 mAh cm^{-2}. This composite showcased a remarkable cycle life of 90% capacity retention over 1,000 cycles (An et al. 2019).

The hunt for carbon/Si nanohybrids led to the exploration of various carbon-based materials for combining with Si to create promising LIB anodes. These carbon materials include zero-dimensional carbon structures (An et al. 2019)

such as carbon nanoparticles, one-dimensional nanowires, and nanotubes (Wang et al. 2013), two-dimensional substances including graphene oxide (GO), reduced graphene oxide (rGO) and graphene (Cen et al. 2018), and three-dimensional porous or hierarchical carbon structures (Liu et al. 2021).

Among these materials, graphene/Si nanohybrids have garnered significant attention for use in lithium-ion battery anodes (Cen et al. 2018; Sehrawat et al. 2021). This is attributed to their enhancements in initial Columbic efficiency, power competence, and lifespan performance. The exceptional electronic conductivity, excellent specific surface area, outstanding mechanical flexibility, and strength of graphene make it a valuable addition for improving electron transfer kinetics and Li-ion diffusion in silicon nanoparticles, consequently enhancing the battery performance of Si anodes.

Silicon and graphene can be blended to make a nanocomposite, and this approach has been a simple and efficient technique for producing a Gr/Si composite. The graphene matrix offers several advantages, including serving as a physical support for Si nanostructures, acting as a cushion to absorb the significant volume changes in silicon, and providing a conductive pathway for charge transport.

In a study by Lee and their co-authors, they successfully created a Si/graphene composite by dispersing silicon particles within graphene sheets (**Figure 2.25**) (Lee et al. 2010). The resulting nanocomposite exhibited an impressive original energy storage of 4200 mAh g^{-1} at 1 A/g completing 50 cycles, and it maintained a stable reversible storage potential of 1500 mAh g^{-1} even completing 200 cycles. These findings clearly illustrate that incorporating Si nanoparticles into the graphene network is an efficient approach for mitigating

the volume changes experienced by Si during cycling. This is primarily attributed to the outstanding mechanical and buffering support provided by graphene, in addition to its high conductivity. The authors emphasized several key factors that contributed to the remarkable electrochemical performance achieved in their study. These factors include the even distribution of Si nanoparticles within the graphene sheets, the benefit of thinner graphene sheets, the presence of high crystallinity, and improved electrical conductivity.

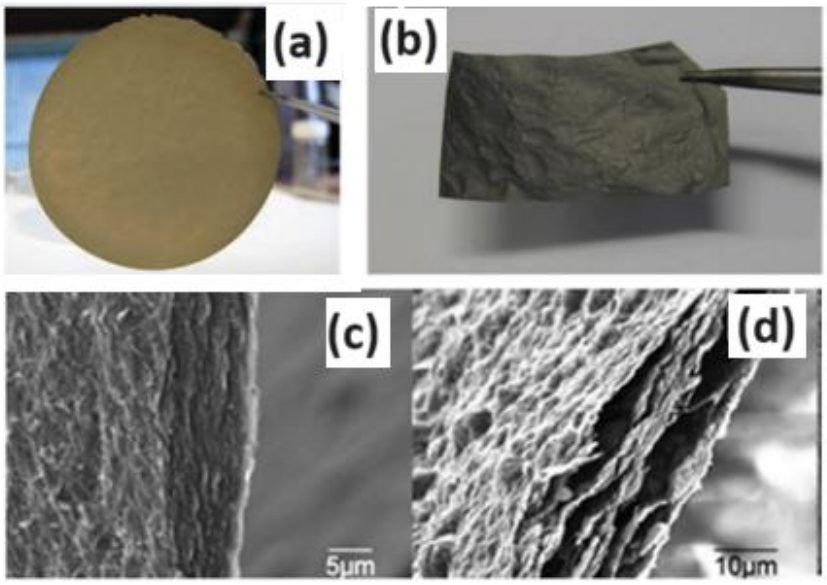

Figure 2.25 (a) Silicon-graphene oxide (SGO) (b) Silicon/graphene (SG) composite paper made by reducing SGO (c and d) Edge-view SEM micrographs of SGO and SG papers.

Adapted from (Lee et al. 2010).

As an alternative approach, Wang and colleagues introduced a simple filtration method, followed by hydrazine reduction, resulting in the fabrication of a flexible, free-standing Si/Gr nanofilm (**Figure 2.26**) (Wang et al. 2010). This composite was produced by hydrazine reduction of GO and commercially

available Si NPs, with the GO being synthesized through the modified Hummer's oxidation of natural graphite. The subsequent graphene/Si paper exhibited a charge storage capability of 708 mA h g^{-1} over 100 cycles (**Figure 2.26**). However, concerning the battery energy storage and operational lifespan, no noticeable improvement was observed when compared to the earlier findings of Lee and co-workers (Lee et al. 2010). A significant, irreversible energy shortfall throughout the initial cycle has been identified as a significant limitation. Nevertheless, these two findings collectively emphasize the advantages of incorporating both Si and graphene for achieving stable capacity.

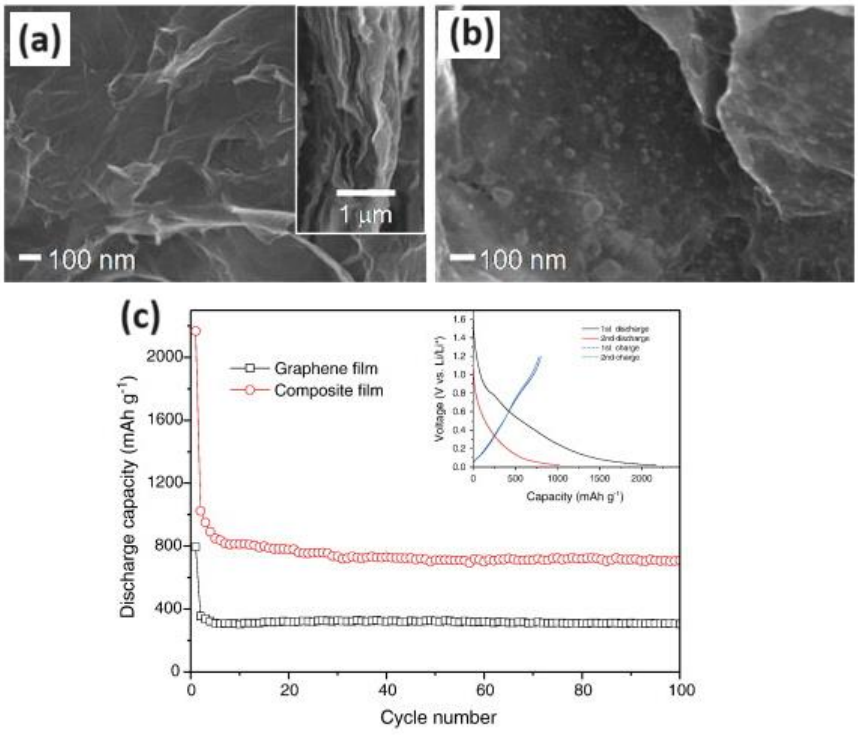

Figure 2.26 SEM micrograph of (a) free-standing graphene film with a cross-sectional view (inset), (b) free-standing graphene-Si nanofilm (c) cyclic performance.

Adapted from (Wang et al. 2010).

Sun et al. (Sun et al. 2014) introduced an innovative approach involving in-situ plasma-assisted mechanical milling to enhance the distribution of Si nanoparticles within graphene layers (**Figure 2.27a**). The resulting Si NP/graphene nanocomposite (milled for 20 hours) demonstrated an impressive specific Li-ion storage potential of 715 mAh g^{-1} at a current flow of 0.5 A g^{-1} completing 50 cycles (**Figure 2.27b)**. However, when this electrode was incorporated into a full-cell design alongside a commercial $LiMn_2O_4$ cathode, the capacity dropped significantly to 150 mAh g^{-1}, which was more than six times lower than the value observed in the half-cell configuration.

The lower capacity of full cells can mainly be attributed to the limited lithium inventory and other factors such as the N/P ratio, electrode thickness, calendaring density, and active material loadings (Smith et al. 2023).

In a subsequent study by the same research group in 2016 (Sun et al. 2016a), it was discovered that the use of commercial expanded graphite (EG) instead of flake graphite, combined with plasma-assisted milling (p-milling) of Si NPs, could enhance cyclability. Expanded graphite, owing to its loose and porous structure, facilitated efficient exfoliation, ensuring the effective encapsulation of Si NPs and thereby extending the cycle life. The assembly demonstrated an improved reversible energy of 942 mAh g^{-1} at 0.2 A g^{-1} over 100 cycles, with an impressive 88% capacity preservation. Furthermore, a superior charge Li-

ion storage of 1000 mAh g^{-1} at 0.2 A g^{-1} was achieved by completing 150 cycles. This enhanced performance once again emphasized the critical role of well-coated Si in achieving an extended cycle life.

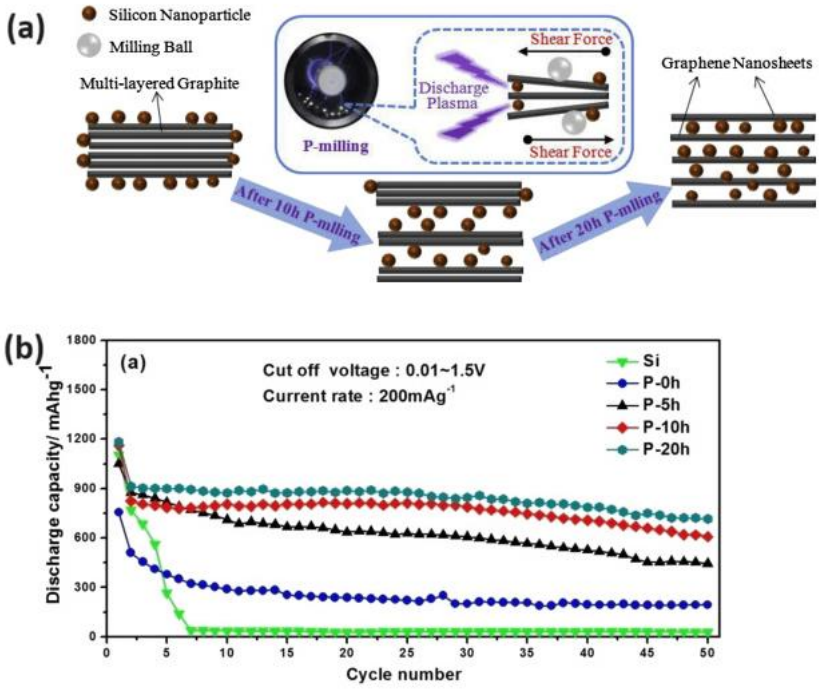

Figure 2.27 (a) A schematic representation of the preparation of nano-Si/GNs composites using plasma-assisted milling (b) Cycling performance for nano-Si/GNs milled for different time durations.

Adapted from (Sun et al. 2014).

In a recent study, Liu and their fellow researchers introduced a hydrothermal-assisted reduction of GO/Si nanocomposite using sodium borohydride, presenting an advanced and optimised method for producing rGO/Si anodes (**Figure 2.28**) (Liu et al. 2019). Specifically, the denoted 10rGO/Si-600 composite, with a quality ratio of 10 and calcination at 600°C, exhibited remarkable performance. It displayed an impressive initial Coulombic efficiency (CE) of 93.2% (**Figure 2.28c**) and a reversible Li-ion storage

capability of 2317 mAh g^{-1}. Furthermore, the cycling retention remained high at 85%, with an energy of 728 mAh g^{-1} sustained over 100 operational cycles, all achieved at a current flow of 0.1 A g^{-1}.

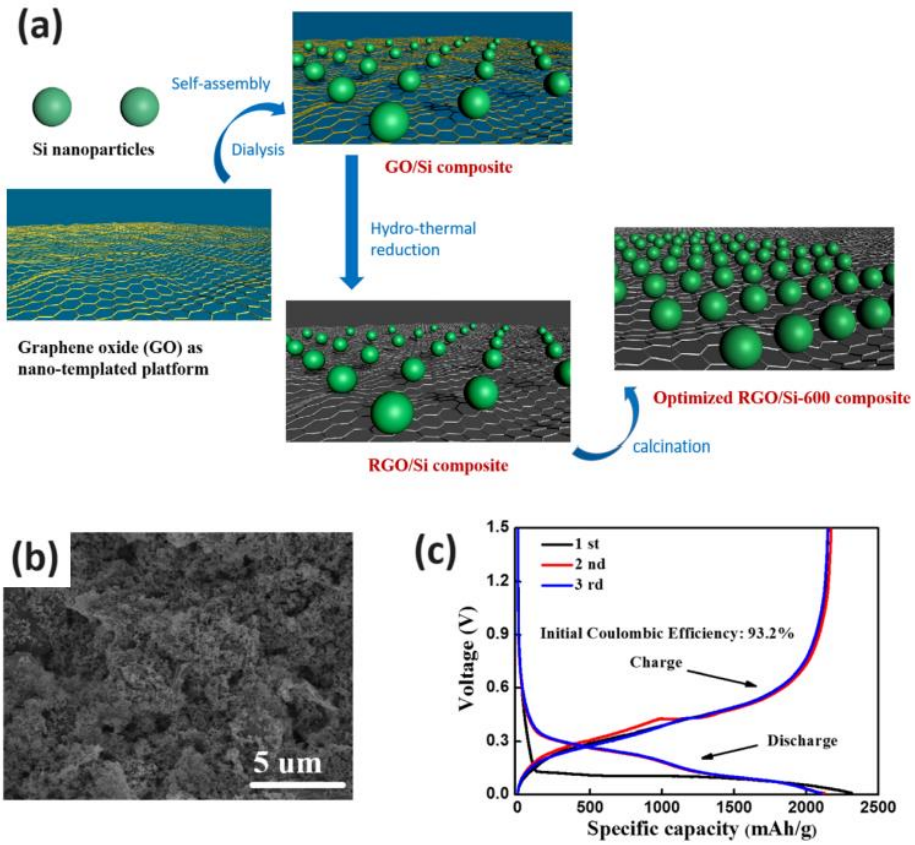

Figure 2.28 (a) A schematic representation of the synthetic approach for the RGO/Si composite (b) SEM image of 10RGO/Si-600 (c) First charge−discharge cycles for the 10RGO/Si-600 at 0.1 A g^{-1}. Adapted from (Liu et al. 2019).

Noncovalent bonding has gained recognition as a viable strategy for anchoring Si nanoparticles onto the surface of graphene, proving to be an effective strategy for preventing Si aggregation and graphene stacking. This approach offers several advantages, including high tunability, excellent processability, and fewer side reactions (Ye et al. 2010). Ye and colleagues (Ye et al. 2014b)

developed an innovative self-assembly technique to anchor surface-modified, negatively charged Si NPs (zeta potential of -43 mV) onto positively charged graphene sheets (zeta potential of +29 mV) through non-covalent electrostatic attraction. They aimed to regulate Si aggregation through electrostatic charge repulsions and thus mitigate electrode stress by enabling the free expansion and contraction of Si NPs, thanks to a porous Si coating design. The synthesis procedure involved three key steps: (1) the synthesis of charged nanomaterials, Si (Si-COOH) and graphene (protic ionic liquid); (2) the dispersion of charged materials in various weight ratios (Si/Gr = 1/1, 1/2, 2/1, and 3/1) to form a nanocomposite; and (3) thermal processing of the composite at 500 °C to create a nanoporous coating on Si particles (**Figure 2.29**). The observed performance was impressive as 803 mAh g^{-1} over 100 operational cycles at 200 mA g^{-1}, with less than a 0.25 % capacity loss per cycle up to 150 lifespan for the Si/Gr composite with a 3:1 weight ratio.

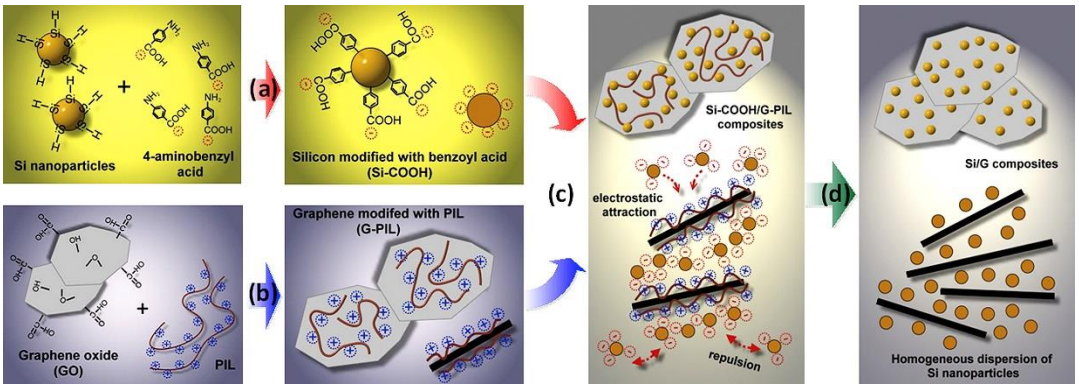

Figure 2.29 Assembly of Si/G composites: (a and b) negatively and positively charged Si nanoparticles and graphene nanosheets (c) Self-assembly of Si-COOH and G-PIL through electrostatic attraction, (d) Thermal processes create voids between the silicon and graphene.

Adapted from (Ye et al. 2014b).

Various fabrication strategies have been proposed to consistently encapsulate silicon nanostructures using graphene and reduced graphene oxide (rGO) sheets, including chemical vapour deposition (CVD), spray drying, spin coating, and freeze-drying, among others.

In a significant development in 2012, Luo and their co-authors successfully pioneered the encapsulation of silicon nanoparticles with graphene as an effective strategy to enhance cycle life (Luo et al. 2012). They achieved this by preparing crumpled graphene shell-coated silicon nanoparticles through a one-step evaporation-induced capillary force technique. The highly crumpled graphene acted as a flexible shell to accommodate the volume expansion of silicon. (See **Figure 2.30**) This nanocomposite exhibited an impressive Li-ion storage potential of 940 mAh g^{-1} after 250 cycles at a specific current flow of 1 A/g, with an 86% capacity retention. The exceptional electrochemical efficiency of this nano assembly was credited to the efficient buffering of silicon volume expansion enabled by the porous carbon coating design. In contrast, the authors reported that incomplete and conformal carbon shells could lead to the rupture of silicon particles, resulting in the establishment of excessive solid-electrolyte interphase (SEI) on newly exposed areas, ultimately leading to poor electrochemical performance.

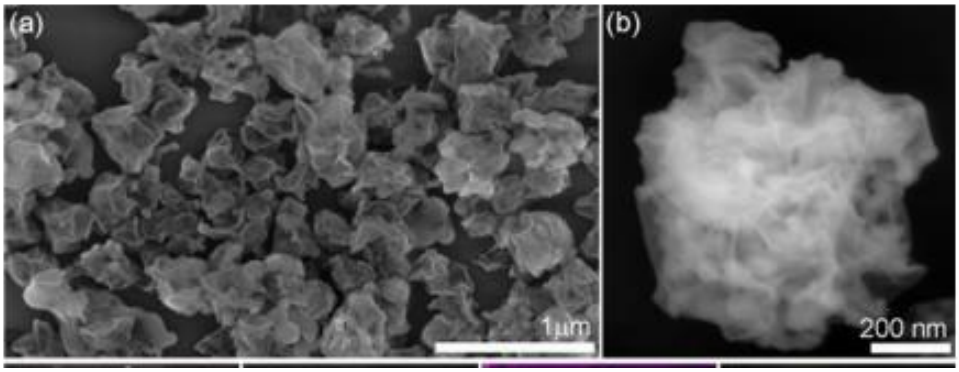

Figure 2.30 (a) Low-magnification SEM image that displays multiple crumpled capsules. These capsules consist of graphene-wrapped silicon (b) SEM image that zooms in on a single capsule, providing a closer look at its structure.

Adapted from (Luo et al. 2012).

In further advancement of graphene/silicon (Gr/Si) nanocomposites, a novel hierarchical composite was synthesized, incorporating silicon nanowires (NW) and reduced graphene oxide via a combined approach involving solvothermal and CVD techniques (Ren et al. 2014). The key feature of this study was the introduction of (111)- oriented silicon NWs as a more efficient crystallographic design for improved electrochemical kinetics. The (111)- oriented silicon NWs were directly grown on the rGO matrix using CVD, and the resulting composite displayed significantly enhanced electrochemical performance compared to bare silicon NWs or silicon particles (Si NWs) (**Figure 2.31**).

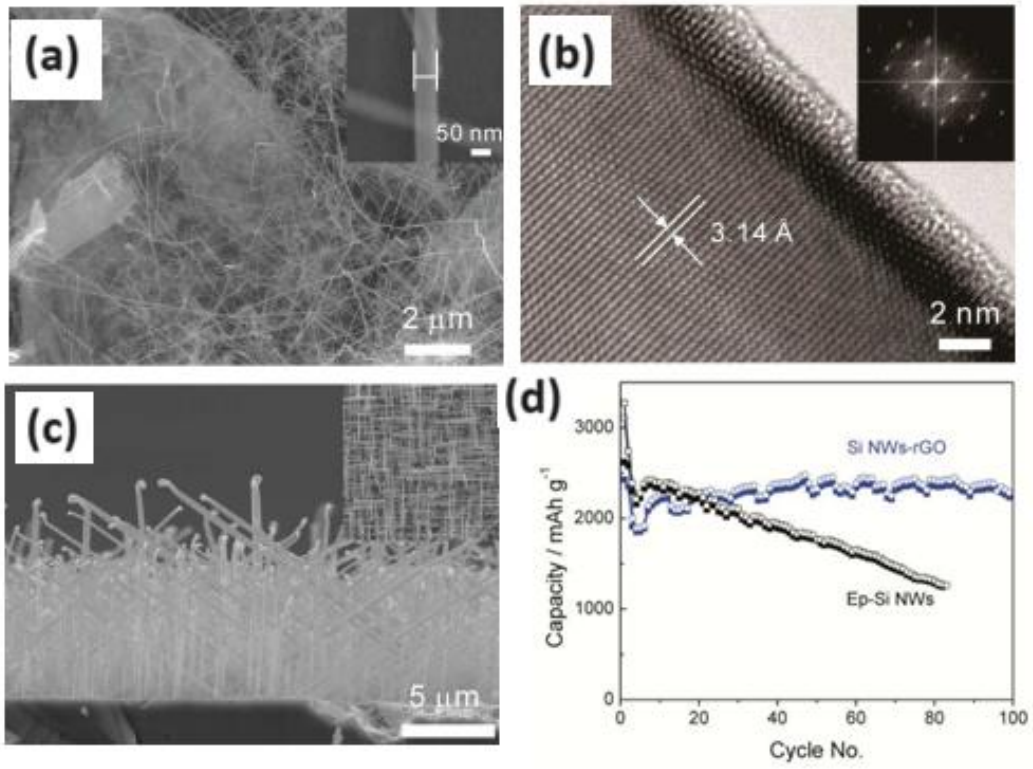

Figure 2.31 CVD synthesised Si NWs–rGO composite (a) SEM micrograph (inset shows the diameter of a single Si NW). (b) TEM picture of a single Si NW (inset shows the Fourier transform image). (c) SEM micrograph of Si NWs array on Si (100) wafer (inset is the top-view image) (d) Cycle life of the Si NWs–rGO and Si NWs.

Adapted from (Ren et al. 2014).

In a half-cell configuration, this composite achieved a superior lithium storage Li-ion storage potential of 2300 mAh g^{-1} at a power of C/3 over 100 cycles, along with impressive areal and volumetric energy storage capacities of 3.45 mAh cm^{-2} and 1725 mAh cm^{-3}, respectively. The outstanding electrochemical characteristics of the rGO/Si NW assembly may be attributed to several key properties:

- Efficient accommodation of the volume change in silicon by the flexible rGO matrix, ensuring the mechanical integrity of the electrode over cycling.
- The establishment of a 3-D porous network through the tight adhesion of rGO to the silicon NW surface promotes the storage of Li ions.
- Improved reaction kinetics facilitated by the short-distance lateral charge transport between the NW and rGO, along with fast Li-ion diffusion enabled by the (111) oriented silicon NW crystallography.

A research team led by Zhou (Zhou et al. 2012) employed a spin coating technique as a straightforward and efficient method to create graphene/silicon nanoparticles (Gr/Si NPs) film with void spaces surrounding the silicon nanoparticles (**Figure 2.32**). This binder-free anode demonstrated remarkable performance, boasting a high Li-ion storage capability of 1611 mAh g^{-1} at a specific current flow of 1 A g^{-1} after 200 cycles, with an impressive 74 % capacity retention. Furthermore, the electrode displayed excellent rate capability, delivering 648 mAh g^{-1} at a superior power of 10 A g^{-1} (**Figure 2.32**). The nanocomposite film featured a unique nanostructure that enhanced electronic conductivity and effectively controlled the volume change of silicon by incorporating void spaces around the silicon nanoparticles.

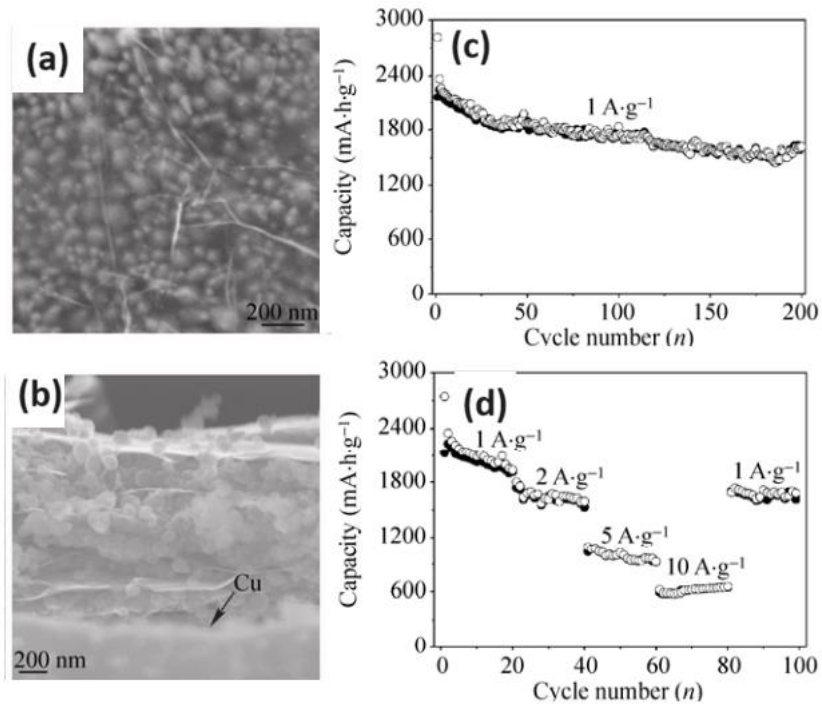

Figure 2.32 SEM micrographs of the SC-Si/G electrode (a) surface (b) cross-section. Electrochemical performance of SC-Si/G electrode (c) cycle life (d) rate capability.

Adapted from (Zhou et al. 2012).

In a recent development, Zhou and their team introduced a sandwiched anode system for LIBs with graphene and silicon nanoparticles (Si NPs). This innovative system was fabricated using a simple vacuum-assisted filtration approach (Zhou et al. 2018). As depicted in **Figure 2.33**, Si NPs were uniformly embedded within the conductive graphene matrix with the assistance of nano cellulose as a covalent cross-linking adhesive. The cross-linking and hydroxylation processes ensured the homogeneous dispersion of Si NPs within the graphene sheets, with the Si NPs serving as spacers to control the restacking of the graphene.

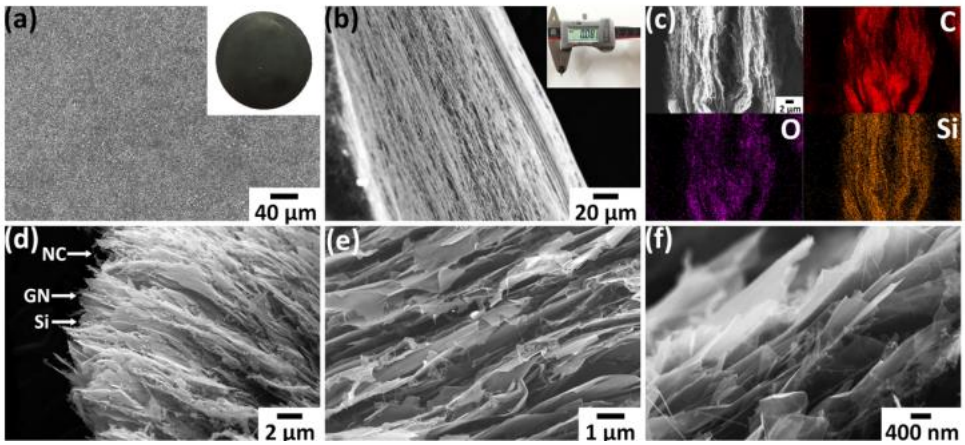

Figure 2.33 (a) The images include a scanning electron microscope (SEM) surface view and an overall photograph of a free-standing GN/NC/Si film (b) The image displays a cross-sectional SEM view of the free-standing GN/NC/Si film, with an inset indicating the thickness of the film (c) This set of images presents elemental mapping for carbon (C), oxygen (O), and silicon (Si) in the free-standing GN/NC/Si film. (d-f) These images show low- and high-magnification cross-sectional SEM views of the free-standing GN/NC/Si film, offering detailed insights into its structure and composition.

Adapted from (Zhou et al. 2018).

The composite was also observed to exhibit outstanding flexibility and mechanical properties, which effectively mitigated the volume changes experienced by silicon during the cycling process. The resulting sandwiched film exhibited outstanding performance, including a Li-ion storage capability of 1251 mAh g^{-1} at a specific current flow of 100 mA g^{-1} after 100 cycles and an excellent power capability of 405 mAh g^{-1} at 6.4 A g^{-1}.

In addition to literature findings, several companies are actively engaged in the large-scale production of graphene/silicon composites for lithium-ion battery anode materials. Among these, the Global Graphene Group (G3), headquartered in the USA, stands out. G3's graphene-enabled silicon anode

(GCA^{TM}) has earned praise for its remarkable storage capacity, ranging from 2000 to 2600 mAh/g, coupled with an impressive internal coulombic efficiency (ICE) exceeding 88%. Furthermore, it demonstrates compatibility with various passive materials and mixing procedures (Global Graphene Group 2024) (**Figure 2.34**).

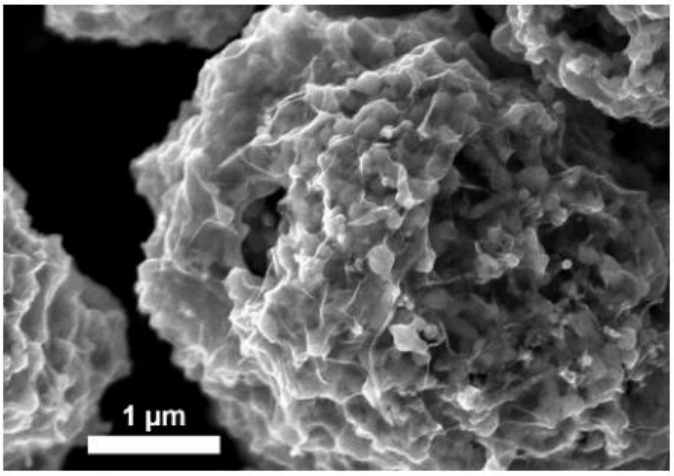

Figure 2.34 SEM image of G3's graphene-enabled silicon anode.

Adapted from (Global Graphene Group 2024).

Despite numerous literature efforts highlighting the enhanced electrochemical performance of silicon nanoparticles through graphene incorporation, aggregate formation remains a concern (Han et al.). Moreover, limited research has been dedicated to industrial-scale production, hindered by challenges including scalability, cost efficiency, and ensuring long-term electrochemical stability. Therefore, there is a critical need to investigate cost-effective, scalable, and environmentally friendly methods for preparing Si/graphene composites.

Chapter 3 Fundamental Experimental Approach

3.1 Hydrothermal synthesis

The materials synthesised in this thesis result from the hydrothermal synthesis method, which enables the controlled formation of nanostructures with specific shapes and crystal structures. Hydrothermal synthesis involves conducting chemical reactions in aqueous solutions at elevated temperatures and pressures, utilising salts like metal chlorides or nitrates as starting materials for inorganic compound synthesis. To enhance the solubility of these precursors, a mineraliser, such as NaOH, can be incorporated (Kafle 2020).

The synthesis process is explained by heating the solution within a sealed vessel, called autoclave as depicted in **Figure 3.1**. As the solvent's temperature approaches its boiling point, the pressure inside the vessel surpasses atmospheric levels. This interchange of temperature and pressure induces changes in the solvent's properties, affecting factors like density, viscosity, and dielectric constant. Notably, the dielectric constant of water decreases from 80 at 20°C to 55 at 100°C at high temperatures, approaching the values of non-polar solvents. Consequently, precursors of non-polar substances become more soluble, while polar and ionic substances tend to precipitate into solid phases (Kafle 2020).

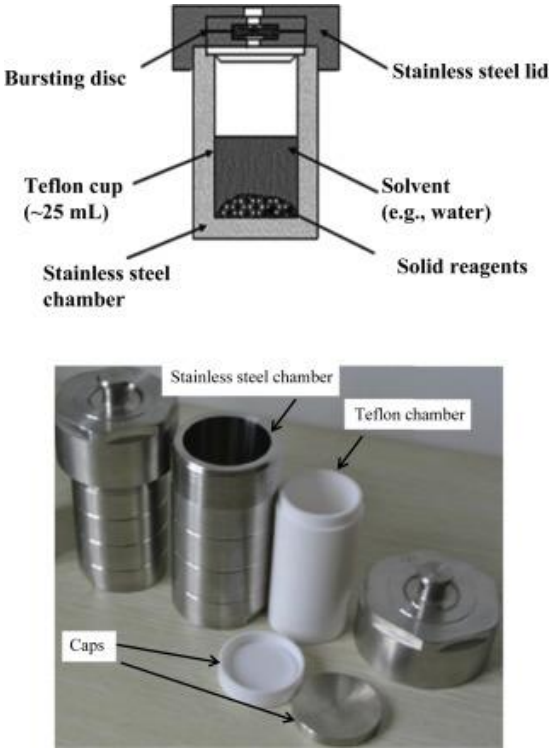

Figure 3.1 The upper image describes Teflon-lined stainless-steel autoclaves with inner components, showcasing the Teflon chamber encased within the stainless-steel chamber where reactions take place. The lower image showcases a commercially available Teflon-lined stainless-steel chamber. Adapted from (Kafle 2020).

In addition to rapid reaction times and high crystallinity, the hydrothermal method has abundant yields, uniform particle products, cost-effectiveness, environmental friendliness, and ease of scalability (Kafle 2020).

Nonetheless, hydrothermal synthesis does come with certain drawbacks. Predicting the outcomes of various reaction parameters can be challenging, often necessitating a trial and error approach. Additionally, safety concerns arise from the high pressures within the reaction vessels, and monitoring in-situ reactions proves challenging due to the closed system.

3.2 Research equipment

This chapter describes the equipment utilised in both material synthesis and the assembly of coin cells.

3.2.1 Box furnace

The box furnace, produced by Carbolite and illustrated in **Figure 3.2**, serves as an electric heating apparatus utilised for heat treatments. This heat treatment occurs in a normal atmospheric environment, leading to the oxidation of the samples. The furnace can reach the highest temperature of 1200 °C.

Figure 3.2 Box furnace.

3.2.2 Tube furnace

A tube furnace assembled by Carbolite (**Figure 3.3**) is employed to heat treat the anodes under argon conditions at different temperatures. The tube furnace can reach a highest temperature of 1200 °C.

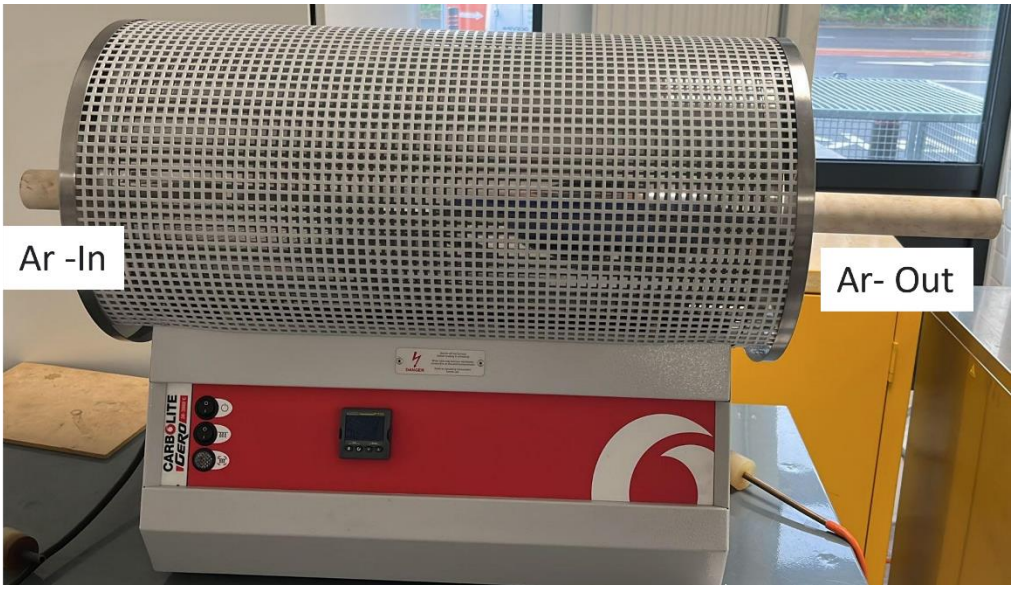

Figure 3.3 Tube furnace.

3.2.3 Vacuum oven

Figure 3.4 shows the vacuum oven OV-11, Jeio Tech Co**.** applied to dry anodes at 120°C under vacuum.

Figure 3.4 Vacuum oven.

3.2.4 Glove box

Figure 3.5 presents the sealed Argon-filled glove box manufactured by MBRAUN.

The glove box was used to construct the coin cells in an inert and controlled atmosphere. Glove boxes are defined by their built-in gloves, strategically positioned on their sides or fronts, which enable users to interact with objects or materials inside the enclosure without compromising the controlled environment. These gloves, constructed from butyl rubber or neoprene, create an effective barrier between the operator and the internal environment. Transparent panels crafted from airtight materials allow operators to observe the interior of the glove box while maintaining an impermeable seal that safeguards against the intrusion of moisture, oxygen, or other contaminants that could potentially disrupt the ongoing environment. To ensure an inert

atmosphere, inert gases such as argon or nitrogen are continuously circulated within the glove box.

Figure 3.5 Glove box (Lab star eco, MBRAUN).

3.3 Material characterisation techniques.

The synthesized materials were evaluated for morphology, crystallinity, and impurities using different techniques.

3.3.1 Scanning electron microscopy (SEM) fitted with energy-dispersive X-ray spectroscopy (SEM-EDS).

Figure 3.6 illustrates the scanning electron microscope (SEM, JEOL JSM-6010PLUS/LV) that was employed for the analysis of sample morphology. All samples underwent gold coating (approximately 7 nm) before analysis. This SEM is equipped with energy-dispersive X-ray spectroscopy (EDX) for detecting the elemental distribution within the sample. The SEM functions by scanning a rectangular area of a specimen using a focused electron beam, resulting in the generation of images. The interaction between electrons and

atoms in the sample is instrumental in determining the sample's surface topography and elemental analysis.

An electron beam strikes a specimen at an angle that generates secondary electrons that are emitted by excited atoms and can be detected in varying numbers depending on the angle of the beam's impact. A specialized detector collects the secondary electrons emitted from the sample and produces an image that portrays the surface topography.

Figure 3.6 Scanning electron microscope (SEM) fitted with energy-dispersive X-ray spectroscopy (SEM-EDS).

3.3.2 Raman spectroscopy analysis

Raman spectroscopy was used to investigate the chemical structure and graphite to graphene exfoliation, which was performed on a laser Raman

spectrometer (Raman, Horiba XploRATM) with a 532 nm laser (**Figure 3.7**). Raman spectroscopy provides valuable insights into the presence of functional groups in materials by detecting vibrations, rotations, and other low-frequency modes.

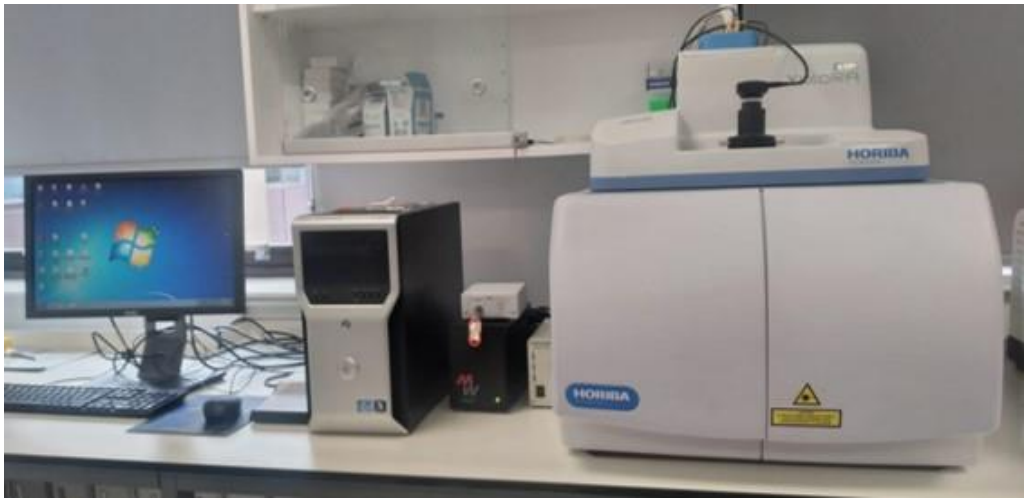

Figure 3.7 Raman spectrometer.

3.3.3 X-Ray diffraction

The crystallography details of the samples were assessed using a Siemens D5000 diffractometer powder XRD, which employed Cu Kα irradiation (λ = 1.54˚A) over a 2θ range of 20° to 80° at a scan rate of 0.02° (**Figure 3.8**).

Figure 3.8 X-ray diffractometer.

XRD primarily comprises three components: an X-ray tube, an X-ray detector and a sample holder. In this process, X-rays produced in the X-ray tube are directed at the sample, producing X-ray spectra containing distinctive data about the target material. These spectra can be refined using a filter, gathered by the X-ray detector, and ultimately transformed into a curve through software operation.

In addition to the previously mentioned techniques, the research incorporates the following essential methods and instruments:

- High-resolution transmission electron microscopy, accompanied by energy-dispersive X-ray spectroscopy (EDX), was employed to validate the expansion in the interlayer spacing of graphite and the synthesis of graphene. The observations were made using a JEOL JEM-2100F high-resolution transmission electron microscope operating at 200 kV.

- X-ray photoelectron spectroscopy (XPS) was employed to evaluate the chemical states of the synthesised compounds. A PHI Quantera X-ray photoelectron spectrometer was used for the XPS analysis, providing the chamber pressure at 5×10^{-9} Torr. An aluminium (Al) cathode served as the X-ray source. Core-level scans were executed with a pass energy set at 26.00 eV, and the source power was configured at 100 W.
- Thermogravimetric analysis (TGA) experiments were conducted utilising a TA Instrument-SDTQ600 in the presence of air (up to 1000 °C), employing a temperature ramp of 10°C per minute.

- The specific surface area and pore size distributions of the compounds were determined using the Brunauer−Emmett−Teller (BET) technique. Nitrogen sorption measurements were conducted at 77.4 K using an Autosorb iQ station 1 system. Before the analysis, all samples underwent a degassing process at 200 °C for 12 hours.

3.4 Electrode preparation

The slurries were crafted by blending the active material, Super P, and sodium carboxymethyl cellulose binder in de-ionized water, with the specific ratios detailed in Chapter 4 and Chapter 5. Using the doctor blade technique, the homogeneously mixed slurry was applied evenly and uniformly to a copper current collector (**Figure 3.9**). The coated electrode underwent an initial drying phase at 60°C for 5 minutes on a hot plate to minimise binder migration during the drying process. Subsequently, it was subjected to further drying at 120°C for 12 hours in a vacuum oven to eliminate any residual moisture. Following the drying stages, the electrode was punched into discs with a diameter of 13 mm (**Figure 3.9**).

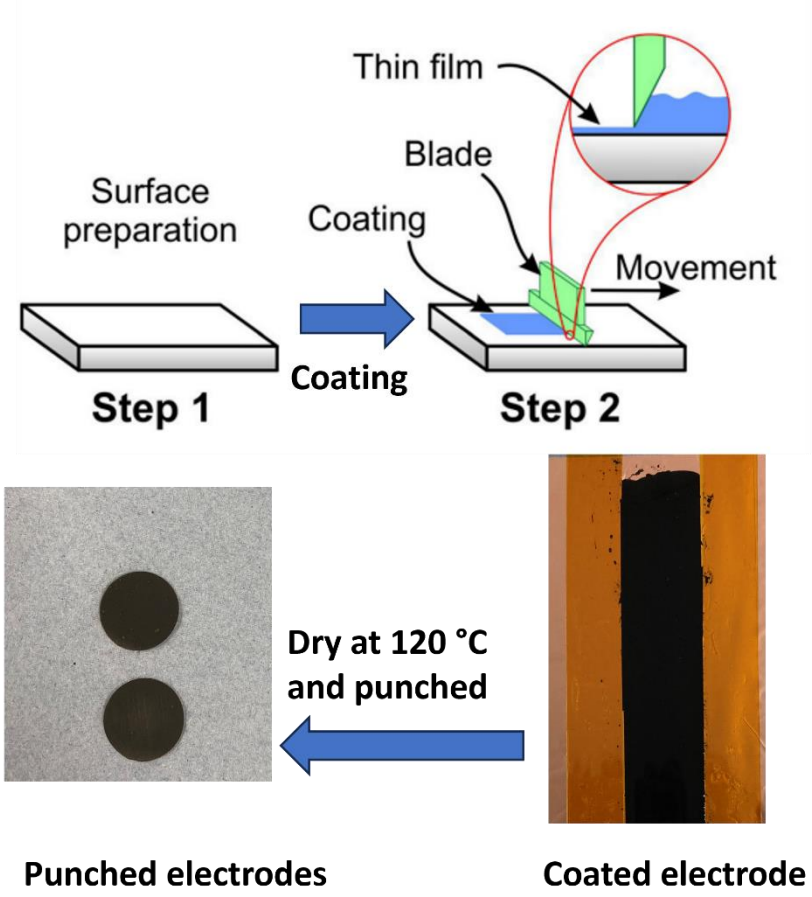

Figure 3.9 The doctor blade electrode preparation technique.

3.5 Coin cell assembly

The half-cells were compiled within a glove box and purged with argon to establish a controlled environment. The glove box maintains an atmosphere with moisture and oxygen concentrations steadily lower than 1 ppm. The counter electrode utilised was a lithium disk from MTI Corp., measuring 15.6 mm in diameter and 0.45 mm in thickness. For the separator, a glass microfiber filter disk (GF/B) was employed, with a diameter of 18 mm and a pore size of 1.0 µm.

In Chapter 4, a 60 µl electrolyte was employed, which comprised a 1M solution of Lithium hexafluorophosphate (LiPF6) dispersed in a blend of ethylene

carbonate and diethyl carbonate in a 1:1 volume ratio, additionally comprising 2% vinylene carbonate and 3% fluoroethylene carbonate additives, all of battery grade quality, from Solvionic. In Chapter 5, a 60 µl electrolyte was used, consisting of a 1M solution of lithium hexafluorophosphate (LiPF6) salt dispersed in a solvent blend of ethylene carbonate and ethyl methyl carbonate in a 1:1 volume ratio (MTI Corp.).

A coin cell is constructed by assembling the positive can, working electrode, separator, Li metal, spacer (1 mm thickness), spring, and ultimately the negative cover as shown in **Figure 3.10**.

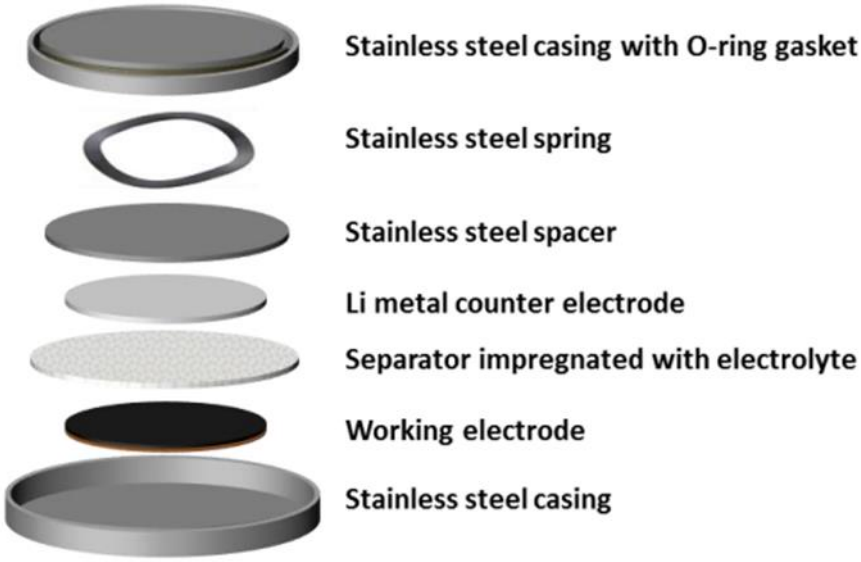

Figure 3.10 Diagram illustrating the coin cell setup.

Adapted from (Sole 2017).

3.6 Electrochemical characterisation

Various electrochemical characterisation techniques and instruments were employed to assess the assembled coin cells.

3.6.1 Battery testing system

In the ongoing research, the Neware battery tester, featured in **Figure 3.11**, operates as the battery testing system. This electrochemical workbench functions as a comprehensive apparatus for evaluating multiple battery cells simultaneously. Its advanced features include full automation, programmability, and the ability to handle multiple channels, ensuring the efficient testing of battery cells when they are integrated into a single unit. The program also incorporates protective measures, establishing safety thresholds to prevent overcharging and discharging of the cells.

This system typically operates by connecting to on-site computers and using software to capture the output data from the battery testing station. In the present study, galvanostatic charge-discharge profiles, cycle life evaluation, and rate performance of cells were assessed using a battery system.

In Chapter 4, the applied potential range covered from 3.0 to 0.001 V (opposed to Li/Li^+). Initially, the batteries were left to rest at open circuit potential (OCV) for a three-hour duration, after which they were discharged to 0.001 V. This discharge was conducted using a constant current constant potential mode (CCCV) with current densities of 0.1 A/g and 0.01 A/g. The initial charging and discharging formation cycles were carried out in constant current (CC) mode, maintaining a voltage range of 3 V to 0.001 V and a specific current flow of 0.1 A/g.

In Chapter 5, a voltage window from 1.5 to 0.01 V was applied. The batteries were initially allowed to rest at open circuit potential (OCV) for three hours and were subsequently discharged to 0.01 V. This discharge was performed using a constant current constant potential mode (CCCV) with current densities of

0.1 C and 0.01 C (1C = 350 mA h g^{-1}). The initial charging and discharging formation cycles were executed in constant current (CC) mode, maintaining a voltage span of 1.5 V to 0.01 V and a specific current flow of 0.1 C.

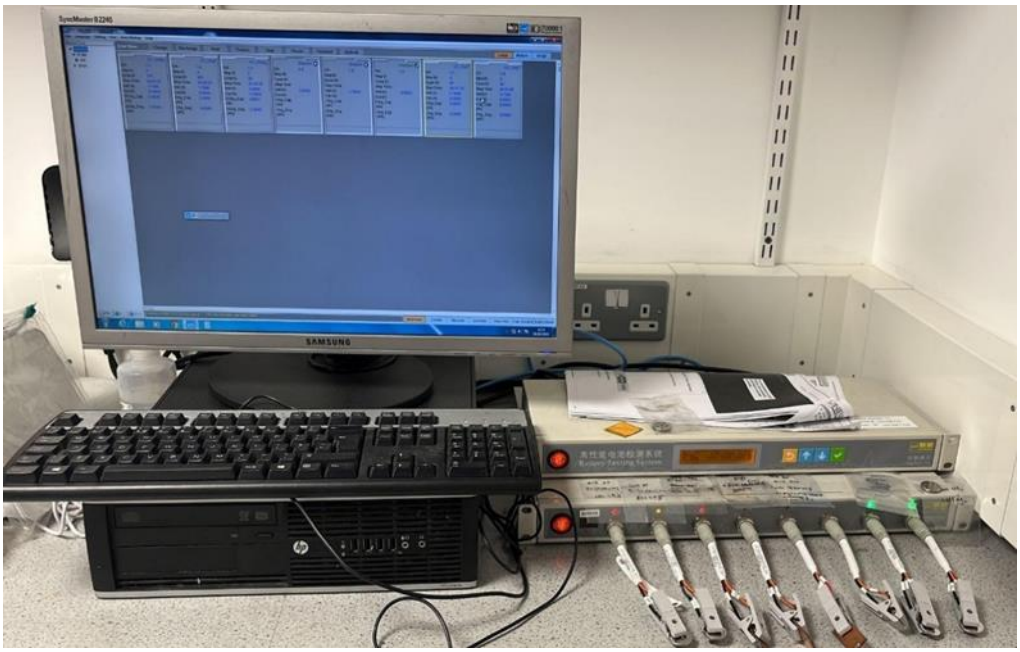

Figure 3.11 Neware battery tester, BTS 4000.

3.6.2 Electrochemical workstation

Electrochemical impedance spectroscopy (EIS) and cyclic voltammetry (CV) characterisation were conducted using an electrochemical workplace (Iviumstat, Ivium Technologies), as illustrated in **Figure 3.12**. Cyclic voltammetry (CV) analysis was carried out in Chapter 4 with a scanning power of 0.1 mV s^{-1} and cut-off potentials ranging from 3.0 to 0.001 V (contrasted with Li/Li^{+}). In Chapter 5, the analysis was carried out with a scanning power of 0.1 mV s^{-1}, and the cut-off potentials spanned from 1.5 to 0.01 V. The electrochemical impedance spectroscopy (EIS) analysis was carried out at a fixed amplitude of 5 mV, covering a frequency range of 0.01 Hz to 100 kHz. All the electrochemical tests were performed at room temperature.

Figure 3.12 Potentiostat (Ivium Technologies).

3.6.3 Graphical representation of electrochemical data

3.6.3.1 Cyclic voltammetry

Cyclic voltammetry (CV) measures the current response as the potential is varied, providing insight into the redox reactions occurring within batteries. During the analysis, the voltage is scanned between two defined potentials, V1 and V2 (the electrochemical window), at a rate of 0.1 to 10 mV/s. In this process, a voltammogram is produced (e.g., Figure 3.13), which shows two distinct peaks: anodic and cathodic.

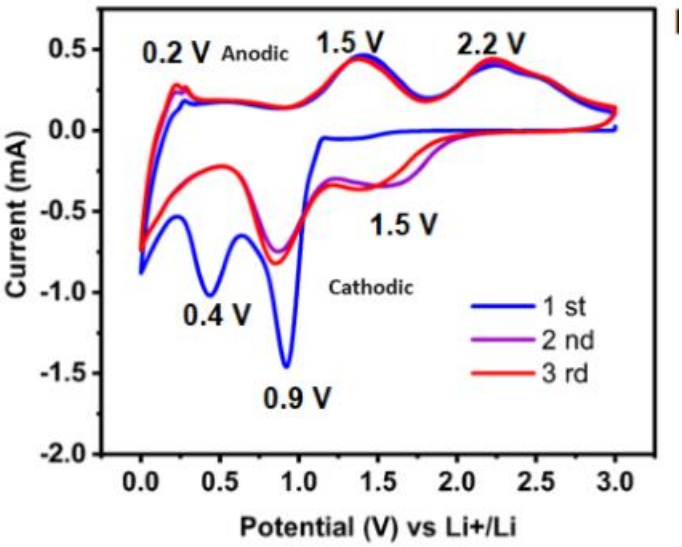

Figure 3.13 Sample CV of a NiO/graphene anode.

3.6.3.2 Voltage-Capacity Curves

Voltage versus Capacity curves are constructed with potential on the Y-axis and capacity on the X-axis. The presence of distinct potential plateaus on these graphs signifies the establishment of lithium intercalation and deintercalation compounds. The coin cell experienced galvanostatic charging and discharging at a specific current flow of 0.1 A/g, covering the voltage spectrum of 0.001–3.0 V (**Figure 3.13**). This graph illustrates that the discharge profile extends until the voltage reaches 0.001 V (Li/Li^+), while the charge profile continues until the voltage reaches 3 V (Li/Li^+).

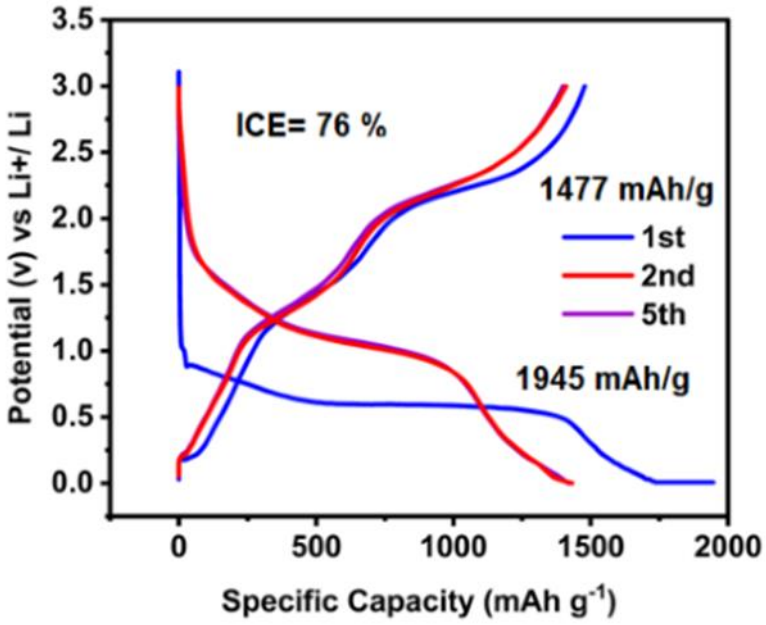

Figure 3.14 Sample voltage-capacity curve of a NiO/graphene anode.

An Excel spreadsheet is used to export the total charge and discharge capacities (mAh) and voltages. A graph is created using Origin data analysis software using the specific capacity (mAh/g) versus voltage (V) data points derived from the capacity data and divided by the active weight of the electrode sample.

3.6.3.3 Cycle life curves

Cycle life curves serve as indicators of battery lifetime, with the X-axis representing the number of cycles and the Y-axis depicting capacity. Greater cycling stability is typically observed when the anode material maintains its structural integrity over Li-ion insertion and extraction. In **Figure 3.14**, a coin cell undergoes 600 cycles of charge and discharge in the battery tester. Following data export to an Excel file, specific capacities are computed. Using Origin, discharge and charge capacities (mAh/g) are graphed. The graph reveals that both charge and discharge capacities decline as the number of cycles increases, primarily due to electrode degradation, excessive solid

electrolyte interphase (SEI) formation, Li-dendrite growth, and side reactions, among other factors.

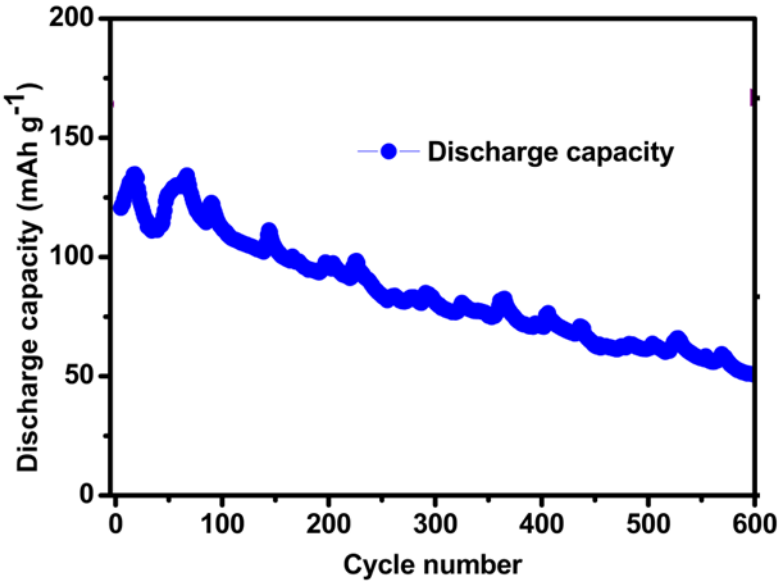

Figure 3.15 Sample cycle life curve of a graphene anode with Li reference.

3.6.3.4 Electrochemical Impedance analysis

The core layout of all batteries shares common components. Typically, electrodes consist of active materials and conductive additives, connected with a polymeric binder. Batteries also incorporate an electrolyte and a separator to prevent electrode contact. Analysing the impedance of the electrode and electrolyte serves as a valuable method for exploring battery kinetics. This approach not only facilitates the development of a functional kinetic model for the entire battery but also enables the assessment of each element's influence on the material's electrical performance.

Figure 3.15 provides an overview of the kinetic processes within a lithium-ion battery. These processes involve electronic conduction through the solid

materials and ionic conduction within the electrolyte, which occupies the spaces between the particles. Charge transfer resistance occurs at the electrode's interface, and ions diffuse into the interior of the electrodes, introducing solid-state diffusion impedance. During cycling, the creation of new crystalline structures can become a limiting factor in the kinetics, particularly at frequencies below 1 mHz. It's worth noting that **Figure 3.15** does not depict conduction through a porous separator or the electrolyte, which typically governs high-frequency performance above 10 kHz (Itagaki et al. 2004; Nazri and Pistoia 2008).

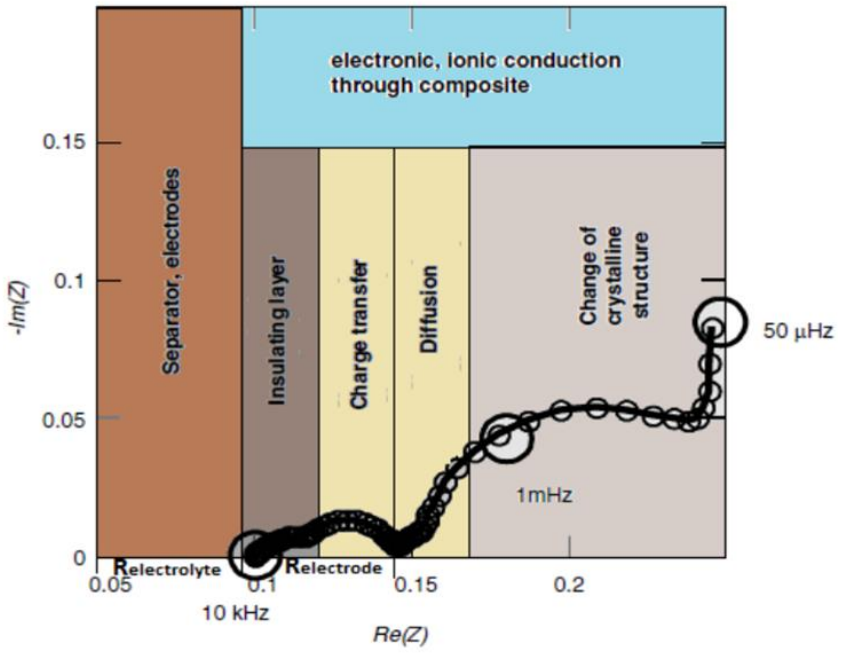

Figure 3.16 A sample impedance spectrum of an intercalation material. Adapted from (Cheekati 2011).

Chapter 4 Graphene-integrated NiO for Advanced Lithium-ion Batteries

4.1 Introduction

In recent years, LIBs have emerged as a highly efficient, and cost-effective energy source for mobile devices, portable electronics, and electric vehicles (EVs). Nevertheless, the industrial graphite presently utilised in LIBs falls short of meeting the modern market needs, primarily due to its limited nominal energy of approximately 372 mAh g^{-1}. In the quest for potential alternatives to graphite, the focus of research has turned to transition metal oxides (TMOs) including cobalt (Co), nickel (Ni), iron (Fe), copper (Cu), titanium (Ti), and zinc (Zn) oxides. These materials offer a notably higher energy density and exhibit an excellent storage capacity of around 700 mAh g^{-1}, as described by the chemical representation of $MO + 2Li^{+} + 2e = M + Li_2O$ (Huang et al. 2011; Ren et al. 2012; Qin et al. 2014; Li et al. 2016b; Li et al. 2020; Fernando et al. 2023).

Among the various oxides, nickel oxide (NiO) stands out as a particularly attractive candidate for use as an anode in LIBs. This choice is driven by its abundance, cost-effectiveness, eco-friendly nature, impressive safety profile, and high volumetric energy density. However, the practical application of pristine NiO, like other oxide materials, has been hampered by its inherent limitations, including inadequate electrical conduction, poor power characteristics, and limited lifespan (Rahman et al. 2022).

An effective protocol found in the literature involves the combination of NiO with carbon nanostructures. The incorporation of NiO into a carbon-based

composite design has proven to be advantageous for several reasons. It not only provides a larger surface area but also enhances electrical conductivity, offering desirable mechanical flexibility to counteract the volume expansion of NiO. Researchers have extensively investigated a variety of carbonaceous matrices, including graphite, graphene, hard carbon, carbon nanofibers, and carbon nanotubes (Iftikhar et al. 2022; Siddiqui et al. 2022).

For instance, Li et al. demonstrated that the capacity and capacity retention of pristine NiO can be significantly improved by integrating it into a graphene matrix. This innovative approach results in the establishment of a flower-like nickel oxide/reduced graphene oxide (NiO/RGO) nanocomposite, which boasts a specific Li-ion storage capability of 702.3 mAh g^{-1} and maintains a capacity retention of 77.0% even after 100 cycles at a specific current flow of 0.1 A g^{-1} (Li et al. 2018). Similarly, Shi et al. developed a 3D graphene/NiO nanobelt assembly, which substantially boosted both the volumetric and specific capacities of graphene by 75% and 41%, respectively. This composite exhibited an impressive cycling life of 360 cycles and a specific Li-ion storage capability of 445 mAh g^{-1} at a high specific current flow of 2 A g^{-1} (Shi et al. 2018). Additionally, an exciting study by Park et al. delved into coaxial carbon nanofiber/NiO core-shell nanocables, showcasing an exceptional reversible Li-ion storage capability of 825 mAh g^{-1} at a specific current flow of 0.2 A g^{-1} (Park and Lee 2015).

Despite the numerous efforts dedicated to the design of NiO/carbonaceous composites, several challenges persist in the quest for an ideal composite that can effectively address issues related to conductivity and synthesis procedures. An illustrative example of this challenge is encountered in the

synthesis of graphene/NiO composites, which often involve a multi-step process, raising concerns regarding the scalability and practicality of these materials. Another issue, as documented in the literature, revolves around the separation of composite components during the Li-ion cycling process, particularly with graphene and NiO. Over time, oxide nanoparticles tend to cluster together, leading to high local impedance and a significant reduction in capacity.

In this study, we introduce a nanocomposite anode featuring NiO on a 3D carbon network created by expanding graphite into nanoflower structures (referred to as NiO/GNF). This innovative approach capitalises on the synergistic interaction between NiO and the conductive carbon platform, resulting in a substantial enhancement in anode performance within Li-ion batteries. To elaborate on the key benefits of this novel design:

Firstly, the 3D carbon nanoflower backbone furnishes a generous surface area and exceptional conductivity to the active materials.

Secondly, NiO is partially integrated into the graphene, expanding the interlayer lattice distance, which, in turn, accelerates the transport of Li^+ ions and expands storage capacity.

Thirdly, the well-conceived nanoflower structure effectively accommodates volumetric changes during charge and discharge cycles, leading to a marked improvement in cycle life. These enhancements are examined in detail within the study.

4.2 Experimental section

In addition to the details in Chapter 3, this section outlines the specific methods employed in Chapter 4.

4.2.1 Chemicals and NiO/GNF nanocomposite synthesis

Nickel sulfate hexahydrate, sodium acetate trihydrate, and trisodium citrate were procured from Sigma Aldrich, UK. Natural flake graphite powder (100 mg, particle size <1 mm) was dispersed in a 40 mL aqueous solution containing 0.2 mol dm^{-3} nickel sulfate hexahydrate, 1 mol dm^{-3} sodium acetate trihydrate, and 0.5 mol dm^{-3} trisodium citrate. The resulting blend was subsequently moved into a Teflon-lined container within a stainless autoclave and subjected to heating at 200 °C for 20 hours. Following this, the residue was meticulously washed with de-ionized water and collected using vacuum filtration. Finally, the obtained samples underwent heat treatment at 350℃ for 12 hours to facilitate the conversion of the hydrothermal intermediate hydroxide product into NiO. For comparison, NiO and expanded graphitic nanomaterials (EG) were synthesized using the same methodology.

4.2.2 Electrode slurry preparation

The electrode slurry was prepared by mixing active material (70 wt. %), Super P (20 wt. %), and sodium carboxymethyl cellulose binder (10 wt. %, CMC, Sigma-Aldrich, 99%).

4.3 Results and Discussion

4.3.1 Material characteristics

Figure 4.1 exhibits a graphic representation of the proposed mechanism for the NiO/GNF. This study employed nickel salt and graphite powders as initial materials to produce nickel-integrated graphitic nanostructure.

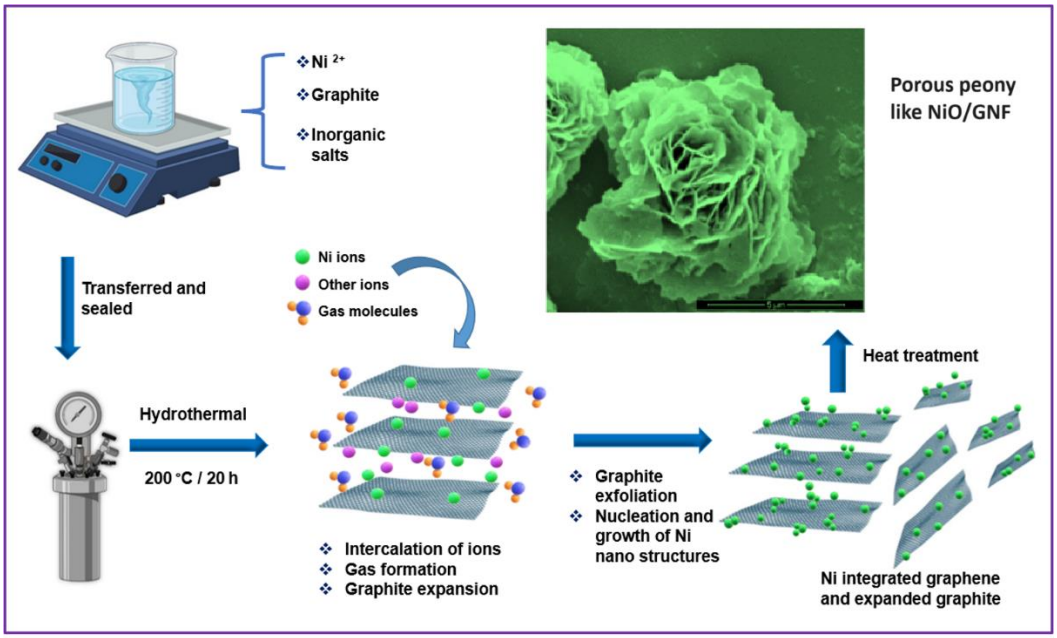

Figure 4.1 Synthesis of NiO/GNF

During the initial hydrothermal reaction, nickel, sodium, and citrate ions intercalate into the graphite matrix, yielding an intercalated graphite compound (GIC). Subsequently, gaseous substances confined between the layers of graphite are gradually released, causing an expansion in the interlayer spacing between the graphite sheets. The robust hydrothermal conditions, coupled with the continuous, in-situ generation of gases, further weaken the Van der Waals forces, leading to the formation of exfoliated graphitic nanosheets. At the same time, nickel ions in the hydrothermal environment initiate nucleation and growth, ultimately forming Ni nanostructures within the layers of graphite,

resulting in Ni-integrated expanded graphitic nanostructures. The synthesis of expanded graphite particles serves to effectively hinder the aggregation of Ni nanostructures, preserving a unique nest-like structure after synthesis. However, following the heat treatment, a noteworthy transformation in morphology occurs, leading to the development of peony-like 3D structures. This transformation can be attributed to the conversion of hydroxides into oxides and the expulsion of various gases throughout the process.

The X-ray diffraction (XRD) pattern, as shown in **Figure 4.2**, resembles that of NiO. Notably, the diffraction peaks located at 2-Theta angles of 37.4º, 43.3º, and 62.9º correspond to the (111), (200), and (220) crystallographic planes of cubic NiO, respectively, in line with the JCPDS reference code 43-1477. The measurement of the interplanar spacing (d-spacing) yielded a value of 0.24 nm for the peak at 43.3˚(Kottegoda et al. 2011).

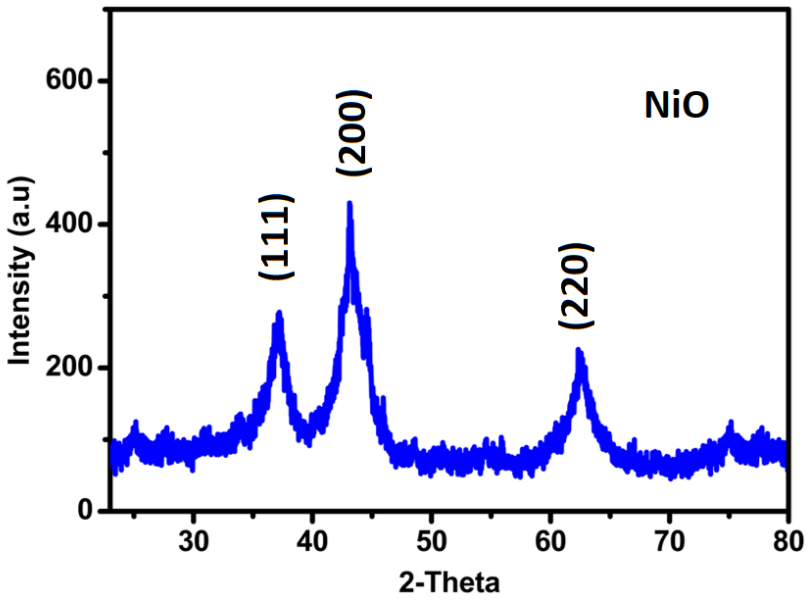

Figure 4.2 XRD analysis of NiO derived after hydrothermal treatment displaying peaks at 2-Theta 37.4º, 43.3º, and 62.9º corresponding to (111),

(200), and (220) planes of cubic NiO, respectively which matches with JCPDS 43-1477.

Furthermore, in the XRD pattern of the NiO-GNF nanocomposite (**as seen in Figure 4.3**), additional peaks at 26.6˚ and 54.79° are observed, attributed to the graphitic backbone, following JCPDS reference code 26-1080 (Jung et al. 2016).

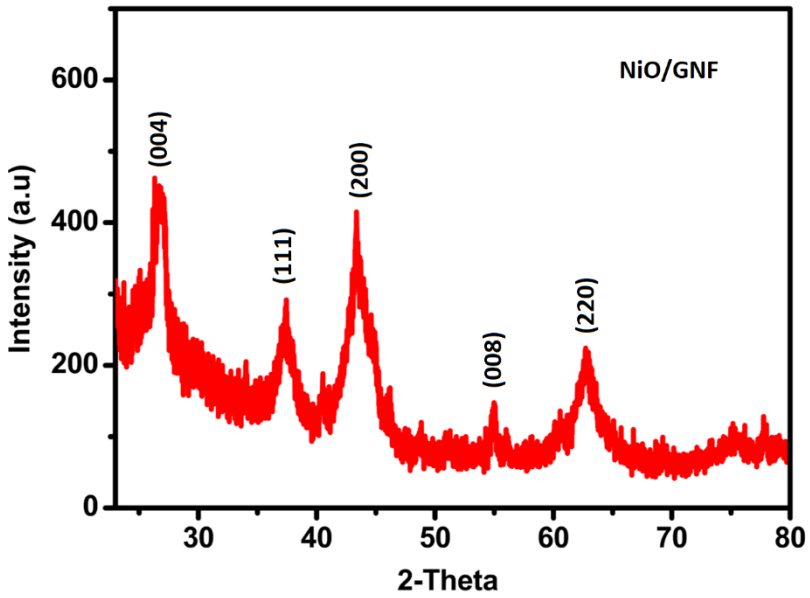

Figure 4.3 XRD analysis of NiO /GNF powders derived after hydrothermal treatment displaying additional peaks at 26.6˚ and 54.79° attributed to the graphitic backbone (JCPDS 26-1080).

Raman spectroscopic analysis also provides to verify the presence of the NiO phase within the NiO-GNF composite. As illustrated in **Figure 4.4**, two significant peaks are apparent in the petal of the peony-like structure, specifically a pronounced peak at approximately 500 cm^{-1} and a broad peak at around 1062 cm^{-1}. These peaks correspond to the NiO's first (1P) and second-order phonon (2P) scattering, respectively, consistent with previous findings (Kottegoda et al. 2011).

However, the presence of the graphene phase in the NiO/GNF composite was not observable in the Raman analysis due to its minor quantities. Therefore, XPS analysis was used to confirm the presence of the carbon phase in the NiO/GNF composite.

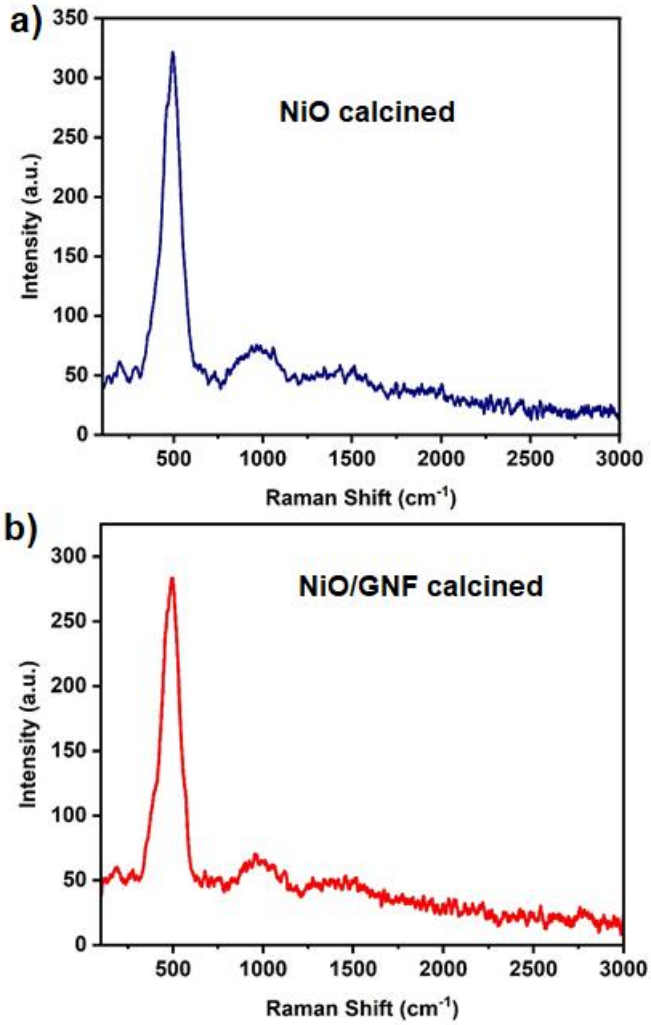

Figure 4.4 Raman spectroscopy analysis of (a) NiO and, (b) NiO-GNF composite.

X-ray photoelectron spectroscopy (XPS) was employed to determine the chemical valence states of the NiO-GNF composite and gain insights into their elemental compositions, as illustrated in **Figure 4.5**. In **Figure 4.5a**, the XPS

survey spectrum conclusively confirms the presence of carbon (C), nickel (Ni), and oxygen (O) within the composite. Furthermore, **Figure 4.5b** presents the C1s spectrum, revealing a distinctive binding energy at 284.8 eV, signifying the presence of sp^2-hybridized carbon through C-C bonds. In addition, two shadowy peaks emerge at approximately 285 and 288 eV, corresponding to the sp^3 hybridised C-OH and O-C-O bonds, respectively (Fernando et al. 2021).

The Ni2p spectrum in **Figure 4.5c** displays a unique splitting pattern resulting from spin-orbital coupling. Notably, binding peaks emerge at around 854 and 872 eV, accompanied by their respective satellite peaks at approximately 862 and 879 eV. These are attributed to the 2p3/2 and Ni 2p1/2 spin-orbit levels of NiO. Additionally, a shoulder peak at roughly 855 eV suggests the potential surface oxidation of NiO to Ni_2O_3 (Liu et al. 2015; Huang et al. 2017).

Turning to the O1s spectrum in **Figure 4.5d**, resulted in two prominent peaks at 529.4 and 531.7 eV. These peaks are attributed to metal-oxygen bonds, specifically O-Ni and C-O-Ni, demonstrating a clear link between the NiO and the graphitic framework that goes beyond ordinary physical or chemical adsorption due to the presence of strong chemical bonds (Huang et al. 2017).

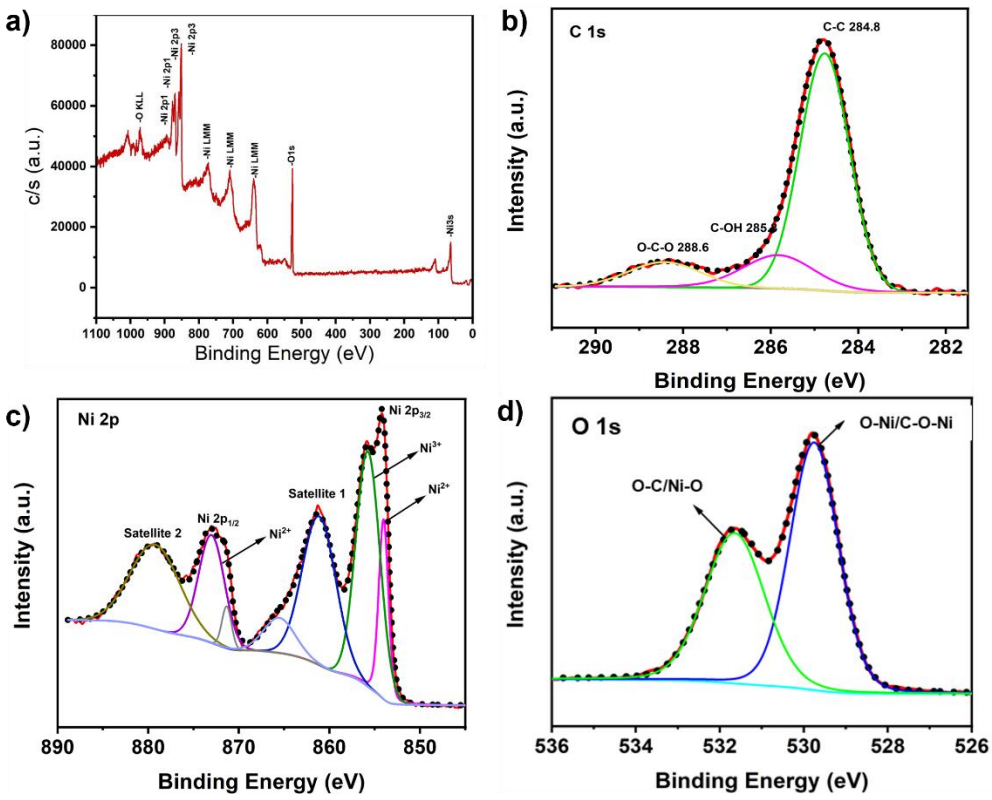

Figure 4.5 XPS spectra of NiO/GNF: a) survey spectrum, b) C 1s c) Ni 2p and d) O 1s.

Figure 4.6 presents scanning electron microscope (SEM) images depicting the transformations in the bulk NiO/graphite powders before and after undergoing the hydrothermal and calcination processes. Notably, the hydrothermal treatment brings about significant alterations in the surface morphologies, resulting in a crumpled, thin nano-sheet morphology of graphene, as illustrated in **Figure 4.6c**. Similarly, the NiO/GNF composite exhibits a highly porous structure with a pattern reminiscent of peonies, as showcased in **Figure 4.6d-f.**

Upon closer examination using higher magnification SEM (**Figure 4.6e&f**), we observe an interconnected petal-like morphology, characterized by a uniform distribution of exfoliated graphene sheets over these petal structures. This intriguing observation indicates the concurrent processes of nucleation of

nickel nanostructures and the gradual release of gaseous substances during the hydrothermal treatment, effectively transforming the bulk powders into well-organized structures wherein nickel oxide (NiO) encapsulates the graphitic nano framework (GNF).

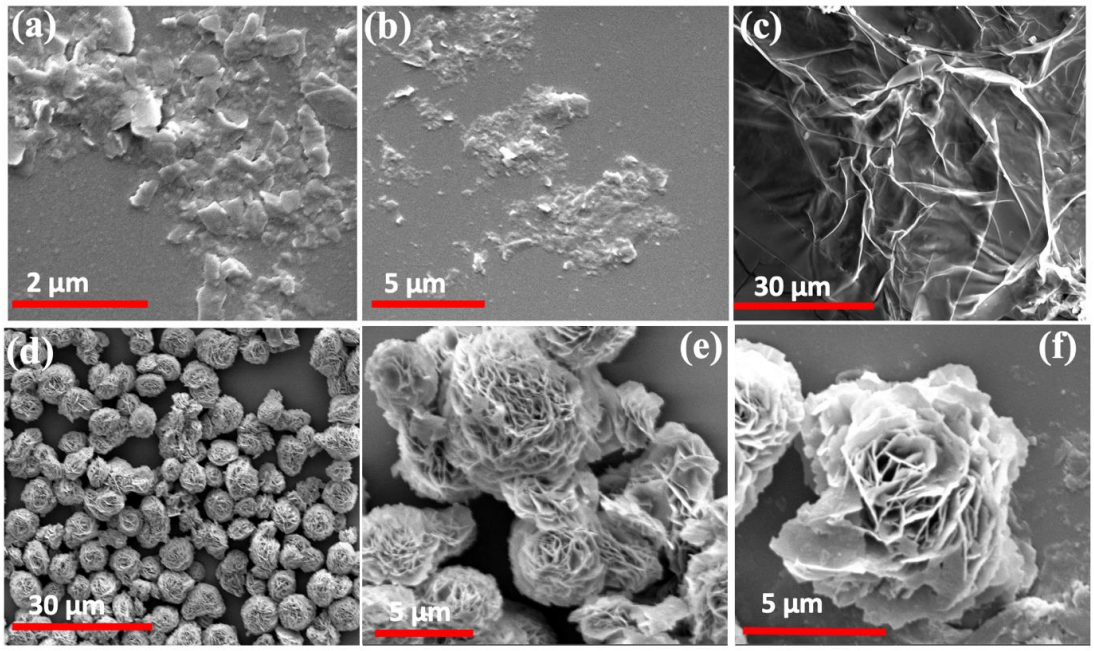

Figure 4.6 SEM images: (a and b) bulk NiO/graphite powders before hydrothermal treatment showing bulk particles and flakes, (c-f) corresponds to samples derived after hydrothermal process where (c) displays crumpled thin graphene nano-sheet, and (d-f) higher magnification NiO-GNF composite material displaying an interconnected petal morphology with uniform distribution of exfoliated graphene sheets encapsulated with NiO. Adapted from (Fernando et al. 2023).

To further validate the presence of carbon, nickel, and oxygen within the composite, SEM/EDX mapping (**Figure 4.7**) was conducted.

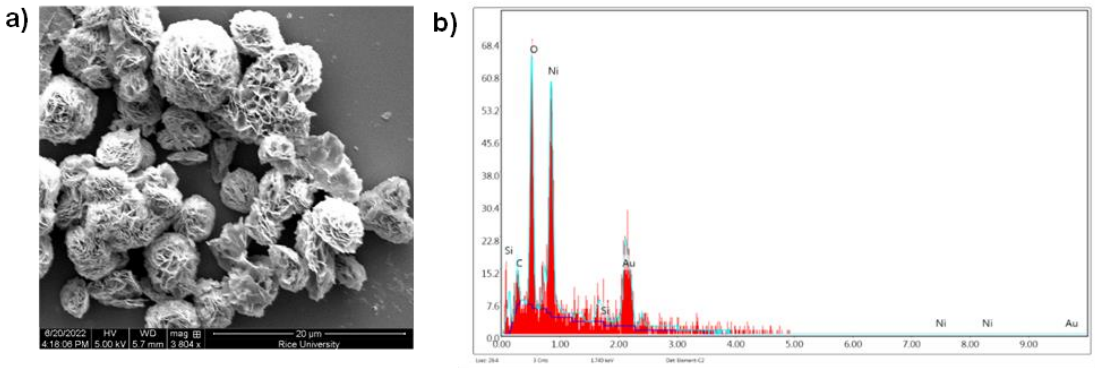

Figure 4.7 SEM/EDX analysis of NiO/GNF, confirms the presence of C, Ni and O elements.

Adapted from (Fernando et al. 2023).

As displayed in **Figure 4.8**, we performed a thermogravimetric analysis (TGA) under air to confirm NiO content in NiO/GNF composite. The first weight loss of around 3.9% could be due to the removal of water and the successive second and third losses of ~ 34.12% may arise from Ni $(OH)_2$ and expanded graphite respectively. The residual mass represents the content of NiO in the composite as ~ 61.98%.

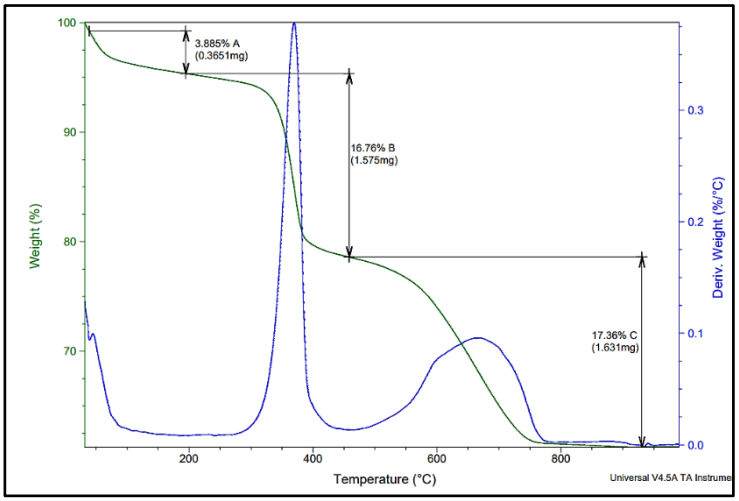

Figure 4.8 TGA interpretation of NiO/GNF.

Adapted from (Fernando et al. 2023).

To understand the process of graphite peeling into thin graphene nanoplatelets during the hydrothermal treatment, Transmission Electron Microscopy (TEM) analysis was conducted, as depicted in **Figure 4.9a-k**. **Figure 4.9a** reveals the stacking of multilayer graphene sheets, and in **Figure 4.9b**, we observe the presence of scattered NiO particles displaying a distinctive white patch-like morphology.

To affirm the exfoliation of graphite, we conducted measurements of the interlayer spacing at three distinct regions, as indicated in the inset of **Figure 4.9c**. These measurements yielded the following values: (i) 0.33, (ii) 0.36, and (iii) 0.37 nm. These reflections are characteristic of morphed graphene and correspond to the (110) crystallographic planes, aligning with the XRD peak observed at approximately 26º (2θ). The increase in interlayer spacing can be attributed to the expansion of layers during the hydrothermal treatment and subsequent calcination step.

Furthermore, TEM-EDS mapping was employed to analyse the NiO-GNF samples and confirm the presence of various elements. The results of this analysis are depicted in **Figure 4.9g-k**. Notably, the TEM-EDS results exhibit a uniform distribution of carbon (C), nickel (Ni), and oxygen (O) elements, conclusively confirming the feasibility of transforming bulk graphitic structures into few-layered graphene sheets encapsulated with NiO.

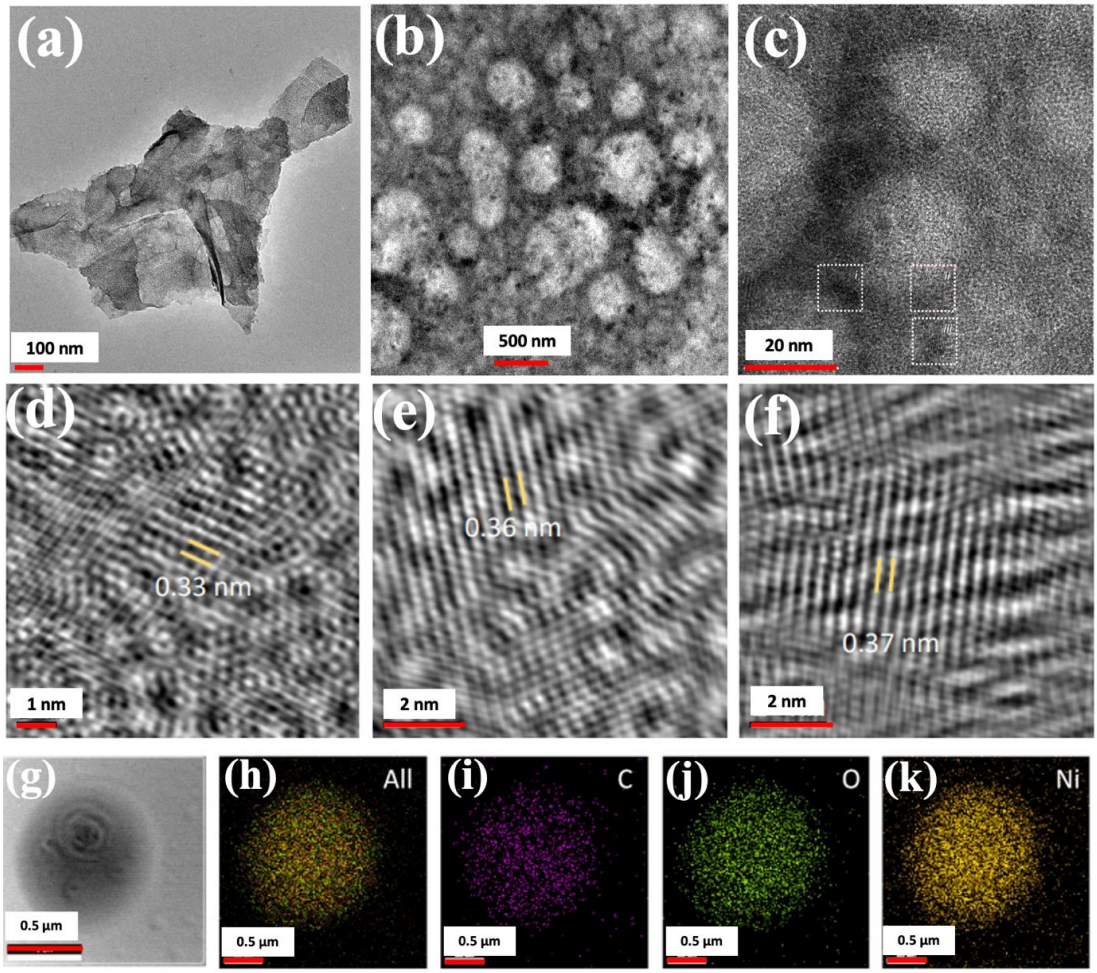

Figure 4.9 TEM images of derived samples (a) exfoliated graphene sheets; (b) displays the presence of scattered NiO nanoparticles (c) displays d-spacing values taken at three different regions (marked i, ii, and iii) correspond to differences in interlayer spacings at various spots where (d) show 0.33 nm, (e) 0.36 nm and (f) 0.37 nm. TEM-EDS mapping area is shown in (g), and (h) shows the presence of all expected elements where (i) corresponds to carbon, (j) oxygen, and (k) nickel.

Adapted from (Fernando et al. 2023).

There is no doubt that surface area and pore hierarchy play a significant role in Li-ion transport. Consequently, we conducted nitrogen adsorption-desorption analysis to assess modifications in the pore size distribution and

surface measurements of both the NiO/GNF composite and pristine NiO. Both materials exhibited characteristic type IV isotherm curves, indicative of the presence of mesoporous characteristics. However, a distinctive difference emerged: the NiO/GNF sample demonstrated a multistage pore size distribution, evidencing the presence of micro, meso, and macro pores within the composite. In contrast, pristine NiO was predominantly microporous, with pore sizes measuring less than 2 nm. This discrepancy in pore size characteristics can likely be ascribed to the loss of organic oxygen and hydrogen groups during the hydrothermal treatment, while graphene contributed to the growth of mesopores.

Quantitatively, the NiO/GNF composite boasted a higher total pore volume, an increased average pore diameter, and a greater specific surface area, measuring 0.33 $cm^3 g^{-1}$, 7.29 nm, and 178 $m^2 g^{-1}$, respectively. In contrast, the values for the pristine sample were 0.13 $cm^3 g^{-1}$, 6.06 nm, and 82.9 $m^2 g^{-1}$, respectively (as depicted in **Figure 4.10**).

The presence of a multistage size distribution and the greater surface area in the NiO/GNF composite strongly suggest an enhancement in Li-ion migration and a comparatively higher capacity for Li-ion storage. These characteristics are highly advantageous for the fabrication of high-capacity energy storage materials.

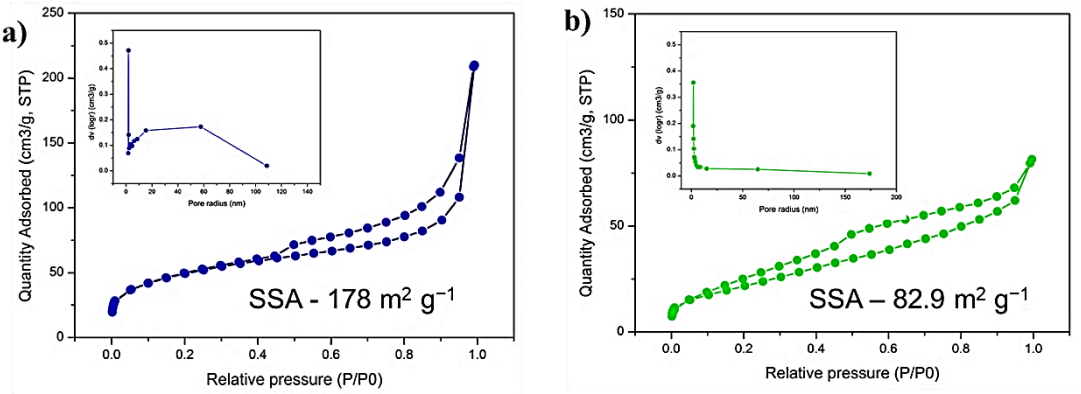

Figure 4.10 Adsorption-desorption isotherms and pore size distribution of a) NiO/GNF and b) pristine NiO. The NiO/GNF sample displayed increased specific surface area which assisted in enhanced Li-ion transport. Adapted from (Fernando et al. 2023).

4.3.2 Electrochemical characteristics

The electrochemical analysis was conducted on the synthesised NiO-GNF as an anode in a two-electrode half-cell Lithium-ion battery setup, using Li foil as the counter electrode. For comparison, we also assessed the characteristics of pristine exfoliated graphene (EG) and NiO, as shown in **Figure 4.11**. The cyclic voltammetry (CV) measurements were carried out within the voltage range of 0.001–3 V (vs. Li^+/Li), employing an intentionally slow scan rate of 0.1 mV s^{-1}. **Figure 4.11a-c** provides insight into the initial three CV cycles of EG, NiO, and NiO-GNF.

In the first cathodic scan (**Figure 4.11a**), EG displays a minor peak at approximately 1.3 V, which is associated with the reductive degradation of the electrolyte and the subsequent establishment of a solid electrolyte interface (SEI) (Sivakkumar et al. 2010). Additionally, a noticeable reduction at 0.1 V indicates the intercalation of lithium ions into the multilayer graphene. At

around 0.4 V, a sharp oxidation peak is observed, corresponding to the de-intercalation of Li-ions from the LiC_x complex (Zhong et al. 2020a).

In contrast, both NiO and NiO/GNF share several CV peaks, emphasizing the dominant contribution of NiO (**Figure 4.11b and c**). Both materials exhibit a cathodic peak at 0.4 V vs. Li^+/Li, which signifies the irreversible establishment of SEI and the reduction of NiO (Cao and Wei 2015). However, the peak is notably more pronounced for pristine NiO in comparison to NiO/GNF, suggesting catalytic activity of NiO in electrolyte decomposition and the establishment of an additional SEI layer (Wang et al. 2017).

Additionally, the initial cathodic scans of both NiO and NiO/GNF systems reveal two recurring oxidation peaks at 0.6 V and 0.9 V, along with another peak at 1.4 V. These observations indicate the presence of NiO traces in both electrodes, which undergo reduction during the first cathodic scan.

The reduction process observed can be linked to the conversion of NiO into metallic Ni and nickel suboxides, represented by the following electrochemical reaction: $NiO + 2Li^+ + 2e \rightarrow Ni + Li_2O$ + Ni suboxides (Li et al. 2018; Chen et al. 2019). In addition to this, we observed that the intensity of the peak at 0.9 V is significantly stronger and shifted in the case of NiO/GNF as compared to pristine NiO, indicating an increased lithiation capacity. This enhanced capacity can be attributed to the intercalation of lithium with the graphene sheets, resulting in improved electrical conductivity and faster electron transfer kinetics (Ou et al. 2021).

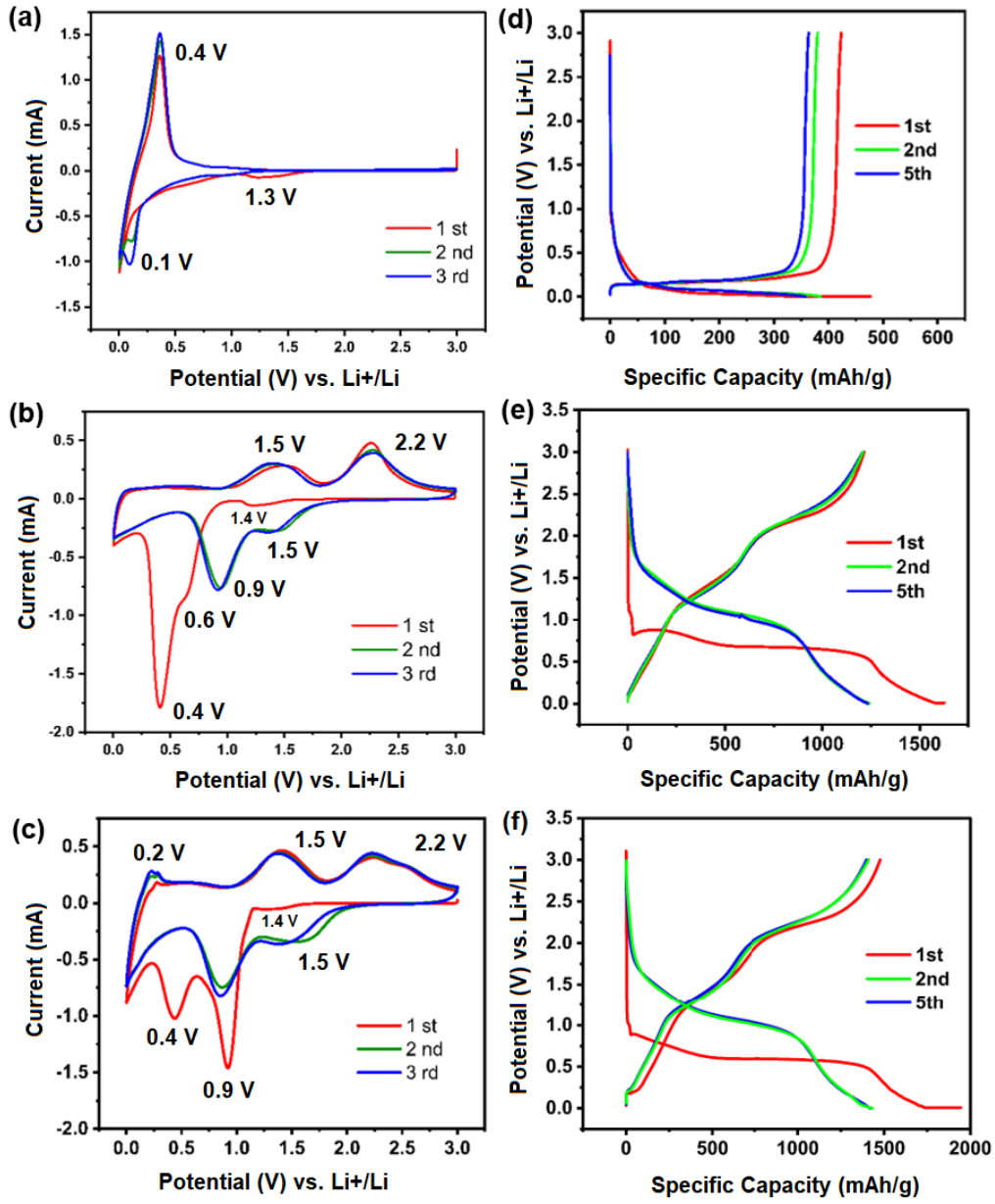

Figure 4.11 Cyclic voltammetry profiles: (a) EG, (b) NiO, and (c) NiO/GNF at a scan rate of 0.1 mV s^{-1} in the voltage range of 0.001–3.0 V. The discharge/charge profiles: (d) EG, (e) NiO, and (f) NiO/GNF in the 1st, 2nd, and 5th cycles in the potential range of 0.001–3.0 V at 0.1 A g^{-1}. Adapted from (Fernando et al. 2023).

The cathodic peak observed at 1.4 V in both systems has shifted towards a more positive potential of 1.5 V in subsequent cycles, which is likely related to

the formation of various nickel suboxides during the first cycle (Li et al. 2018). As for the anodic oxidation peaks at 1.5 and 2.2 V in both NiO and NiO/GNF systems, they can be associated with the oxidation of nickel or nickel suboxides back into NiO according to the following reaction: Ni + Ni suboxides + $Li_2O \rightarrow NiO + 2Li^+ + 2e$.

Furthermore, in the NiO-GNF system, a recurring mild oxidation plateau was observed at 0.2 V, a phenomenon that is not present in the pristine NiO (Shi et al. 2018). This observation may be attributed to the de-intercalation of Li-ions from the graphitic structures, representing an additional aspect of the electrochemical behaviour of the NiO/GNF system.

Figure 4.11d-f presents the galvanostatic charge/discharge curves recorded at a specific current flow of 0.1 A g^{-1} after the 1st, 2nd, and 5th cycles. Notably, the EG samples exhibit a first discharge Li-ion storage of 476.8 mAh g^{-1} and a charge capacity of 423.1 mAh g^{-1}, resulting in an initial Coulombic efficiency (ICE) of 88.7%. This comparatively higher capacity of EG can be recognised for the improved electrical conduction of graphene nanoplatelets and the enhanced ion storage capacity, thanks to the enlarged interlayer spacing.

Similarly, for the pristine NiO, the initial discharge and charge capacities were 1626 mAh g^{-1} and 1214 mAh g^{-1}, respectively, with an ICE of 74.6%. However, in comparison to the NiO samples, the NiO/GNF composite exhibited significantly higher initial discharge and charge capacities, measuring 1945 mAh g^{-1} and 1477 mAh g^{-1}, respectively, along with an enhanced ICE of 76%.

In the subsequent discharge cycles of the three LIBs, it's evident that the capacity was lower than that of the first cycle. This reduction in capacity can be attributed to the irreversibility of the Solid Electrolyte Interface (SEI)

formation and the presence of some undecomposed Li_2O phases, which aligns with the cyclic voltammetry (CV) results.

Furthermore, during the 5th cycle, the pristine NiO achieved a discharge/charge capacity of 1236/1207 mAh g^{-1} with excellent Coulombic efficiency (CE) of 97.6%. Similarly, the discharge/charge capacities of NiO/GNF were 1437 mAh g^{-1} and 1415 mAh g^{-1}, respectively, resulting in a superior CE of 98.5%. This enhancement in CE is attributed to the synergistic effect of NiO/GNF, which has been widely observed in previous studies (Li et al. 2018; Ou et al. 2021).

Additionally, it's worth noting that the increased interlayer distance in expanded graphite can contribute significantly to the observed capacitive behaviour. Furthermore, the fact that the 2nd and 5th discharge curves of both NiO and NiO/GNF overlapped suggests more active material utilisation over the cycling, indicating an improvement in electrode conditioning.

Then the rate capability of the NiO/GNF electrode was evaluated and compared with the performance of EG and pristine NiO electrodes, as depicted in **Figure 4.12**. The NiO/GNF electrode displayed average capacities of 1429, 1287, 1148, 1008, 821, and 752 mAh g^{-1} at various specific currents of 0.1, 0.2, 0.5, 0.8, 1, and 1.2 A g^{-1}, respectively. The recorded capacities for the NiO-GNF electrode at different current densities consistently outperformed those of EG and pristine NiO, illustrating fast electrochemical kinetics credited to the synergistic properties of NiO and the graphitic nanomaterials (as detailed in **Table 4.1**).

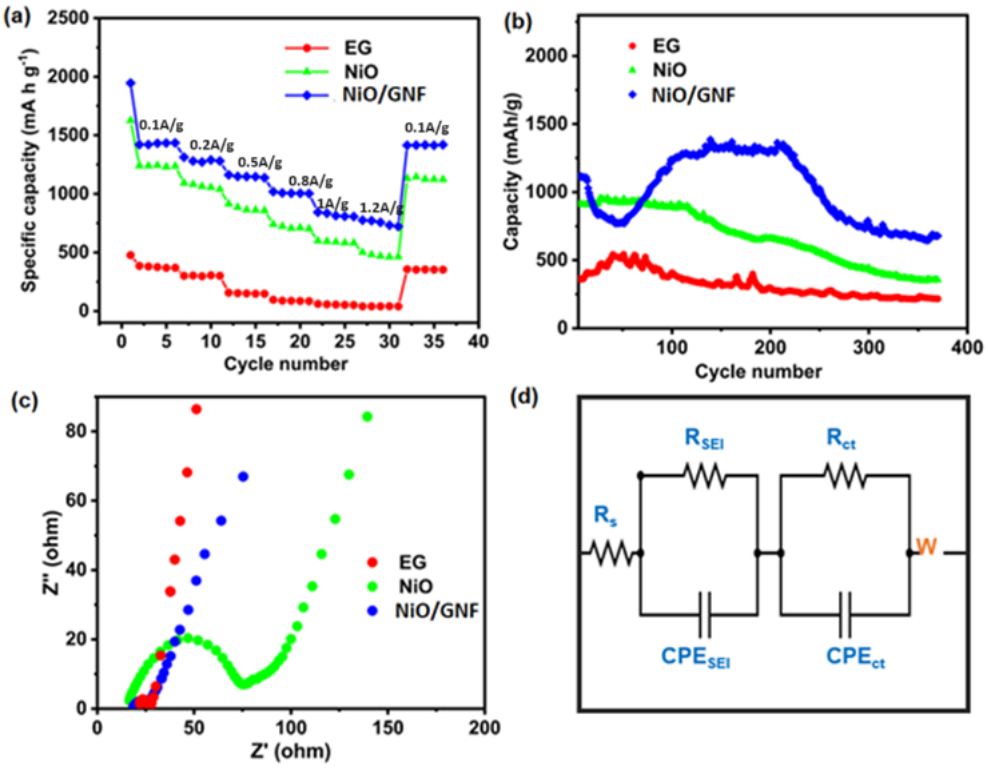

Figure 4.12 Lithium-ion battery performance of EG, NiO, and NiO/GNF. (a) Rate capability at different current densities, (b) Long-term cycling at 0.5 A g-1 in the voltage range of 0.001–3.0 V, (c) The electrochemical impedance spectroscopy after the 5th cycle in the frequency window from 100 kHz to 0.01 Hz, and (d) The equivalent circuit of the cells used to simulate EIS curves.

Adapted from (Fernando et al. 2023).

Table 4.1 The average capacity comparison of EG, NiO and NiO/GNF at various current densities.

Current density / (A g^{-1})	**EG (mAh g^{-1})**	**NiO (mAh g^{-1})**	**NiO/GNF (mAh g^{-1})**
0.1	376	1239	1429
0.2	302	1095	1287
0.5	152	904	1148

0.8	89	740	1008
1	56	589	821
1.2	41	475	752
0.1	354 (CR, 94.3 %),	1130 (CR, 91.2%)	1408 (CR, 98.5 %)

Notably, when cycling at a specific current flow of 0.1 A g^{-1}, the NiO/GNF electrode almost fully recovered its initial capacity, highlighting its exceptional rate capability. In comparison, the NiO electrode achieved approximately 91.2% capacity recovery, indicating the role of the GNF backbone in enhancing the electrode's electrical conductivity and structural integrity.

Furthermore, at an ultra-high specific current flow of 1.2 A g^{-1}, the NiO-GNF electrode exhibited an energy of 752 mAh g^{-1}, which was slightly higher than the nominal capacity of NiO (i.e., 718 mAh g^{-1}). This result emphasizes the excellent rate capability of the NiO-GNF composite. This achievement highlights the exceptional performance of the NiO-GNF composite in terms of rate capability and signifies a significant advancement in electrochemical performance (**Table 4.2**)

The cyclic stability of the materials was assessed and exhibited notably superior performance when compared to pristine NiO, as demonstrated in **Figure 4.12b**. The composite electrode displayed an impressive capacity of 678.2 mAh g^{-1} after 370 cycles at a specific current flow of 0.5 A g^{-1}, equating to a remarkable 60.7% retention of its 6^{th} cycle capacity. In contrast, the EG electrode delivered a Li-ion storage capability of 86.6 mAh g^{-1} completing the

same 370 cycles, while the pristine NiO experienced a substantial capacity decline and ultimately provided a capacity of 354 mAh g^{-1}.

It's noteworthy that the NiO/GNF electrode displayed an intriguing upward trend in capacity after approximately 50 cycles. Such a phenomenon has been previously observed in various transition oxides/carbon composites and can be attributed to the enhanced diffusion of Li^+ ions into the internal structures of the NiO/GNF composites. The electrochemical performance of NiO/GNF is highly promising, especially when compared to recent reports on NiO/carbon composites as Li-ion battery anode materials (as summarized in **Table 4.2**).

Table 4.2 Comparison of NiO/carbon composites as Li-ion battery anode material. Symbols > and ~ are used to estimate values from graphs in references where exacts are not stated.

Material	**NiO (wt. %)**	**Rate capability (mAh/g) / (A/g)**	**Cycling performance (mAh/g)/ (A/g), CR, cycles**	**Ref.**
NiO/GNF	61.98	752/1.2	678.2 / 0.5, 60.7 %, 370 cycles	This work
NiO/3DGS	26.8	445/2	416/2, 112.7 %, 515 cycles	(Shi et al. 2018)
NiO/RGO	86.12	564.5/0.8	702.3/0.1, 77 %, 100 cycles	(Li et al. 2018)
NiO@graphene	-	711/10	205/0.05, ~ 20.5 %, 500 cycles	(Ou et al. 2021)
NiO@CMK-3	45.1	824/0.8	848/0.4, 90.2 %, 50 cycles	(Fan et al. 2015)

NiO/N-graphene	56.44	~ 600/1.6	1105/0.08, 138.1 %, 150 cycles	(Chen et al. 2017)
NiO/C arrays	93.3	~1200/1	~1250/1, >90 %, 200 cycles	(Feng et al. 2016)
Graphene@NiO@carbon	59.5	580/1.6	754/0.2, 74.7 %, 50 cycles	(Wang et al. 2016)
Eggshell-yolk NiO/C porous composite	~85.7	400.1/0.8	625.3/0.1, 94.1%, 100 cycles	(Li et al. 2017 a)

To gain further insights into these observations, electrochemical impedance spectroscopy (EIS) was conducted, and **Figure 4.12d** illustrates the equivalent circuit used to interpret the EIS results. In this equivalent circuit, the high-frequency intercept (R_s) signifies the ohmic resistance of the electrolyte due to the formation of surface films. Additionally, the diameter of the semi-circle signifies the R_{SEI}, which is the resistance associated with the Solid Electrolyte Interface (SEI) growth, and R_{ct}, the charge-transfer impedance at the electrode/electrolyte border related to Li-ion movement. It's important to note that the depressed semicircles indicate the presence of non-uniform surfaces, hence a constant phase element (CPE) is used in the equivalent circuit instead of a pure capacitance. Consequently, CPE_{SEI} and CPE_{ct} correspond to the SEI and double-layer capacitance, respectively, while the Warburg impedance (W) is attributed to Li-ion diffusion (Reddy et al. 2010; Sakunthala et al. 2011).

The remarkably low R_{ct} for NiO/GNF electrodes, measuring just 0.636 Ω, stands in contrast to the considerably higher resistance of NiO, which registered at 44.7 Ω (as illustrated in **Figure 4.12c**). These findings provide

clear evidence that the NiO/GNF composite exhibits superior electrochemical kinetics, benefiting from the successful integration of exfoliated graphene. Additionally, the smaller semi-circle observed in the NiO/GNF electrode confirms the controlled pulverisation of NiO and effectively inhibits the further growth of the SEI layer, corroborating the cyclic voltammetry results. These outcomes highlight the improved performance and stability of the NiO-GNF composite electrode.

4.4 Conclusions

In summary, this study investigated a one-step simple hydrothermal synthesis approach to fabricate a NiO/GNF composite material. This process involved the transformation of graphitic particles into graphene nanosheets that encapsulated NiO nanoparticles within their carbon network. We thoroughly characterised the chemical nature and surface morphology of the resulting NiO/GNF composite material through various analytical techniques.

The integration of expanded graphite with NiO nanostructures yielded significant improvements in electrochemical performance, electrode integrity, Li-ion storage capacity, and the ability to withstand electrode stress. The synergistic interaction between expanded graphite and NiO led to a remarkable 22.4% increase in capacity retention and a substantial Li-ion storage improvement of 324 mAh g^{-1} compared to pristine NiO in Lithium-ion batteries.

To the best of our knowledge, the electrochemical performance of NiO-GNF, achieving approximately 678.2 mAh g^{-1} at a specific current flow of 0.5 A g^{-1} over 370 cycles, represents a significant advancement compared to previously

reported carbon-based NiO composites. In conclusion, the derived material stands out as an exceptional electrode due to its ease of synthesis, scalability, enhanced capacity retention, and remarkable long-term cyclability.

The limitations of this research include the lack of full cell testing of the NiO/GNF composite with a cathode material. Conducting such tests would provide a better understanding of the electrochemical performance of the anode in a commercially relevant context. Additionally, post-mortem analysis of the electrodes would be beneficial for understanding the ageing mechanisms of the composites.

Chapter 5 Graphene Incorporated Si for Lithium-ion Batteries.

5.1 Introduction

The demand for the new generation LIBs is continuously growing due to their increasing potential use in electric vehicles and modern electronic devices (Gaines and technologies 2018). LIBs offer significant electrochemical advantages, including high voltage availability, excellent energy/power density, prolonged cycling life, and sustainability compared to non-renewable fossil fuels (Duan et al. 2020). Thus, LIBs provide various applications with a compelling alternative. However, conventional LIBs with the graphite-based anode and the metal oxide cathode ($LiCoO_2$) have reached their maximum nominal gravimetric capacity limitations of 372 mAh g^{-1} and 274 mAh g^{-1} correspondingly (Sun et al. 2006; Writer and Batteries 2019). Unfortunately, the current commercial goal of achieving a half-cell coating energy of 1000 mA h g^{-1} is undoable for these traditional materials. Hence, there has been significant research and development on developing cutting-edge LIBs with extended cycle life, excellent energy density, and lightweight to satisfy the growing energy demands of current technologies.

The electrochemical performances of LIBs depend on the characteristics of anode and cathode materials together, while the anode contributes significantly to increasing the capacity (Wu et al. 2019). Despite the popularity, low energy density and poor cycle life of graphite anode still hinder the LIB performance. According to theoretical studies, the conversion of high-dimensional conventional graphite into carbon nanomaterials has

demonstrated enhanced electrochemical performances (Fang et al. 2017; Cheng et al. 2017; Canal-Rodríguez et al. 2018). As a result, graphene was introduced as a new-generation anode with a comparatively high nominal Li-ion storage of 744 mA h g^{-1} based on the Li_2C_6 stoichiometry (Hu et al. 2020). Despite the excellent theoretical capacity, the utilisation of pristine graphene electrodes has not translated into significant improvements in practical lithium-ion battery (LIB) applications (Betti et al.).

Silicon (Si) holds great promise as a future anode material for LIBs due to its exceptional nominal lithium-ion storage of about 4200 mAh g^{-1}, a significant improvement over the widely used commercial graphite with a 372 mAh g^{-1} energy. However, the practical application of Si as a LIB anode faces significant challenges. These obstacles stem from Si's inherent limitations, including poor electronic conductivity and substantial volume changes exceeding 400% during lithiation and delithiation processes. These issues lead to the fragmentation of Si particles and disconnection from the current collector, resulting in a rapid capacity decrease (An et al. 2019b).

To address these challenges, one of the effective strategies is to incorporate graphene into the Si as discussed in previous Chapter 2.

In this section, we introduce a cost-effective and scalable hydrothermal exfoliation approach to synthesising exfoliated graphene composite (EG) from natural flake graphite. In contrast to other common techniques like Chemical Vapor Deposition (CVD) (Yi and Shen 2016), which is significantly expensive and requires elevated temperatures, and electrochemical exfoliation, which involves high-energy processes and the use of hazardous organic solvents,

the hydrothermal exfoliation approach is distinct. It utilises only inorganic salts and operates under aqueous conditions (Rizwan and Gwenin 2021).

To create a nanocomposite incorporating silicon (Si) nanoparticles, exfoliated graphene and Si nanoparticles were combined in various proportions. The influence of the mass ratio between Si and exfoliated graphene on the electrochemical performance of the anodic lithium-ion battery was studied, to determine the optimal Si to exfoliated graphene ratio.

5.2 Experimental

In addition to the methods described in Chapter 3, the following were applied.

5.2.1 Chemicals

Sodium acetate trihydrate, trisodium citrate, sodium carboxymethyl cellulose (CMC) and Si nanoparticles (< 100 nm) were purchased from Sigma Aldrich, UK. Natural flake graphite powder (100 mg, <1 mm) and styrene-butadiene rubber (SBR) were obtained from Talga Technologies Ltd, UK. Super P conductive carbon black, lithium chips (diameter-15.6mm, thickness - 0.45 mm) and 1M lithium hexafluorophosphate (LiPF6) salt in ethylene carbonate/ ethyl methyl carbonate solvent mixture (50:50, v/v) was purchased from MTI Corporation. The glass microfiber filters were obtained from Whatman (GF/B, pore size- 1.0 µm).

5.2.2 Sample preparation

Graphene/Si composite was synthesised using a hydrothermal technique. To prepare the mixture, the graphite powder was stirred with 40 mL of a trisodium citrate solution with a concentration of 0.5 mol dm^{-3}, along with a sodium

acetate trihydrate solution with a concentration of 1 mol dm^{-3}, in an aqueous medium. Subsequently, the obtained solution was subjected to heating for 20 hours at a temperature of 200 °C, utilising a stainless-steel autoclave that was internally lined with Teflon. Following the hydrothermal exfoliation process, the resultant product was allowed to cool, and the final powder was obtained by rinsing it with de-ionized water and subsequently collecting it via vacuum filtration. Any remaining impurities were removed by heating the product at 200°C for 12 hours.

Next, Si-EG composites were synthesised by mixing the above-exfoliated graphene composite with Si nanoparticles. The composites were prepared in three different weight percentages of Si: 10Si-EG, 30Si-EG, and 50Si-EG, which contained 10%, 30%, and 50% of Si respectively.

5.2.3 Electrode slurry preparation

The lithium-ion battery electrochemical performance of Si-EG composites was assessed using 2032-type coin cells. The slurry solutions of 10Si-EG, 30Si-EG, and 50Si-EG were prepared by combining the active materials with CMC (carboxymethyl cellulose), SBR (styrene-butadiene rubber), and Super P conductive carbon black as described in **Table 5.1** (Sun et al. 2016b).

Table 5.1 Materials used in electrode preparation.

Composite	**Active materials wt. %**		**CMC wt. %**	**SBR wt. %**	**Super P carbon black wt. %**
	Si	EG			
10Si-EG	10	70	5	5	10
30Si-EG	30	50	5	5	10
50Si-EG	50	30	5	5	10

For comparison, natural graphite (NG) and EG anodes were made by combining active material (80 wt. %), CMC (5 wt. %), SBR (5 wt. %) and Super P conductive carbon black (10 wt. %).

5.3 Results and discussion

5.3.1 Material analysis

Figure 5.1 demonstrates a graphic illustration outlining the proposed process for synthesising exfoliated graphitic materials from natural graphite flakes by hydrothermal exfoliation. This study utilised bulk natural graphite powder as raw material to produce graphene and expanded graphite composite. During the initial stage of the high-temperature hydrothermal process, sodium and citrate ions penetrate between the layers of bulk graphite, leading to the establishment of a graphite-intercalated compound (GIC). In the following stages, the gaseous substances that have been confined between the graphitic layers gradually release, causing an expansion of the interlayer spacing between the graphitic sheets. The synergistic effect of rigorous hydrothermal conditions and the in-situ generation of gases results in the weakening of Van der Waals forces among graphite layers. This, in turn, leads to the exfoliation of graphite into graphene (Yang et al. 2019).

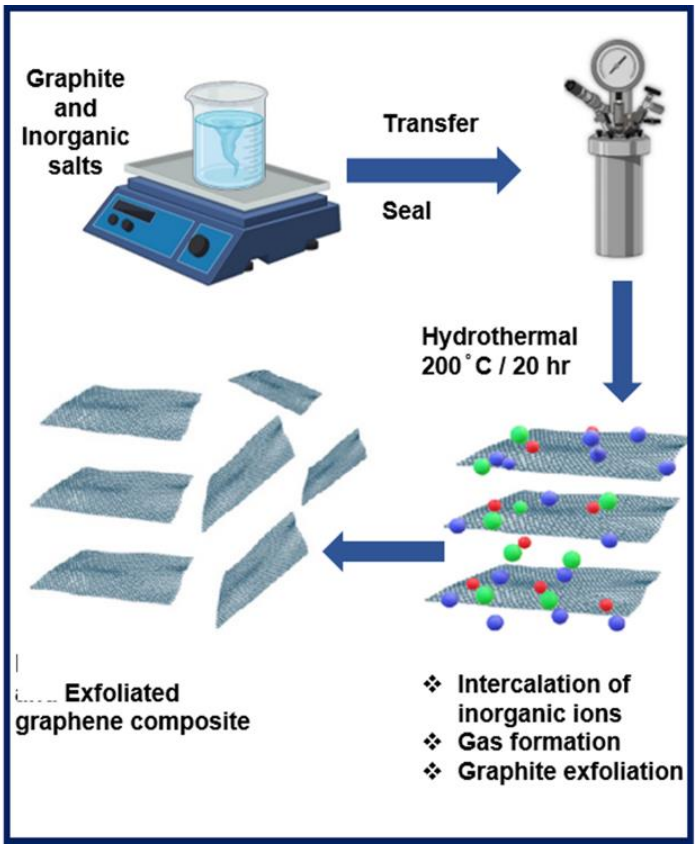

Figure 5.1 Schematic representation of the fabrication of exfoliated graphitic substances from bulk graphite powders using the hydrothermal ion intercalation technique.

The exfoliation process of natural graphite was first verified through X-ray diffraction (XRD) and Raman spectroscopic analysis, as illustrated in **Figures 5.2 and 5.3**, respectively. By using these analytical techniques, we confirm that the exfoliation process effectively separates and expands the layers of graphite, resulting in multilayer graphene sheets.

The peak shapes and intensities in their respective XRD patterns can be used to differentiate graphite, graphene, and expanded graphite. Typically, graphite displays a sharp and intense peak at 2θ = 26°, whereas graphene exhibits a broader less intense peak at around 2θ = 26°. In the case of expanded

graphite, a low-intensity peak can be observed at ~26° (Johra et al. 2014; Huang et al. 2015; Valapa et al. 2015; Chen et al. 2021).

Figure 5.2 illustrates the XRD graphs of both natural graphite and the EG composite. The diffraction peaks located at 2-Theta 26.4º, 44.8º and 54.2º correspond to respective (002), (101), and (004) planes of graphite, (JCPDS 01-0640). The sharp basal diffraction peak at 2θ = 26.4° (002) appeared for both natural graphite and EG composite, confirming the presence of graphitic structure. The position of the basal peak remains the same as that reported for natural graphite in literature (Chen et al. 2004; Yasmin et al. 2006; Li et al. 2007; Bai et al. 2013; Li et al. 2013; Kanakaiah et al. 2014; Valapa et al. 2015; Sasanka Hewathilake et al. 2017). In contrast, the XRD pattern of the EG composite exhibits a noticeable decrease in intensity, indicating the formation of expanded graphite during the exfoliation process. According to previous literature, a lower peak intensity corresponds to a higher degree of exfoliation (Yasmin et al. 2006). Furthermore, a new peak appears around 28.9°, consistent with previous literature on expanded graphite (Li et al. 2007). During the XRD analysis, the presence of graphene was difficult to confirm due to its minor quantity. To confirm the presence of graphene in the exfoliated composite, additional analysis methods such as Raman spectroscopy, SEM, and TEM were employed.

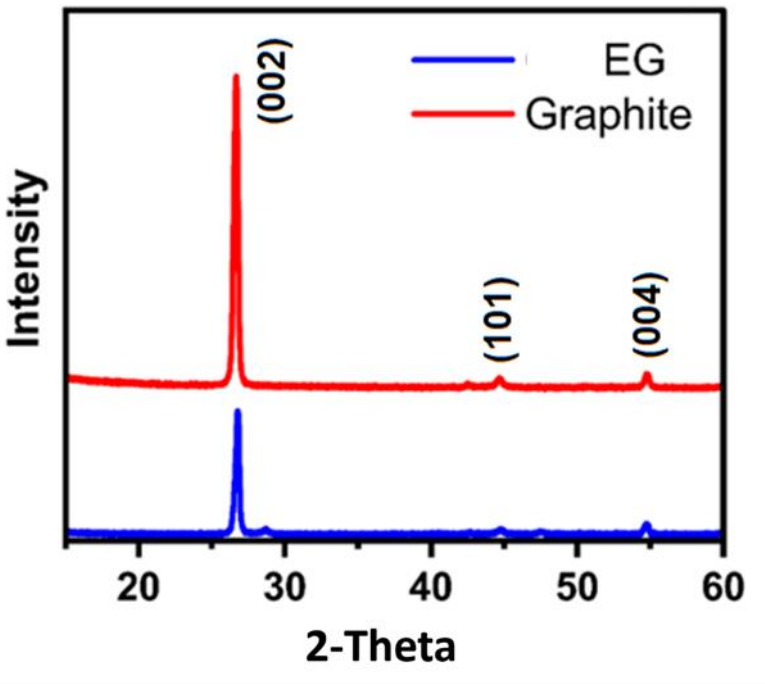

Figure 5.2 XRD of natural graphite powder and EG composite.

Raman spectroscopy has proved to be a highly valuable and widely applied analytical approach, particularly for analysing graphitic substances. By analysing the characteristic peaks in the Raman spectra, researchers can determine important properties like crystallinity, number of layers, and defect content, which provide valuable evidence of a graphitic material's quality and purity (Ferrari 2007).

Graphitic materials typically exhibit three well-known characteristic Raman peaks, the D, G, and 2D bands. These peaks are typically detected at approximately 1350, 1580, and 2700 cm^{-1}, respectively (Tuinstra and Koenig 1970; Ferrari et al. 2006; Bai et al. 2013; Qiu et al. 2019).

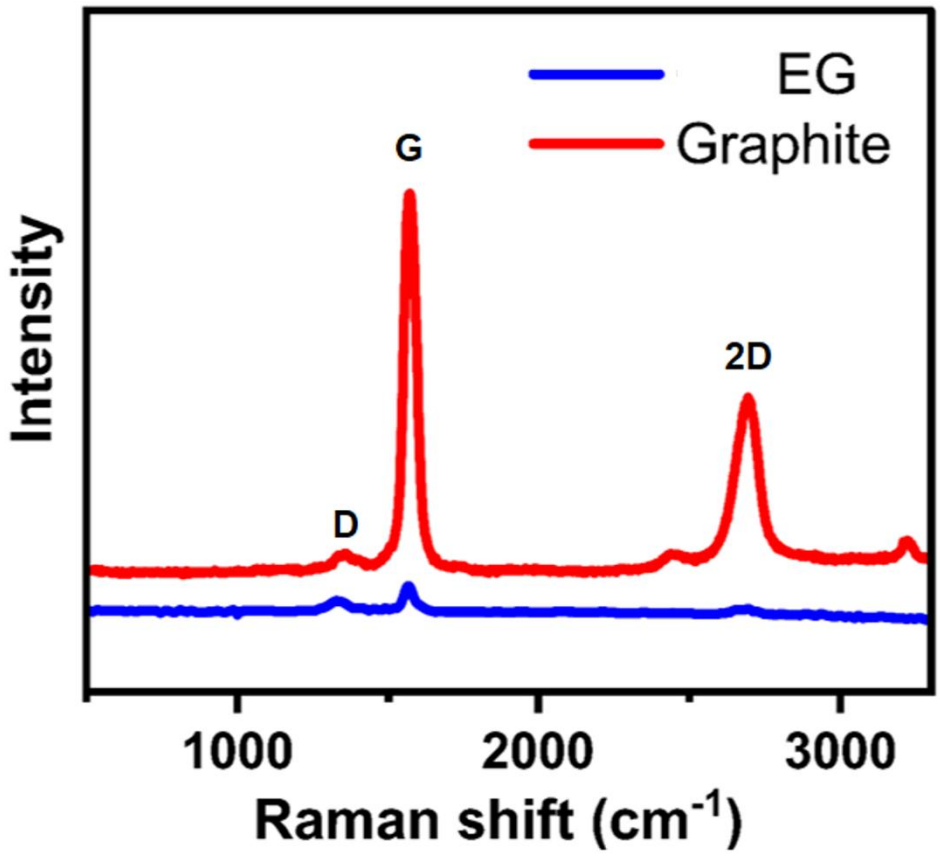

Figure 5.3 Raman spectra analysis of natural graphite and EG composite excited at 532 nm.

In graphite, the D band is caused by the presence of edges, defects, and disorders, which arise due to the activation of six-membered carbon rings in breathing modes. The G band originates from the in-plane sp^2 carbon vibrations, which are attributed to the phonon mode with E_{2g} symmetry. Similarly, the 2D band is created by two-phonon lattice vibrations (Tuinstra and Koenig 1970; Zólyomi et al. 2011; Rao et al. 2014; Hadi et al. 2018). D bands are usually weaker in graphite than G bands, signifying a defect density.

Graphitic materials are assessed based on the intensity proportion of the D to G band (I_D/I_G), a quantification of disorder and defects in graphitic structure (Tuinstra and Koenig 1970; Bai et al. 2013).

Figure 5.3 represents the Raman spectrum analysis of both natural graphite and EG composite after hydrothermal processing, demonstrating significant structural changes during the conversion. It is possible to establish the layer count present in exfoliated graphitic materials by analysing the location and the appearance of the 2D band. Specifically, a much broader 2D peak that shifts to lower wavenumbers evidences the graphite to multilayer graphene exfoliation, achieved through decreasing the number of layers (Ferrari 2007; Ferralis 2010; Ling et al. 2011; Hadi et al. 2018). In **Figure 5.3**, the changes in the 2D peak characteristics indicate the graphite to few-layer graphene exfoliation. Particularly, following the exfoliation process, a shift in the 2D peak can be detected in the natural graphite spectrum, moving from the exfoliated graphene composite, which indicates successful graphite to few-layer graphene transformation.

The I_D/I_G values obtained for natural graphite and the EG composite were 0.08 and 0.87, respectively. The significant increase in the I_D/I_G ratio in EG composite signifies that intense hydrothermal conditions have caused defects to arise within the graphitic structure. Additionally, the increased I_D/I_G ratio in the EG composite material signifies the presence of small sp^2 domains, confirming the exfoliation process as previously reported in other studies and providing further evidence of successful exfoliation through hydrothermal treatment (Ferrari and Robertson 2000; Stankovich et al. 2007). Collectively, these observations demonstrate the effectiveness of the hydrothermal

exfoliation process in producing high-quality exfoliated graphene materials from graphite.

The graphite-to-graphene hydrothermal conversion process was further confirmed using surface morphology analysis. **Figure 5.4** illustrates the scanning electron microscope (SEM) micrographs of the natural graphite powder, while **Figure 5.5** displays the SEM analysis of the EG. The microstructure and surface features of the materials provide valuable insights into the successful exfoliation of bulk graphite powder into exfoliated graphene.

As revealed in **Figure 5.4**, the starting bulk graphite was disorderly and irregular, with a particle size ranging from 10-700 µm.

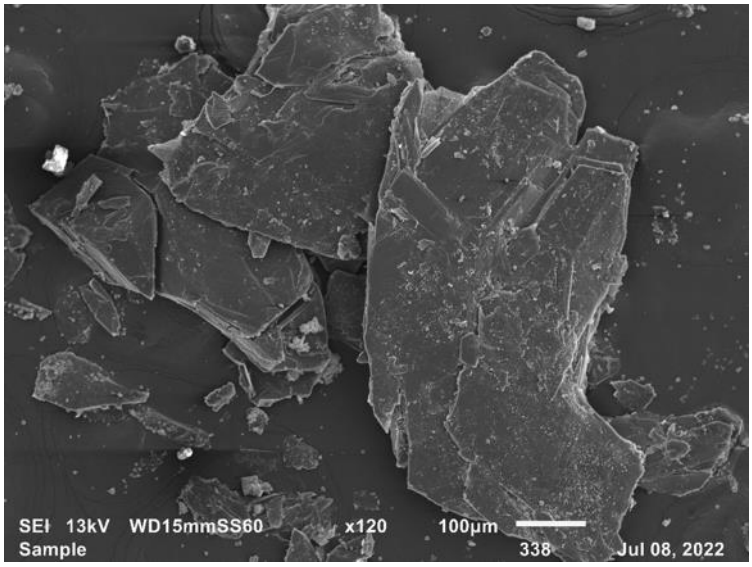

Figure 5.4 Scanning electron microscope (SEM) micrographs of the natural graphite powder.

The hydrothermal process caused significant changes in the surface morphology of graphite, resulting in multiple morphologies for exfoliated graphene structures as shown in **Figure 5.5**. The micrographs demonstrate

that the produced graphene exhibits a wrinkled and thin morphology with a transparent nature, which is consistent with previous reports (Stankovich et al. 2007; Boeva et al. 2014; Xu et al. 2015; Salverda et al. 2022). Furthermore, the SEM investigation in **Figure 5.5(c)** reveals the presence of additional wrinkling and small particles within the exfoliated graphene. These small structures were identified as broken graphite nanostructures, which result from vigorous hydrothermal conditions (See **Figures 5.6 to 5.8** SEM/EDX mapping). In addition, it has been observed that the exfoliated composite contained sheet-like folded structures in the edge plane, which are most likely to be agglomerated graphite nanoflakes, graphene, and granules (**Figure 5.5(d)**). The harsh hydrothermal conditions have caused the graphene and graphitic nanostructures to crumble and fold, resulting in this unique morphology and a similar phenomenon has been reported in previous studies such as (Zhou et al. 2014; Vadivel et al. 2020). This unique morphology exhibits a remarkably high surface area, making the exfoliated graphene composite a potential high-capacitive anode candidate for lithium-ion batteries.

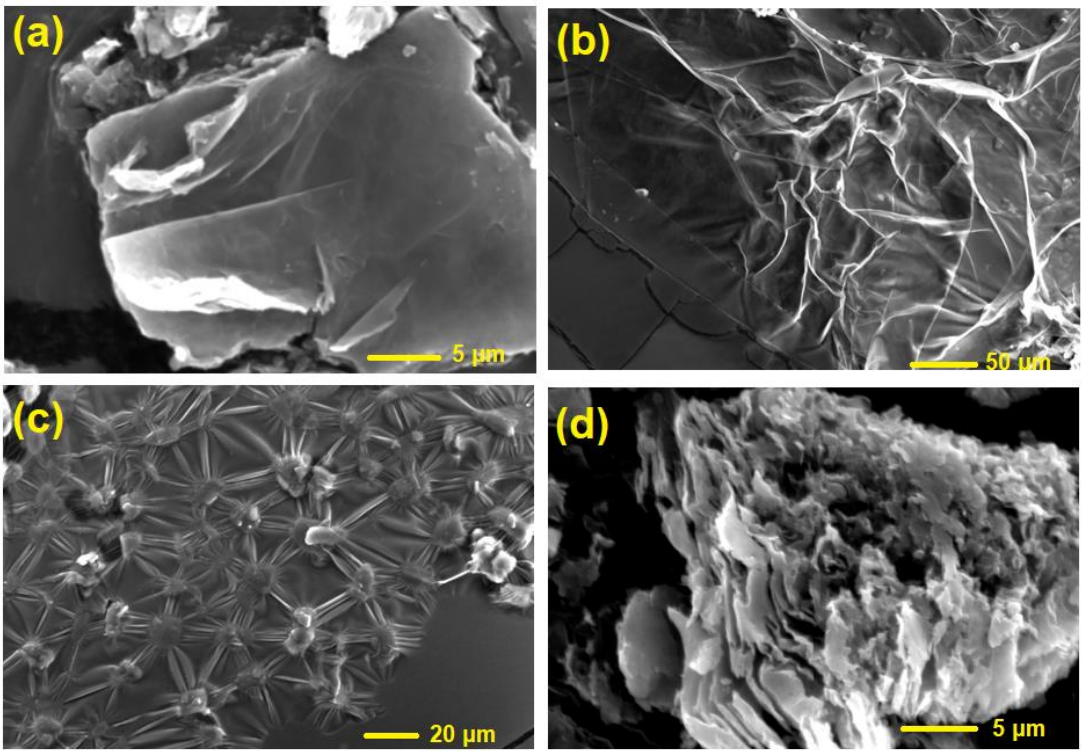

Figure 5.5 Scanning electron microscope (SEM) micrographs of the exfoliated graphene composite showing multiple morphologies.

To investigate the elemental compositions of the exfoliated graphitic materials, further analyses were conducted using scanning electron microscopy (SEM) in conjunction with the energy-dispersive X-ray analysis (EDX) technique. The SEM/EDX combination allows for comprehensive sample examination through morphology and elemental composition.

Figures 5.6 to 5.8 illustrate the three distinct morphologies of the exfoliated graphene and their corresponding SEM/EDX mapping results. It was observed that morphologies contained carbon (C), silicon (Si), and oxygen (O), with the presence of sodium (Na) impurities that were most likely introduced through sodium salts, which were used in the hydrothermal exfoliation process. The silicon was discovered to have originated within the graphite raw material itself,

likely due to the presence of SiOx. This could potentially enhance the energy density of the exfoliated graphene.

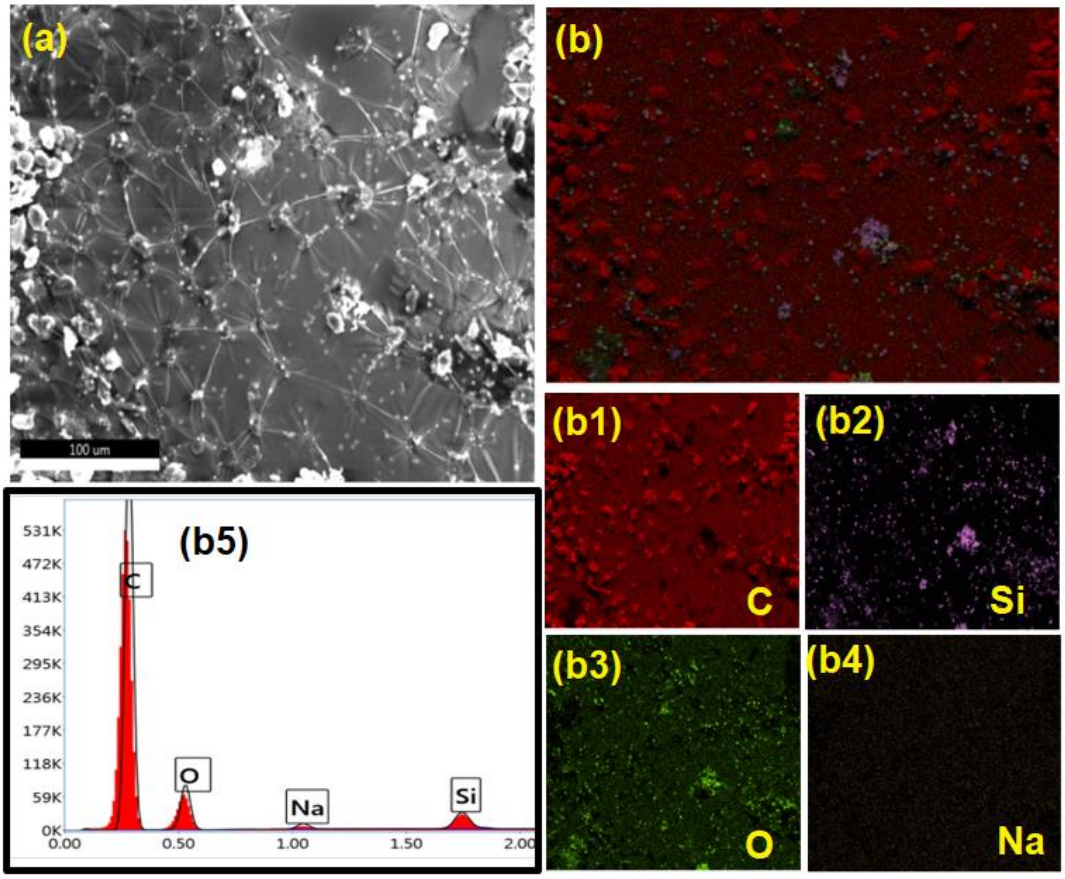

Figure 5.6 SEM/EDX mapping of exfoliated graphene (Morphology 1) (a) SEM micrograph; (b) mapping and elemental investigation, including (b1) C, (b2) Si, (b3) O, (b4) Na and (b5) elemental analysis.

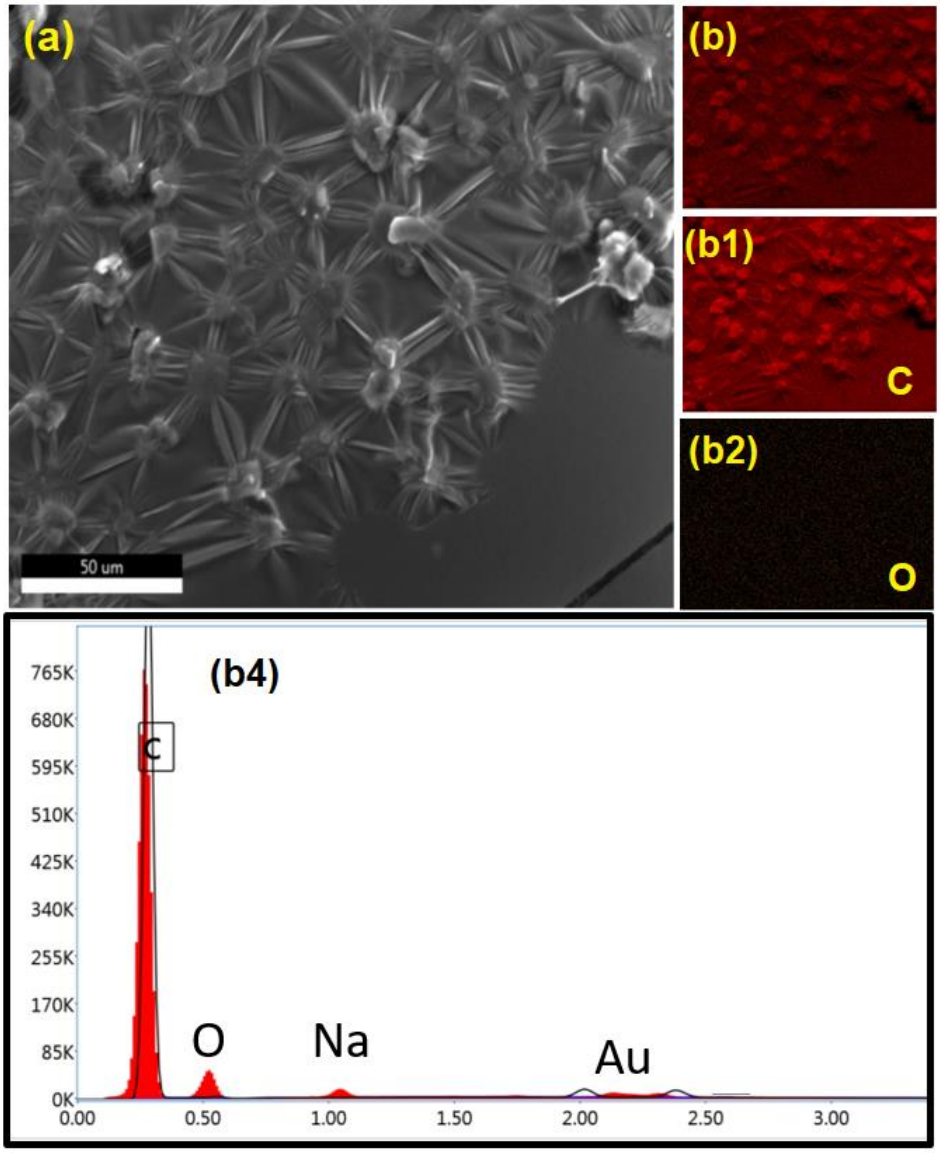

Figure 5.7 SEM/EDX mapping of exfoliated graphene (Morphology 2) (a) SEM micrograph; (b) mapping and elemental investigation, including (b1) C, (b2) O and (b4) elemental analysis.

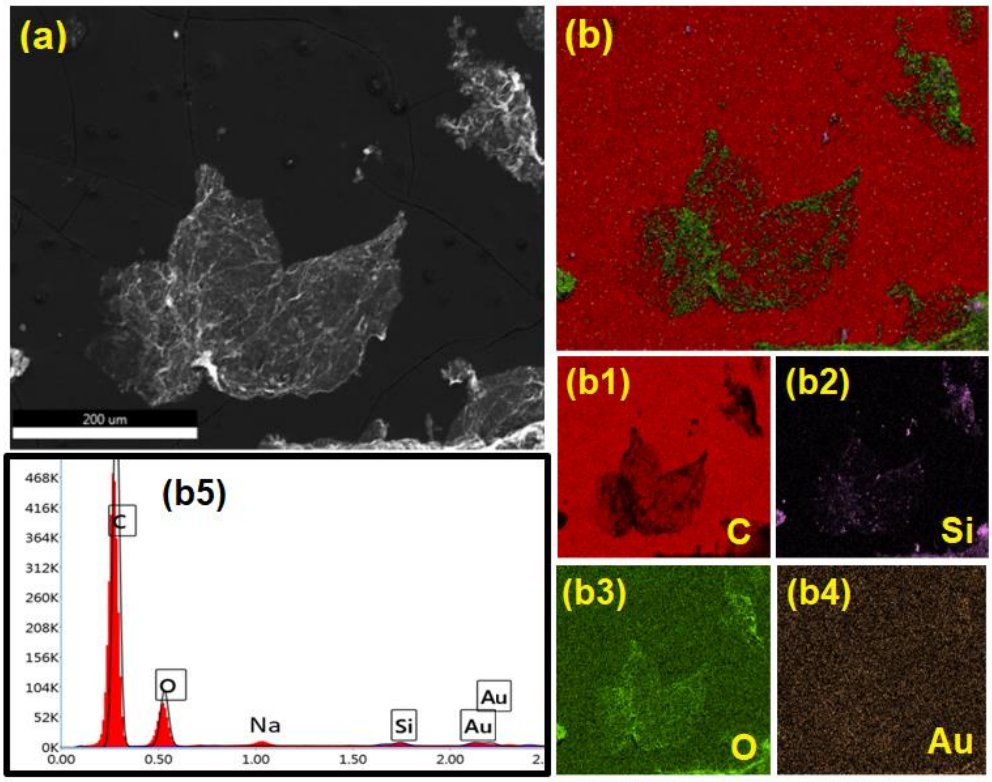

Figure 5.8 SEM/EDX mapping of exfoliated graphene (Morphology 3) (a) SEM micrograph; (b) mapping and elemental investigation, including (b1) C, (b2) Si, (b3) O, and (b4) Au and (b5) elemental investigation.

Further morphological evaluation of the exfoliated graphene was conducted using TEM analysis and demonstrates the presence of transparent multilayer graphene nanosheets (**Figure 5.9**). It is worth noting that resulted in graphene sheets appear to be relatively smooth, unlike reduced graphene oxide with numerous wrinkles (Yang et al. 2012; Qiao et al. 2015). The smooth surface of the graphene sheets observed in the present study can be attributed to the hydrothermal exfoliation technique, which does not involve any harsh chemical reactions. Furthermore, it is worth noting that the edges of graphene sheets

tend to scroll and fold, due to the intrinsic property of graphene. In addition, some dark opaque regions were observed, which indicates the presence of thick exfoliated sheets. All these results collectively confirm the successful graphite-to-graphene exfoliation.

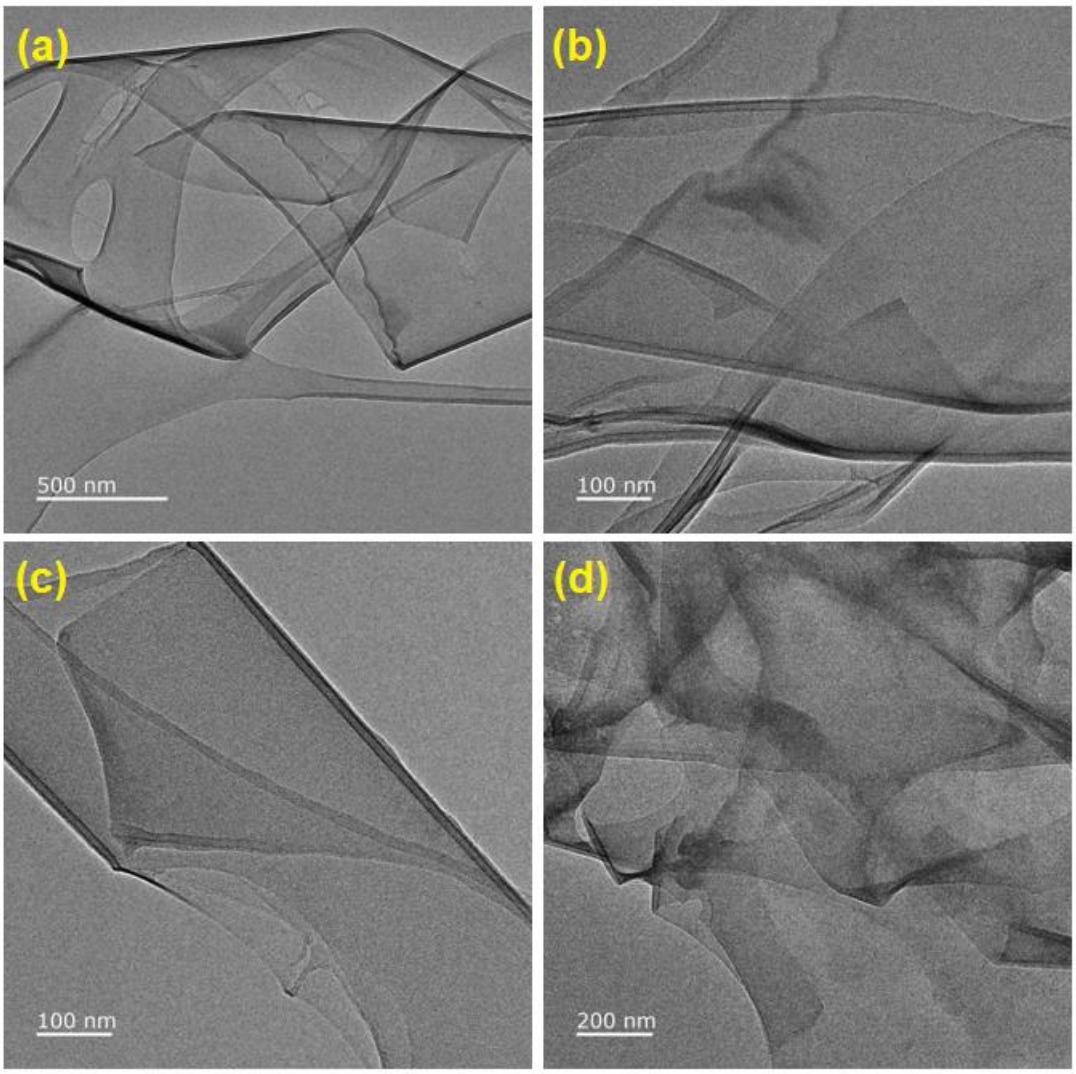

Figure 5.9 Transmission electron microscope (TEM) images of the exfoliated graphene.

In summary, the collective results obtained from all material characterisation techniques provide strong evidence of the successful graphite-to-graphene exfoliation process. In addition, SEM/TEM images of the exfoliated graphene revealed the material's unique morphology with enhanced surface area, suggesting its potential to enhance battery performance when exfoliated.

5.3.2 Electrochemical characterisation

5.3.2.1 Electrochemical characterisation of natural graphite and exfoliated graphene composite

This section evaluates the Li-ion battery performance of natural graphite (NG) and EG composite as baseline materials. The cyclic voltammetry (CV) analysis was conducted applying a slow-scanning power of 0.1 mV s^{-1} within a potential spectrum of 0.01-1.5 V (vs Li^{+}/Li) (**Figure 5.10 (a), and (b)**).

The lithiation cut-off potential of 0.01 V was used to increase the Li-ion intercalation into the graphite matrix while avoiding Li deposition on graphite. During the first lithiation curve **(Figure 5.10 (a), and (b))**, NG displays a slightly broad prominent peak at ~ 0.7 V accompanying the reductive decomposition of electrolyte and subsequent solid electrolyte interface (SEI) development (Bai et al. 2013). In comparison with NG, hydrothermally exfoliated graphene composite shows a relatively blunt peak for SEI layer formation. This observation could be attributed to the possible presence of impurities like silica in the natural graphite sample (Bai et al. 2013).

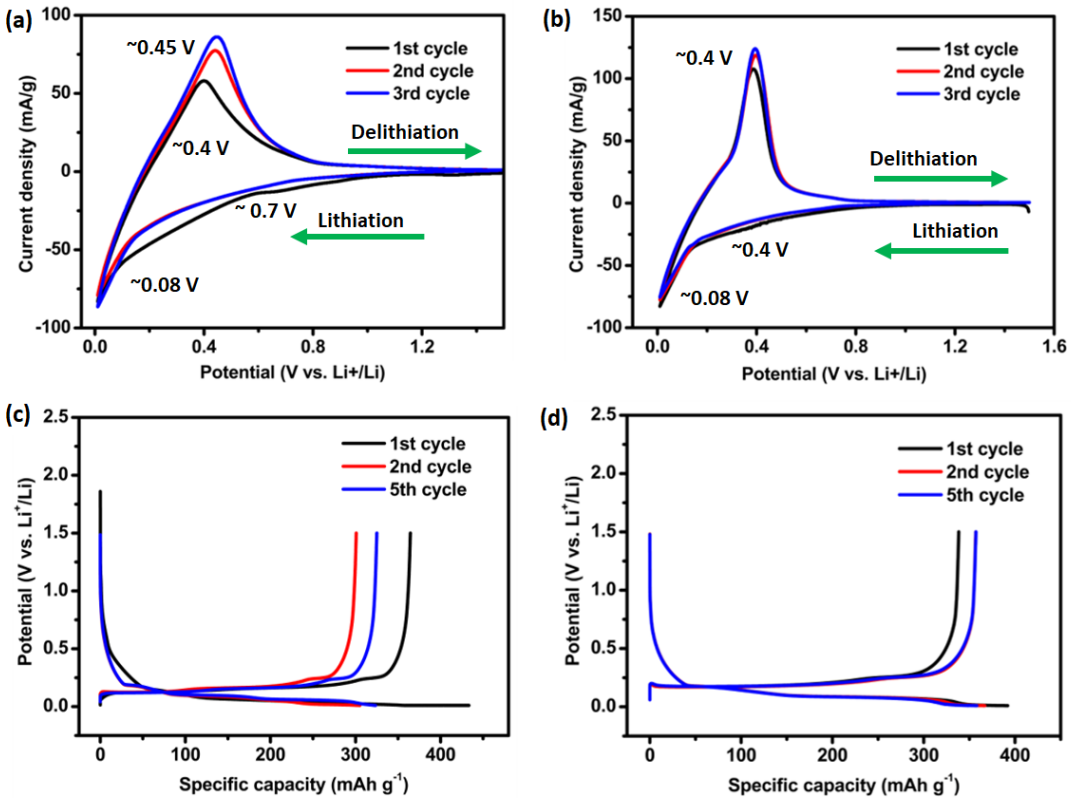

Figure 5.10 Cyclic voltammetry analysis of (a) NG (b) EG at a scanning power of 0.1 mV s^{-1} in the voltage spectrum of 0.01– 1.5 V. The galvanostatic discharge/charge profiles of (c) NG (d) EG in the 1st, 2nd, and 5th cycles in the potential spectrum of 0.01–1.5 V at 0.1 C.

The SEI formation peaks observed for both NG and EG composite at ~ 0.7 V faded in the following cycles suggesting that the electrolyte decomposition had ceased resulting in a stable SEI film (Wu and Bennett 2012). Meanwhile, the prominent reduction peak was observed at ~ 0.08 V for both NG and EG composite during their first lithiation cycle. This peak signifies the lithium-ions intercalation into the graphitic layers as LiC_6 (Zhong et al. 2020b). Furthermore, NG and EG composite shared their first anodic delithiation peak at around ~ 0.4 V equivalent to the extraction of Li-ions from LiC_x complex (Bai et al. 2013). Noticeably, the de-intercalation peak for the NG anode is broader than that of

the EG composite, implying slow electrochemical kinetics of NG (Wu and Bennett 2012). Additionally, during successive cycles, the anodic peak for NG tends to move towards a more positive potential, whereas the delithiation voltage for EG composites remains fixed. Interestingly, the EG composite exhibited a higher delithiation current flow compared to NG, indicating an improved capacitive performance (Lee et al. 2021).

Figure 5.10 (c), and (d) illustrate the first, second and fifth galvanostatic charge-discharge specific capacity curves for the NG and EG electrodes at a current flow of 0.1 C. Comparable to the CV observation, in the first galvanostatic discharge curve of NG (**Figure 5.10 (c)**) displays a potential plateau from 1.0 – 0.5 V representing the SEI layer formation. However, EG experienced relatively low irreversible capacity loss at first discharge, possibly owing to improved electrical conductivity and the removal of impurities through the exfoliation process. (**Figure 5.10 (d)**). In both scenarios, the discharge capacity curves show a smooth voltage drop from 0.5 to ~ 0.2 V due to the first Li-ion insertion into the graphite matrix or multilayer graphene sheets of EG composite, which is in line with previous graphite reports (Zhong et al. 2020b).

The intercalation process in graphite electrodes typically follows a stage mechanism with a well-known reversible lithium-graphite intercalation. According to Zhang et al., graphite anode stores the Li-ions through five continuous phases of lithiation steps at a potential less than 0.2 V vs. Li/Li^+(Zhang et al. 2001). During the intercalation, Li-ions are introduced into the graphitic layers starting with LiC_{72} and progressing through LiC_{36}, LiC_{27}, LiC_{18}, and LiC_{12}, until the maximum intercalation stage of LiC_6 is reached. The stepwise intercalation stores the Li-ions within the graphite structure, enabling

the reversible cycling of the graphite anode in Li-ion batteries. Under ambient conditions, each six-carbon hexagon can store a maximum of one Li-ion resulting in a graphite's specific nominal gravimetric capacity of 372 mAh g^{-1}. Li-ion insertion generally occurs only in the graphite prismatic plane, but defects may allow for additional intercalation in the basal plane.

The gravimetric Li-ion storage capacity here was estimated based on both Si and graphitic active materials mass percentages (see **Table 5.1**). For NG, the initial galvanostatic discharge/charge intercalation capacities were 433/365 mAh g^{-1}, respectively. Correspondingly, EG delivered a significantly lower first Li-ion discharge capability of 392 mAh g^{-1} and a specific charge storage of 338 mAh g^{-1}. Notably, the first discharge/charge capacities of NG in Li-ion storage considerably exceed the nominal capacity of graphite, potentially attributable to the adsorption of Li^+- ion on the graphitic edges and surface, as well as the potential presence of silica and other impurities (Bai et al. 2013). The NG and EG exhibit an ICE of 84.2 % and 86.2 %, respectively and the higher ICE of EG validates the removal of silica impurities during the hydrothermal process and improved electrical conductivity. Furthermore, both NG and EG composite ICEs are comparable to or improved than those reported by natural graphite and synthetic graphite data (Bai et al. 2013; Zhong et al. 2020b).

Despite the first discharge cycle, the capacity of the following cycles for both NG and EG was lower than that of the first cycle, which was identified due to the inclusion of some undecomposed Li_2O phase, and unalterable capacity loss from SEI formation.

Moreover, from the first to the second cycle, an obvious capacity loss was observed for NG as discharge/charge capacities of 305/301 mAh g^{-1},

respectively resulting in a Coulombic efficiency (CE) of 98.6 %. However, EG possesses respective discharge/charge Li-ion storage of 367/357 mAh g^{-1}, with a CE of 97.3 %. A remarkable 93.6 % of the first discharge capacity was retrieved by the EG, while the NG recovered only 70.5 %. Furthermore, during the 5th cycle, NG reached a discharge/charge Li-ion storage of 324/325 mAh g^{-1} while EG delivered 358/357 mAh g^{-1}, respectively. Both NG and EG possess excellent respective CEs at 97.6 % and 99.7 %. Regarding the charge capacities, EG presented an enhanced Li-ion storage trend from the 1st to 5th cycle, while NG's capacity faded over the first five cycles.

Pan et al, suggested that the disordered graphene could significantly enhance the reversible capacity than that of graphite by providing added Li-ion storage sites such as defects and edges (Pan et al. 2009). Additionally, expanded graphite increases the number of active sites and facilitates Li-ion penetration, attributed to their porous nature and excellent surface area (Bai et al. 2013).

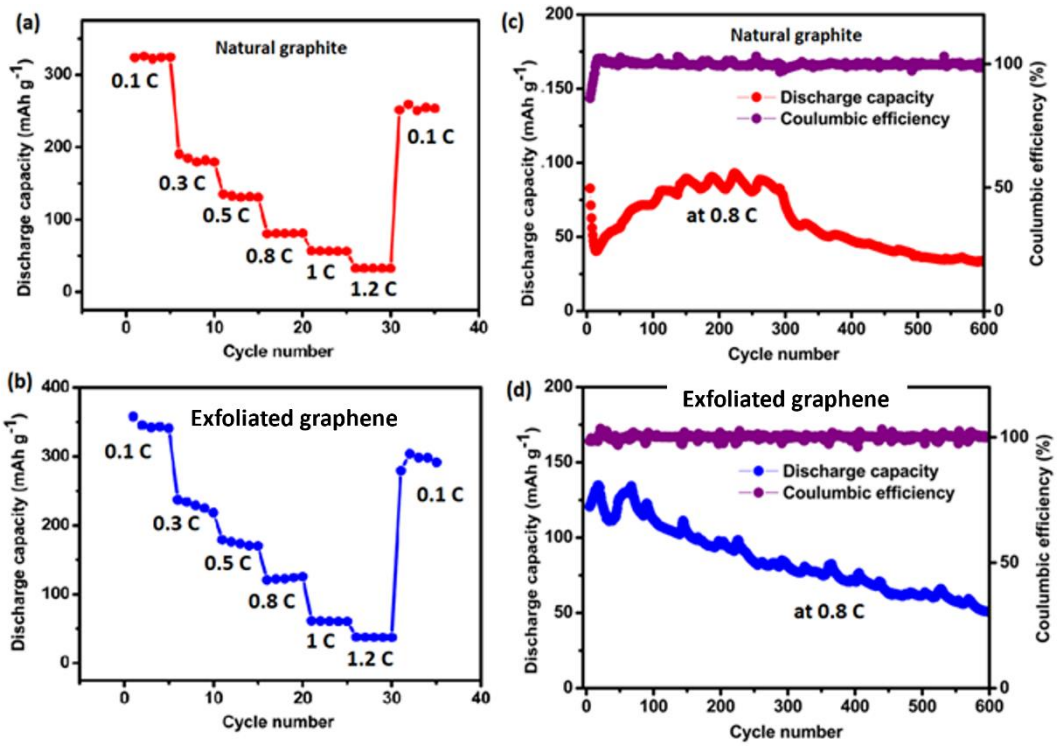

Figure 5.11 Lithium-ion battery performance of NG and EG composite: Rate performances of a) NG b) EG at different C-rates in the potential spectrum of 0.01– 1.5 V. Cycle life investigation of c) NG d) EG at 0.8 C in the potential spectrum of 0.01– 1.5 V.

As demonstrated in **Figure 5.11**, power capabilities and lifespan characteristics of NG and EG composite were inspected. The NG displays average capacities of 323.95, 183.39, 132.35, 80.98, 56.62 and 32.91 mAh g^{-1} at different C-rates of 0.1, 0.3, 0.5, 0.8, 1, and 1.2 respectively (**Figure 5.11 (a)**). Following the rate test, when the specific current flow was applied back to the initial 0.1C power, the discharge capacity resumed to around 253.98 mAh g^{-1}, resulting in a 78.4 % capacity recovery. Similarly, EG composite demonstrated slightly higher discharge capacities than that of NG at similar C-

rates as 345.92, 228.81, 173.94, 122.97, 61.15 and 37.59 mAh g^{-1} and showed an 85 % of excellent capacity preservation with a Li-ion discharge storage of 294.3 mAh g^{-1} at 0.1C (**Figure 5.11 (b)**).

The long-term cycle life stability of both materials was evaluated starting from their respective 5^{th} cycle at 0.8C constant current charge/discharge rate from a voltage window of 0.01-1.5 V, shown in **Figures 5.11 (c) and (d).** After 600 cycles, the NG electrode provided a steady Li-ion discharge Li-ion storage capability of 33.3 mAh g^{-1}, owning to a 40.19 % capacity preservation. Notably, the capacity of NG increased progressively after around 15 cycles and fluctuated during 113 to 268 cycles, probably due to systematic penetration and insertion of Li-ions into the core of the silica and other impurities. Next, the capacity faded from 268 to 600 cycles. Conversely, EG composite recovered a slightly higher Li-ion storage capacity than that of NG at 50.6 mAh g^{-1} and a capacity retaining of 41.96 %, following the 600 charge/discharge cycles. The capacity fading for both NG and EG composite throughout cycling can be attributed to several factors. These include structural damage to the graphite crystal lattice caused by repeated lithium-ion intercalation and deintercalation processes, the growth of lithium metal microstructures known as dendrites on the graphitic surface, volume expansion of graphitic electrodes, and mechanical disintegration due to pulsating of the electrode materials attributing to the continuous charging and discharging (Dai et al. 2015; Guo et al. 2015; Zhong et al. 2020b).

Coulombic efficiencies of both NG and EG composite electrodes were explored over the cycling as presented in **Figures 5.11 (c) and (d).** Coulombic efficiency (CE) denotes the completely discharged and charged capacities

ratio. In the case of 100 % Coulombic efficiency, all the intercalated ions are effectively deintercalated from the electrode during one charge/discharge cycle. Characteristically, both synthetic and natural graphite without impurities offers quite high Coulombic efficiency, ranging from 95 to 100%, depending on the chemical composition of the electrolyte, electrode parameters and operating conditions such as cell potential, applied specific current flow and temperature (Laziz et al. 2018; Mao et al. 2018; Rodrigues et al. 2018). In this work, both NG and EG composite maintained excellent Coulombic efficiencies at 99.86 and 99.95 % respectively, over the 600 charge/discharge cycles.

To get insight into the electrochemical performances of the NG and EG electrodes, the EIS examination was conducted. The frequency series of 100 kHz to 0.01 Hz allows the comprehensive characterisation of the electrochemical behaviour of electrodes. EIS analysis is a widely applied non-destructive tool for studying the electrochemical characteristics of lithium-ion batteries and other energy devices. EIS technique determines the cell impedance over a given frequency range and the resulting information can be applied to understand the electrochemical kinetics, overall battery health, changes of battery performance over the cycling, SEI layer formation and electrochemical processes such as interfacial, charge transfer, and mass transport processes.

A series of EIS measurements were performed for both NG and GN/EN composite after the 5^{th} discharge/charge cycles at 0% of the state of charge (SOC) and the results in Nyquist plots are presented in **Figure 5.12**. Moreover, an equivalent circuit is used to determine the electrochemical impedance parameters of electrodes as shown in the inset of **Figure 5.12 (a)**.

In general, the Nyquist plot often contains a semicircle, and the radius of the semicircle represents the overall impedance of the system, while the high-frequency range incline of the plot indicates the Li-ions diffusion nature of the system. The Z' axis intercept at high frequency denotes the equivalent series resistance (R_s), which signifies the separator, electrolyte, and electrical contact resistance. Likewise, the charge transfer resistance (R_{ct}) next to the electrode/ electrolyte boundary is assigned to the radius of the semicircle within the high-frequency area of the electrochemical impedance spectrum. The constant phase element, CPE represent the capacitive characteristics of the double layer. The ion flow in the anode material determines the Warburg impedance (W) observed as the inclined line in the low-frequency area of the electrochemical impedance graph (Wang et al. 2014; Zhang et al. 2014; Lu 2015; Zhong et al. 2020b).

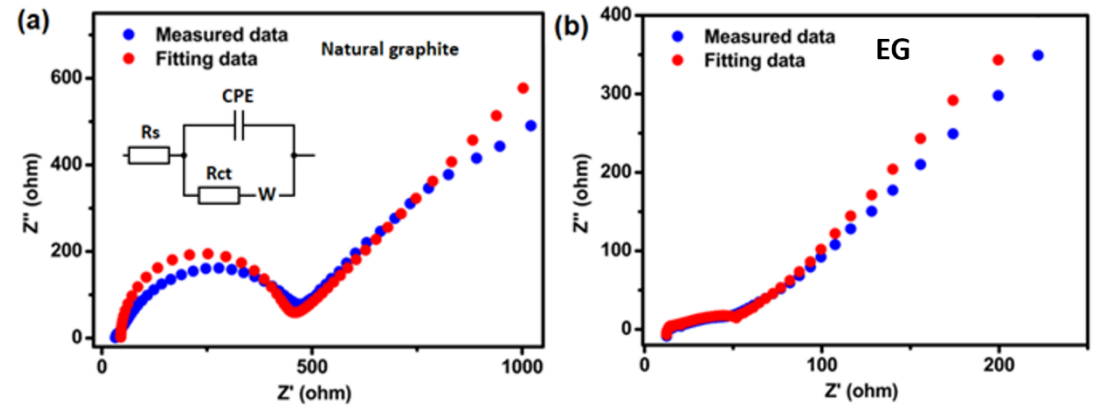

Figure 5.12 The electrochemical impedance spectra for the NG and EG anode materials after 5 cycles, at an amplitude of 5 mV in a frequency spectrum from 100 kHz to 0.01 Hz. Figure 5.12 (a) inset shows the equivalent circuit model.

Following the first discharge/charge cycles, significant impedance differences were observed between NG and EG anodes. According to the equivalent circuit simulation, NG presents substantially a higher charge transfer resistance (R_{ct}) of 381.5 Ω, while EG reveals a much lower R_{ct} of 38.12 Ω. These results confirm the improved electrical conductivity of the EG enhances the charge transfer process next to the electrode/electrolyte boundary, resulting in a lower impedance. This, in turn, indicates reduced resistance to the flow of ions and improved efficiency of charge transfer kinetics, ultimately leading to enhanced cell efficiency. As for the equivalent series resistance (R_s), the NG anode exhibited the highest at 44.82 Ω, while the EG electrode experienced the lowest R_s value of 13.2 Ω. In the EG composite, the low R_s and R_{ct} values align well with the excellent cyclability and rate capability performances. This can be ascribed to the increased electronic conductivity facilitated by the presence of exfoliated graphene.

In summary, hydrothermal conversion of natural graphite into exfoliated graphite composite results in significant improvements in Li-ion battery electrochemical characteristics such as Coulombic efficiencies, charge/ discharge capacities, cycle life, rate capability and electrochemical impedances. The improved Li-ion battery performances of EG can be ascribed to several key aspects: absence of impurities, excellent structural integrity, and electrical conductivity of graphene, defects assisted larger surface area, and high porosity of expanded graphite, which offer improved capacity, energy density and fast electrochemical discharge/charge kinetics.

5.3.2.2 Electrochemical characterisation of (Si-EG) composite

This section evaluates the Li-ion battery electrochemical performance of Si-EG composites. The Si-EG composites were prepared in three different formulations: 10Si-EG, 30Si-EG, and 50Si-EG. In each formulation, Si nanoparticles with a diameter ranging from 30 to 50 nm were blended with EG in weight percentages of 10%, 30%, and 50% respectively (See **Table 5.1**).

The effect of various Si loading on Li-ion battery electrochemical performances has been studied to examine the optimised Si loading for the Si-EG composite and attempted to understand how the Si loading affects the electrochemical performance of the Li-ion battery.

Cyclic voltammetry (CV) was used to examine the formation process of three different electrodes, specifically focusing on the electrolyte degradation and the subsequent solid electrolyte interface (SEI) formation. The SEI film is recognised as a non-conductive film that develops on the anode during the initial charging process due to electrolyte degradation. The SEI film holds a mixture of lithium salts and organic solvents and protects the electrolyte from further decomposition (Wu and Bennett 2012).

Figure 5.13 illustrates the cyclic voltammograms for the 10Si-EG, 30Si-EG, and 50Si-EG respectively, and analysis was carried out at a slow-scanning power of 0.1 mV s^{-1} within a voltage spectrum of 0.01- 1.5 V (vs Li^{+}/Li). The specific gravimetric energies are calculated based on the overall weight of the Si and EG composite.

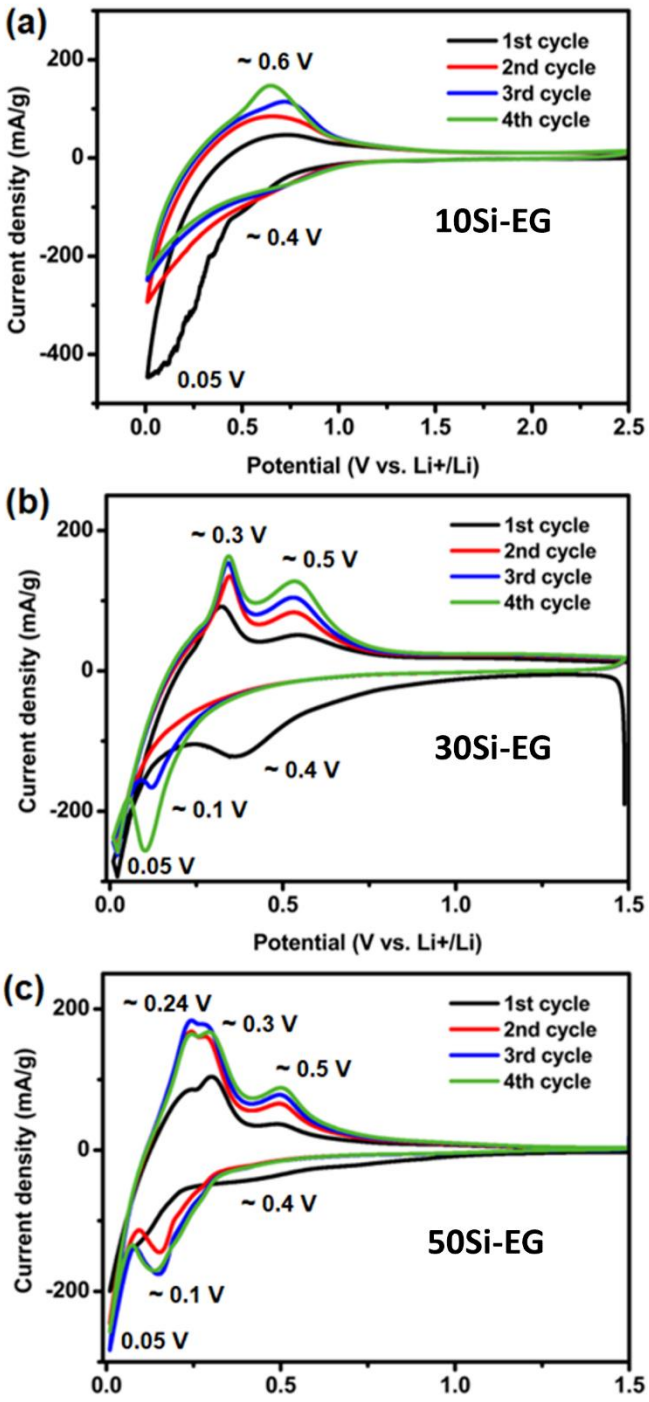

Figure 5.13 The cyclic voltammograms of Si-EG composite anodes for the first four cycles in Li//Si-EG half-cell in a voltage spectrum of 0.01–1.5 V at a low scanning power of 0.1 mV s^{-1} at 25 °C.

The difference between the CV profiles was noted for the three different composites, signifying the presence of their different Li-ion storage behaviour during their initial four cycles. The 30Si-EG and, 50Si-EG composites exhibited typical alloying/dealloying features of Si while 10Si-EG was dominated by graphitic intercalation/deintercalation nature. Prominently, the first cathodic discharge cycles of 10Si-EG, 30Si-EG, and 50Si-EG differed from their subsequent cycles mainly attributed to the solid electrolyte interphase (SEI) film development. When the potential is scanned from open circuit voltage to 0.01 V, an irreversible reductive peak centred at ~ 0.4 V vs. Li/Li^+ was noticed in all three electrodes. It is ascribed to irreversible electrolyte reduction and SEI development on the anode surface. However, the SEI peak has disappeared through subsequent cycles (Oh et al. 2017; Zhang et al. 2017a).

The first permanent capacity loss plateau of 10Si-EG (**Figure 5.13 (a)**) is significantly higher and distinct from those of 30Si-EG and, 50Si-EG composites and resembles more of the graphitic characteristics (Vu et al. 2019). This obvious phenomenon could be attributed to the comparatively low amount of Si (only 10%) in the 10Si-EG composite, which results in the domination of graphitic structure. In contrast, both 30Si-EG and, 50Si-EG composites exhibited a distinctive SEI formation plateau centred at approximately 0.4 V vs. Li/Li^+. The SEI film appears to have formed completely during the first cycle since successive cycles explained no cathodic current at 0.4 V (Mukanova et al. 2018).

In addition to the SEI formation peak, all three composite electrodes showed a reversible lithium insertion cathodic peak approximately at 0.05 V in contrast to Li/Li^+. For the 10Si-EG anode, the key intercalation mechanism could be

dominated by Li_xC_6 formation while 30Si-EG and 50Si-EG composites may benefit from both graphitic intercalation and reversible Si lithiation as Li_xSi_y alloy (Hu et al. 2014; Mukanova et al. 2018). In addition, another distinguishable reversible Li_xSi_y alloy formation peak is seen in 50Si-EG composites during their first cathodic Li-ion insertion cycle (approximately around 0.1 V in contrast to Li/Li^+), whereas the same peak appears in 30Si-EG starting from their second cycle. Because of the higher Si content, the 50Si-EG composite tends to show more Si-dominant behaviour. However, both 30Si-EG and 50Si-EG composites (See **Figures 5.13 (b) and (c)**) exhibit this peak very prominently during their consecutive cycles due to the coexistence of Li_xSi_y multiple phases during lithiation, which is consistent with the literature data for Si-based anodes (Hu et al. 2014; Ding et al. 2017; Mukanova et al. 2018)

As the potential is scanned back from 0.01 to 1.5 V, lithium ions are extracted from all three electrodes, resulting in anodic currents. The Li-ion deintercalation nature of 10S-EG is significantly different from the other two composites, due to graphene dominant charge/discharge behaviour and a broad single anodic deintercalation hump noticed at around 0.7 V in contrast to Li/Li^+. From the second to fourth cycle, however, this peak becomes prominent, and shifts left, reaching around 0.6 V in the fourth cycle. This phenomenon could be resulting due to the gradual contribution of Si over repeated lithiation/delithiation reactions. On the contrary, during the first galvanostatic discharge/charge cycle, the anodic specific current flow is significantly lower than the corresponding cathodic specific current flow. This

proposes that a relatively smaller number of lithium-ions are being delithiated from the anode, resulting in a substantial irreversible Li-ion storage loss.

The anodic CV curves for the 30Si-EG and 50Si-EG composite show the characteristic redox dealloying nature of Si-based anodes with Li-ion extraction potentials approximately at 0.3 and 0.5 V (Hu et al. 2014; Sun et al. 2016b; Ding et al. 2017). Moreover, an anodic peak around 0.24 V in 50Si-EG composite features the crystalline to amorphous structural changes of Si nanoparticles, and the intensity growth of the anodic peak reveals that the Si nanoparticles are gradually becoming more amorphous over the cycling (Ding et al. 2017).

Remarkably, the 50Si-EG composite demonstrated the highest anodic specific current flow throughout all four cycles, while the 30Si-EG came in second and, 10SEG had the lowest. The reason behind the Li-ion storage variation is the extraordinary nominal Li-ion storage of silicon (Si), which is approximately 4,212 mAh g^{-1}, according to the $Li_{22}Si_5$ alloying. This capacity is around 10 times higher than that of graphite (LiC_6), which has a nominal Li-ion storage of 372 mAh g^{-1} (Zhang et al. 2012).

In **Figure 5.14**, 0.1 C rate profiles are shown for the first, second, and fifth discharge/charge cycles of 10Si-EG, 30Si-EG, and 50Si-EG, respectively.

As summarised in **Table 5.2**, the 10Si-EG, 30Si-EG, and 50Si-EG composites demonstrated respective initial discharge/charge capacities of 570.35/433.21,1488.16/1035.00, and 2198.54/1380.16. These capacities corresponded to initial Coulombic efficiencies of 75.9, 69.5, and 62.8 %.

Table 5.2 Galvanostatic charge/discharge performance comparison for first five cycles of 10Si-EG, 30Si-EG, and, 50Si-EG composites.

Composite	1st discharge/charge capacities/ (mAh g^{-1})	ICE/ (%)	5th discharge/charge capacities/ (mAh g^{-1})	5th cycle CE/ (%)
10Si-EG	570.35/433.21	75.9	519.0/506.6	97.6
30Si-EG	1488.16/1035.00	69.5	962.5/926.9	96.3
50Si-EG	2198.54/1380.16	62.8	1220.5/1167.3	95.6

Notably, the highest initial discharge (lithiation)/ charge (delithiation) capacities were obtained for the 50Si-EG, due to its high silicon content. In addition, SEI is formed when the electrolyte is decomposed in the initial cycle, thereby resulting in irreversible Li-ion storage loss (Nadimpalli et al. 2012). Thus, 50Si-EG anode demonstrates the lowest ICE of 62.8%, while 10Si-EG displays the highest ICE of 75.9 %. In contrast, the 30Si-EG composite shows an ICE of 69.5 %. As anticipated, the higher the Si content, the lower the ICE, since Si consumes more electrolyte during discharge/charge to create a steady SEI layer at the anode (Hu et al. 2014). On the other hand, all the composites maintained excellent Coulombic efficiency in the 5th cycle from 96 to 98 %, indicating the excellent reversibility between the lithiation/delithiation process during follow-up cycles.

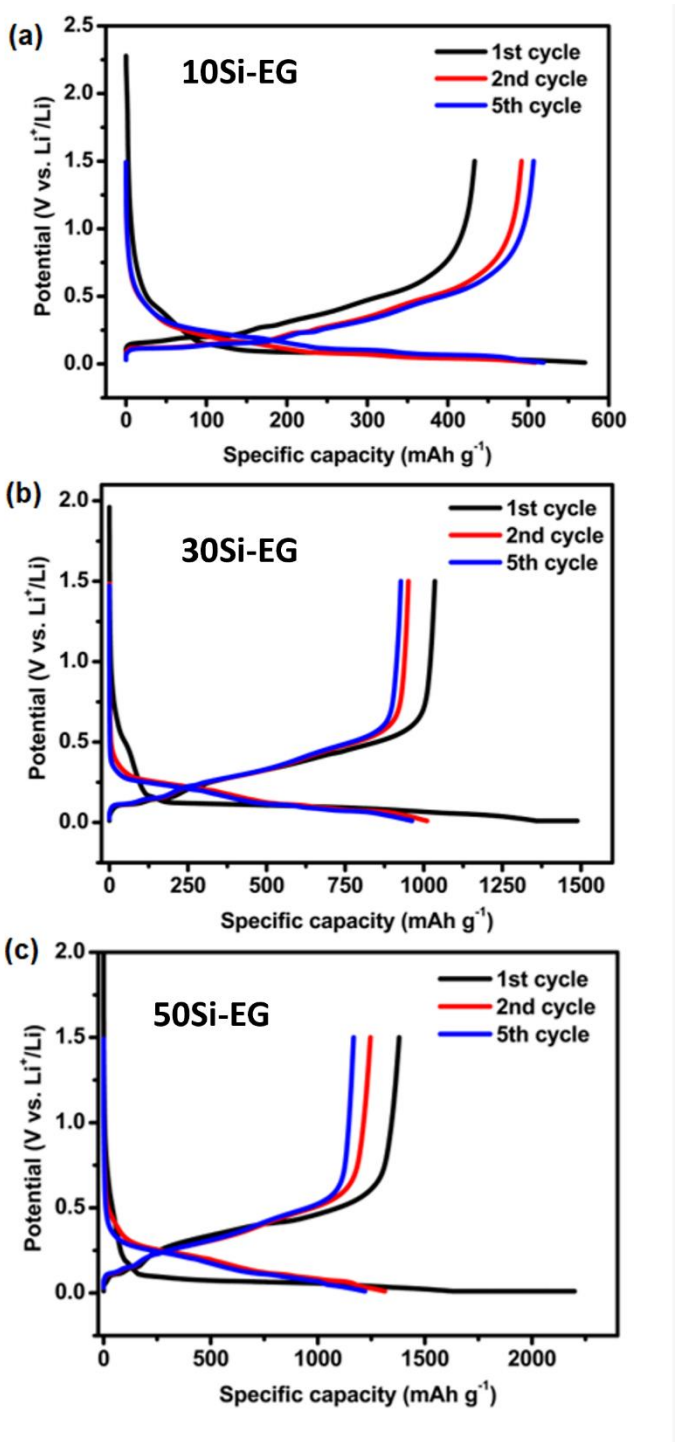

Figure 5.14 The galvanostatic discharge/charge profiles of Si-EG composite anodes for the first five cycles in Li//Si-EG coin half-cell in a potential spectrum of 0.01–1.5 V at a specific current flow of 0.1 C at 25 °C.

Figure 5.15 depicts the rate performances of 10Si-EG, 30Si-EG, and 50Si-EG composites. All three composites exhibit favourable rate performance, with 30Si-EG highlighting the highest rate capability, achieving an average discharge Li-ion storage of 309.2 mAh g^{-1} at a power of 1.2 C. 50Si-EG shows the Li-ion storage of 193.6 mAh g^{-1} while 10Si-EG experience the lowest of 118.4 mAh g^{-1} at 1.2C. At 1.2C, the 50Si-EG composite demonstrates a Li-ion storage of 193.6 mAh g^{-1}, while the 10Si-EG composite exhibits the lowest Li-ion storage of 118.4 mAh g^{-1}. Furthermore, in terms of Li-ion storage recovery after the rate test, the 10Si-EG composite displayed the highest recovery at 94.71%, with an average Li-ion storage of 488.75 mAh g^{-1} at 0.1 C. Likewise; the 30Si-EG composite exhibited a recovery of 81.31% from its initial average Li-ion storage of 1055.1 mAh g^{-1}. On the other hand, the 50Si-EG composite showed the lowest recovery rate of 76.21%, starting from an initial average Li-ion storage of 1190.97 mAh g^{-1} at 0.1 C. The lowest capacity recovery, coupled with the highest silicon content, could be attributed to increased electrode stress, consequently leading to electrode failure and a subsequent reduction in capacity.

Overall, based on the rate performance results, it was confirmed that 30Si-EG as optimised Si composite.

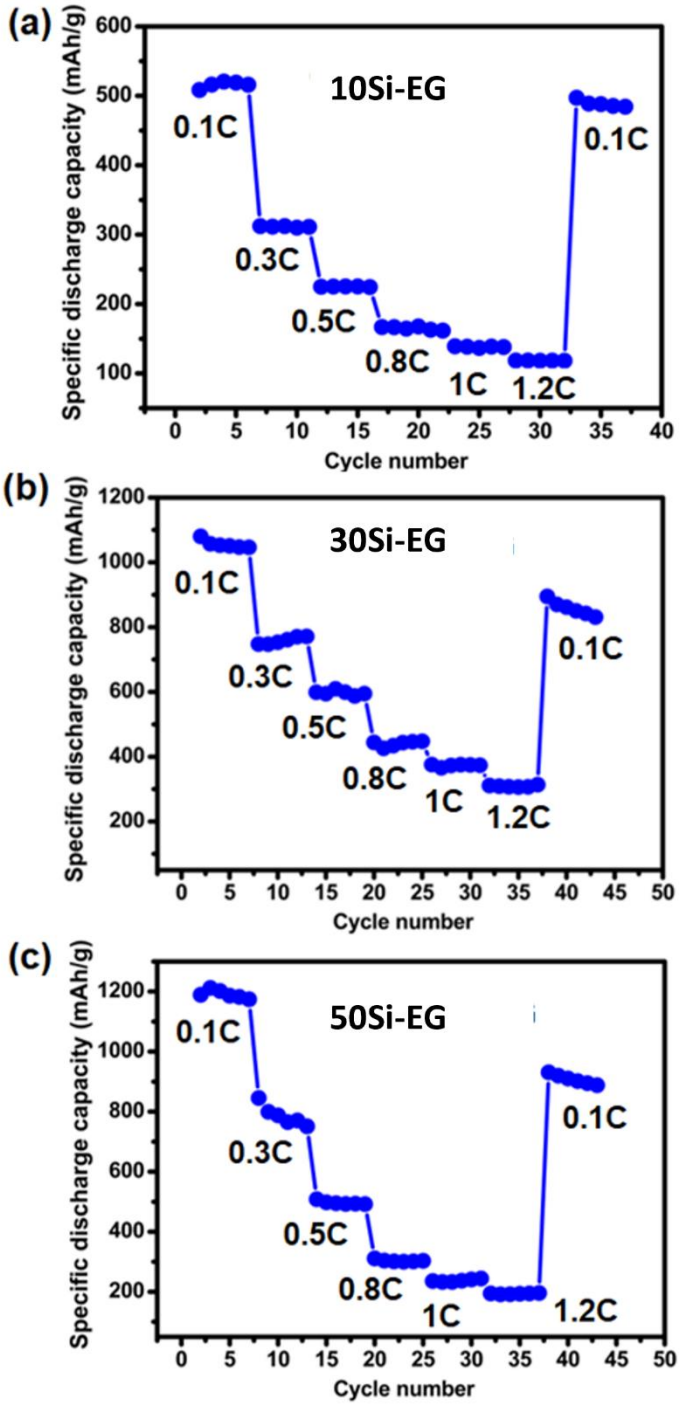

Figure 5.15 Rate performance of Si-EG composite anodes in Li//Si-EG coin half-cell in a potential range of 0.01–1.5 V at various current densities at 25 °C (1C=350 mAh g^{-1}).

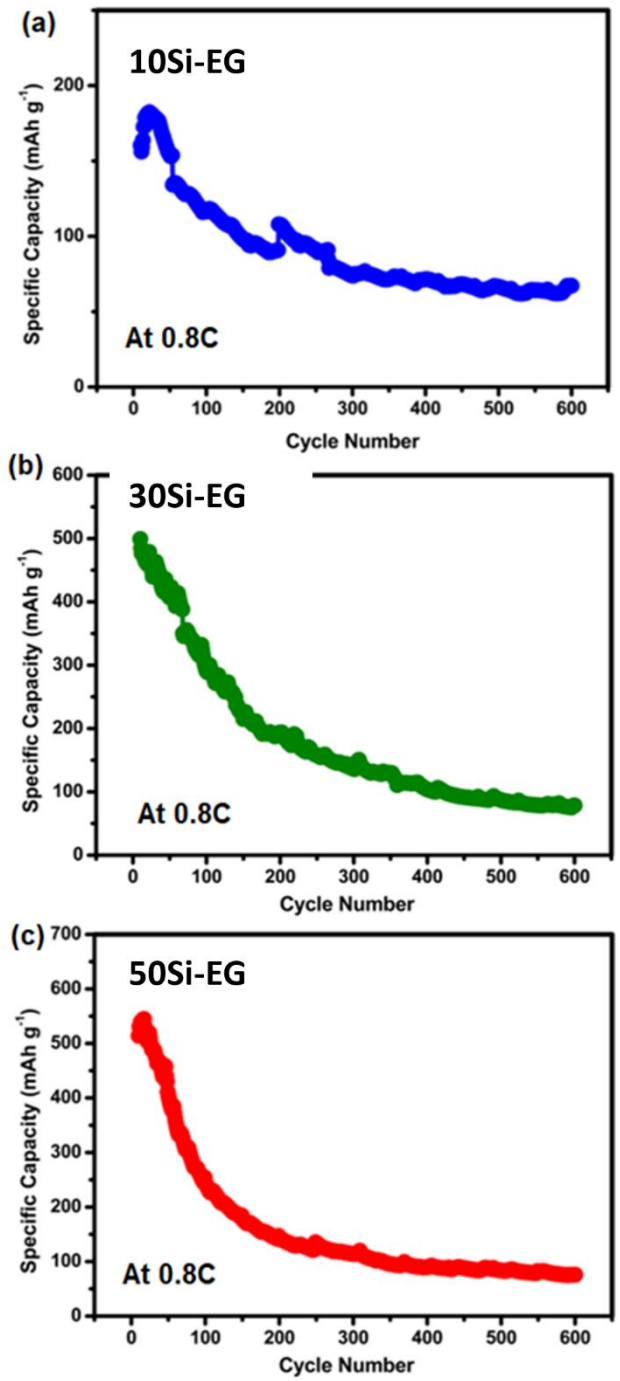

Figure 5.16 Cycle performance of Si-EG composite anodes in Li//Si-EG coin half-cell in the 0.01–1.5 V voltage window at 0.8 C and 25 °C.

The Li-ion battery cycling performance of Si-EG composites was tested starting from their 10^{th} cycle at a 0.8 C rate, as shown in **Figure 5.16**. Compared with 10Si-EG, both 30Si-EG and 50Si-EG, 10Si-EG exhibits rapid capacity decay over cycling, since they contain a higher amount of Si. The 10Si-EG, 30Si-EG, and 50Si-EG composites exhibit different discharge capacities in their 10^{th} cycle, as 160.4, 499.2, and 514.2 mAh g^{-1}, respectively. Following 600 cycles, 10Si-EG, 30Si-EG, and 50Si-EG exhibited Li-ion storage retention of 42 %, 16 %, and 10 %, respectively. It is worth noting that the cycling performance significantly worsened with the increase in Si content.

Further evaluation and comparison of the electrical conductivity of the three Si-EG electrodes were carried out via electrochemical impedance spectroscopy. **Figure 5.17** and **Figure 5.18** show the resulting Nyquist plots of the 10Si-EG, 30Si-EG, and 50Si-EG composites after 5 and 100 cycles, respectively. The equivalent circuits (inset **Figure 5.17 (a)** and **Figure 5.18 (d))** were applied to estimate the EIS parameters, as listed in **Table 5.3**.

The intercept on the Z' axis at high frequency represents the equivalent series resistance (R_s) in EIS. This value reflects the collective resistance of the electrolyte, separator, and electrical contact. Likewise, volume change resistance between the anode and SEI film is denoted by R_1, while R_{ct} signifies the charge transfer impedance at the electrode and electrolyte boundary (Lu 2015). Constant phase elements (CPE or CPE_1 and CPE_2) represent the capacitive characteristics of the SEI films and the double layers. In the low-frequency region, the inclined line in the impedance plot symbolises the Warburg impedance (W). This is determined by the diffusion of ions within the anode material.

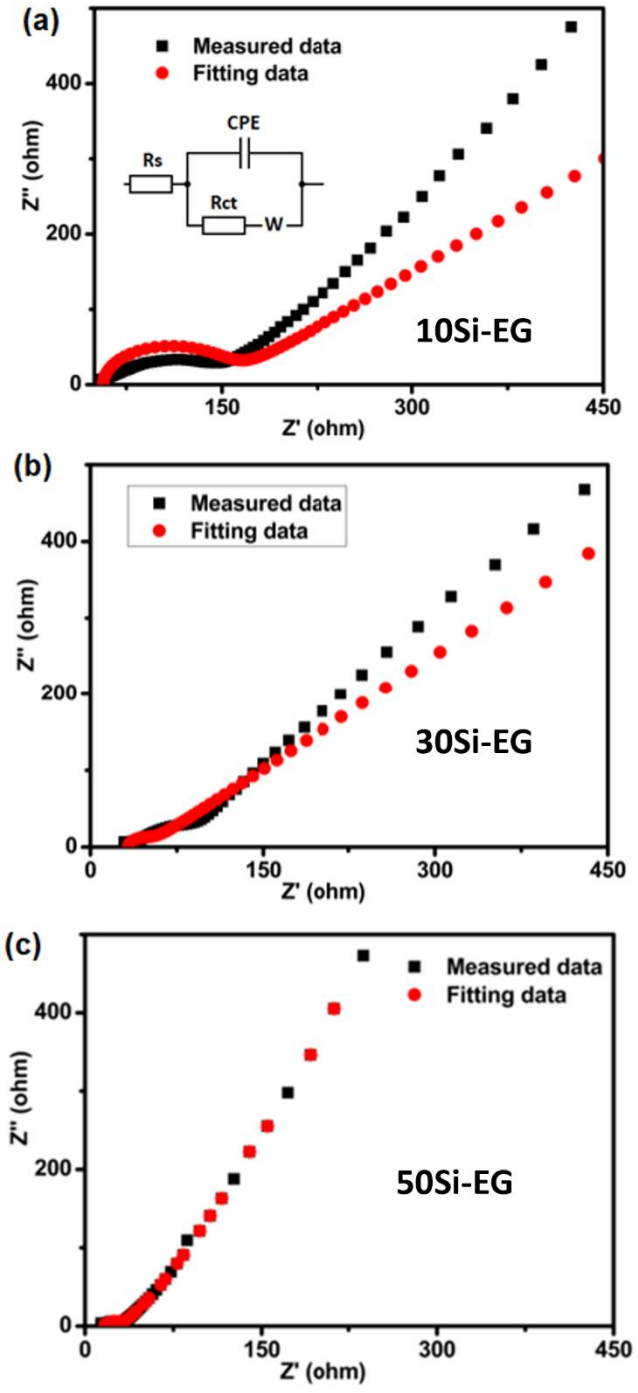

Figure 5.17 Electrochemical impedance spectra for the Si-EG composite anodes after 5 cycles, in a range of 100 kHz to 0.01 Hz, with an amplitude of 5 mV. Figure 5.17 (a) inset demonstrates the equivalent circuit model.

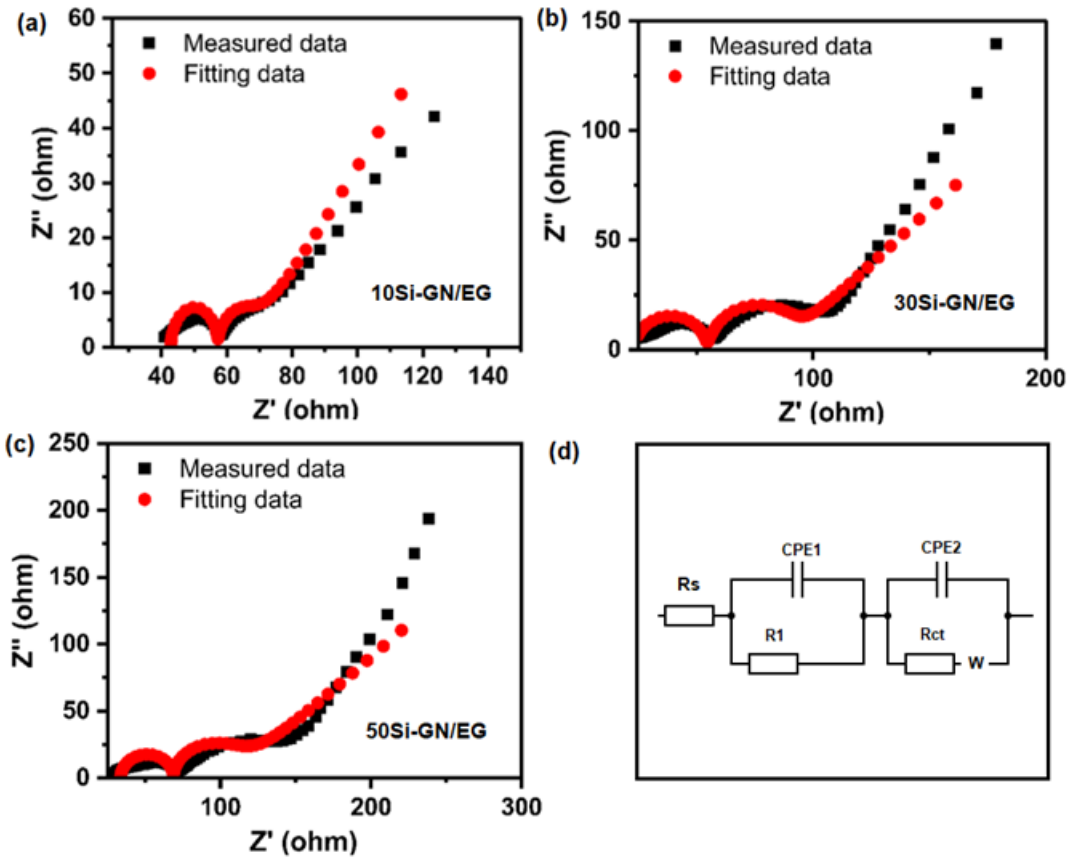

Figure 5.18 Electrochemical impedance spectra for the Si-EG composite anodes after 100 cycles at 0.8 C, in a range of 100 kHz to 0.01 Hz, with an amplitude of 5 mV. Figure 5.18 (d) shows the equivalent circuit model.

Table 5.3 The electrochemical impedance spectroscopy (EIS) resistance factors following the 5th and 100th cycle.

Composite	**After 5th cycle**		**After 100th cycle**		
	R_s (Ω)	**R_{ct} (Ω)**	**R_s (Ω)**	**R_1(Ω)**	**R_{ct} (Ω)**
10Si-EG	56.9	95.1	42.9	14.4	11.2
30Si-EG	32.9	18.1	23.3	32.3	30.5
50Si-EG	15.3	15.2	33.8	34.9	44.0

After 5 cycles, the 10Si-EG electrode presents the highest total resistance with R_s of 56.9 Ω and R_{ct} of 95.1 Ω. The lowest resistance values were shown by 50Si-EG as 15.3 Ω and 15.2 Ω for R_s and R_{ct}, respectively. Similarly, the 30Si-EG electrode exhibits average resistance values of 32.9 Ω for R_s and 18.1 Ω for R_{ct}. There seems to be a discrepancy between this behaviour and the excellent conductivity of graphite. It can be hypothesized that high mass ratios of graphite can lead to thick electrodes, hindering electrolyte accessibility and resulting in increased resistance (Dubey et al. 2021).

After 100 cycles, a second depressed semi-circle radius appears in the impedance spectrum as the interface layer grows (Guo et al. 2011). The equivalent series resistance (R_s), ohmic resistance (R_1), and charge transfer resistance (R_{ct}) are obtained. As the cycling progresses, the volume of Si material increases, leading to cracks, further degradation of the electrolyte, and an increase in the thickness of the solid electrolyte interface (SEI) film. Consequently, a new resistance, R_1, emerges (Guo et al. 2011; Lu 2015; Sun et al. 2016; R-Smith et al. 2021). As revealed in **Table 5.3**, the R_1 growths with an increasing Si content (10%, 30%, and 50%), confirming the growth of resistance due to Si pulverisation.

The impact of R_{ct} on the performance of Li-ion batteries is widely recognised, as a lower R_{ct} facilitates rapid electrochemical electron and ion transportation kinetics (Li et al. 2016; Espinosa-Villatoro et al. 2021). Upon completing 100 cycles, the 10Si-EG electrode exhibits the least R_{ct} value of 11.2 Ω, indicating favourable electrochemical kinetics. In contrast, the 50Si-EG electrode demonstrates the highest Rct value of 44 Ω, suggesting sluggish kinetics. The 30Si-EG electrode falls in between with an R_{ct} value of 30.5 Ω. The observed

rapid increase in R_{ct} with higher Si mass loading suggests that there is an increased probability of structural electrode disintegration over the cycling. The degradation of the Si structure leads to changes in reaction kinetics, which in turn increases the charge-transfer barrier. This alteration ultimately results in a higher R_{ct} value (Zhuang et al. 2012; Macdonald and Barsoukov 2018).

Because of the low resistance values in both R_1 and R_{ct}, the 10Si-EG shows the best cycling stability corresponding to the maintenance of Si crystallinity. In contrast, 50Si-EG reveals the worst cycling stability, comparatively higher R_1 and R_{ct} and lower Si crystallinity due to severe structural degradation and volume change.

Based on the electrochemical findings discussed above, it can be concluded that the 30Si-EG composite exhibited the most favourable Li-ion storage performance concerning energy, power, cycle life, and impedance when compared to the 10Si-EG and 50Si-EG composites.

5.4 Conclusions

In this chapter, a cost-effective and scalable hydrothermal exfoliation method was proposed for synthesizing exfoliated graphene composites (EG) from natural flake graphite. Then proceeded to prepare Si/EG composites with three different weight percentages of silicon (Si), denoted as 10Si-EG, 30Si-EG, and 50Si-EG, which corresponded to Si contents of 10%, 30%, and 50%, respectively. The objective was to investigate how the mass ratio of Si to exfoliated graphene influences the electrochemical characteristics of anodic lithium-ion batteries, to identify the optimal Si to exfoliated graphene ratio.

Based on our electrochemical analysis, the 30Si-EG composite exhibited the most favourable lithium-ion storage performance when compared to the 10Si-

EG and 50Si-EG composites. Notably, the 30Si-EG composite demonstrated a significantly improved lifespan in comparison to the other composites. After 600 cycles at a specific current flow of 0.8 C, it managed to retain 16% of its initial specific Li-ion storage of 499.2 mAh g^{-1}. Impressively, even at a high specific current flow of 1.2 C, the specific capacity remained stable at approximately 309.2 mAh g^{-1}.

This remarkable electrochemical performance can be primarily attributed to the optimised Si/EG mass ratio, which enhances cycling performance by increasing conductivity, providing a reasonable surface area, and promoting porosity. Additionally, the synergistic effects between the exfoliated graphene and Si nanoparticles made a significant contribution to these outcomes.

The limitations of this research include the absence of full cell testing of the Si/graphene composite with a cathode material. Additionally, post-mortem analysis of the electrodes would be valuable for elucidating the ageing mechanisms of the Si.

Chapter 6 Conclusions and Future Works

Undoubtedly, Li-ion batteries will persist as the predominant power source for modern portable energy storage devices. However, there is a pressing need to enhance the energy densities of Li-ion batteries, particularly for emerging applications like electric vehicles. To address this challenge and support large-scale energy storage, anodes based on Si and transition metal oxides show promise due to their high energy performance. Yet, their inherent insulating nature and considerable volume expansion present obstacles to their exclusive application in Li-ion batteries. A well-established strategy to overcome these hurdles is the integration of graphene into these high-capacity materials. This dissertation focuses on the advancement of innovative graphene-based nanocomposites for Li-ion battery anode, aiming to improve their electrochemical performance.

In Chapter 4, a nanocomposite anode is introduced, featuring NiO on a 3D carbon system formed by expanding graphite into nanoflower structures (referred to as NiO/GNF). This configuration enhances the electrochemical performance of the Li-ion battery anode. However, a significant drawback of NiO lies in its limited availability and high cost. As an alternative system, commercial anode for lithium-ion batteries, graphene/Si nano assembly is presented in Chapter 5.

The key findings of this thesis study are as follows:

- Hydrothermal exfoliation of graphite proves to be an environmentally friendly, scalable, and cost-effective method for generating graphene sheets.
- A NiO/GNF composite was successfully developed through a one-step hydrothermal synthesis, involving the transformation of graphitic particles into graphene nanosheets encapsulating NiO nanoparticles. The integration of expanded graphite with NiO nanostructures resulted in significant improvements in electrochemical performance, electrode integrity, and Li-ion storage capacity. The synergistic interaction between expanded graphite and NiO led to a remarkable 22.4% increase in capacity retention, along with a substantial energy improvement of 324 mAh g^{-1} compared to pristine NiO in Lithium-ion battery applications. The NiO-GNF exhibited outstanding electrochemical performance, achieving approximately 678.2 mAh g^{-1} at a specific current flow of 0.5 A g^{-1} over 370 cycles, surpassing previous carbon-based NiO composites.
- Si/EG composites were synthesised with varying silicon (Si) weight percentages (10Si-EG, 30Si-EG, and 50Si-EG) to assess their impact on the electrochemical characteristics of anodic lithium-ion batteries. Among these, the 30Si-EG composite demonstrated superior lithium-ion storage performance, maintaining 16% of its initial specific capacity (499.2 mAh g^{-1}) after 600 service life at 0.8 C. Notably, even at an elevated current flow of 1.2 C, the specific capacity remained stable at approximately 309.2 mAh g^{-1}. This outstanding performance is ascribed to the optimised Si/EG mass ratio, which improves cycling performance

through enhanced conductivity, surface measurements, and porosity. The positive outcomes are further credited to the synergistic influences involving exfoliated graphene and Si nanoparticles.

6.1 Recommendations for future directions

The following recommendations are based on the research results collected in this thesis work:

Future work entails the comprehensive evaluation of both NiO-graphene and Si-exfoliated graphene anode composites through full-cell testing, utilising lithium cobalt oxide (LCO) as the cathode. Although half-cell results offer insights, they may not fully capture material performance in practical industrial applications, given the unlimited Li supply from the counter electrode during the cycling process. Consequently, conducting an analysis with the cathode material in a full-cell configuration will provide more reliable and commercially applicable results.

Recommend conducting a postmortem analysis of the anode to evaluate the ageing mechanism of the composites.

To further boost power performance, it is quite common in industrial anode formulation to incorporate a small quantity (0.2-0.5% by weight) of single-walled carbon nanotubes (SWCNTs). These nanotubes serve as a network, intricately weaving through the nanoparticles and establishing a sturdy connection among them. This interwoven structure notably enhances the overall electrode conductivity, thus elevating the electrochemical power performance.

Recommend evaluating the optimised NiO content in the NiO-graphene composite to assess the balanced Li-ion battery performance. This evaluation will focus on understanding how the conductive network of exfoliated graphene interacts with the high-capacitive NiO, aiming for an optimal balance in battery performance.

Recommend exploring the application of similar hydrothermal synthesis techniques to produce the latest industrial-scale metal oxide anode materials, such as niobium oxide. With abundant Nb-oxide ores available in regions like Brazil and Canada, and considering its exceptional safety profile, impressive power performance (exceeding 15C), and remarkable cycle life (surpassing 10,000 cycles), niobium oxide presents itself as a promising candidate. Moreover, niobium oxide competes favourably with LTO (Lithium Titanium Oxide) anodes, boasting a slightly higher capacity of 200 mAh/g compared to LTO's 170 mAh/g. This elevated capacity positions niobium oxide as a strong candidate in various applications, especially in high-power demands seen in energy storage systems and sports vehicles (Butts 2022; da Silva Lima et al. 2023).

Investigating the solvothermal in-situ synthesis of the Si-graphene composite using organic solvents like N, N-Dimethylformamide, Ethylene glycol, and Propylene glycol holds possibilities. This approach can prevent Si oxidation and facilitate stronger interaction between Si and exfoliated graphene. A well-connected Si-graphene structure can offer superior mechanical stability, promote stable SEI formation, and enhance safety in LiBs.

References

AbdelHamid, A. A., Mendoza-Garcia, A. and Ying, J. Y., 2022. Advances in and prospects of nanomaterials' morphological control for lithium rechargeable batteries. *Nano Energy*, 93, 106860.

Amprius Technologies, 2024. *Amprius Technologies Silicon Anode Batteries*. Amprius Technologies.https://amprius.com/.

Amrouche, S. O., Rekioua, D., Rekioua, T. and Bacha, S. J. I. j. o. h. e., 2016. Overview of energy storage in renewable energy systems. *International Journal of Hydrogen Energy*, 41 (45), 20914-20927.

An, W., Gao, B., Mei, S., Xiang, B., Fu, J., Wang, L., Zhang, Q., Chu, P. K. and Huo, K., 2019. Scalable synthesis of ant-nest-like bulk porous silicon for high-performance lithium-ion battery anodes. *Nature communications*, 10 (1), 1447.

Armand, M. and Tarascon, J.-M. J. n., 2008. Building better batteries. *Nature,* 451 (7179), 652-657.

Arora, P. and Zhang, Z., 2004. Battery separators. *Chemical reviews*, 104 (10), 4419-4462.

Ashuri, M., He, Q. and Shaw, L. L., 2016. Silicon as a potential anode material for Li-ion batteries: where size, geometry and structure matter. *Nanoscale*, 8 (1), 74-103.

Aurbach, D., Zinigrad, E., Cohen, Y. and Teller, H., 2002. A short review of failure mechanisms of lithium metal and lithiated graphite anodes in liquid electrolyte solutions. *Solid state ionics*, 148 (3-4), 405-416.

Bai, L.-Z., Zhao, D.-L., Zhang, T.-M., Xie, W.-G., Zhang, J.-M. and Shen, Z.-M. J. E. A., 2013. A comparative study of electrochemical performance of graphene sheets, expanded graphite and natural graphite as anode materials for lithium-ion batteries. *Electrochimica Acta*, 107, 555-561.

Beck, F. R., Epur, R., Hong, D., Manivannan, A. and Kumta, P. N., 2014. Microwave derived facile approach to Sn/graphene composite anodes for, lithium-ion batteries. *Electrochimica Acta*, 127, 299-306.

Betti, M. G., Gemmi, M., Mariani, C. and Panero, S., An Advanced Lithium-Ion Battery Based on a Graphene Anode and a Lithium Iron Phosphate Cathode. *Nano Letters*, 14 (8), 4901–4906.

Boeva, Z. A., Milakin, K. A., Pesonen, M., Ozerin, A. N., Sergeyev, V. G. and Lindfors, T. J. R. A., 2014. Dispersible composites of exfoliated graphite and polyaniline with improved electrochemical behaviour for solid-state chemical sensor applications. *RSC Advances*, 4 (86), 46340–46350.

Bourderau, S., Brousse, T. and Schleich, D. M., 1999. Amorphous silicon as a possible anode material for Li-ion batteries. *Journal of power sources*, 81, 233-236.

Brodie, B. C., 1859. XIII. On the atomic weight of graphite. *Philosophical transactions of the Royal Society of London*, (149), 249-259.

Buchmann, I., 2001. Batteries in a portable world: a handbook on rechargeable batteries for non-engineers. *2nd ed.*

Butts, D., 2022. *Next-generation Electrode Materials for Na-and Li-ion Batteries*. University of California, Los Angeles.

Canal-Rodríguez, M., Arenillas, A., Menéndez, J. A., Beneroso, D. and Rey-Raap, N. J. C., 2018. Carbon xerogels graphitized by microwave heating as anode materials in lithium-ion batteries. *Carbon,* 137, 384-394.

Cao, K., Jin, T., Yang, L. and Jiao, L., 2017. Recent progress in conversion reaction metal oxide anodes for Li-ion batteries. *Materials Chemistry Frontiers*, 1 (11), 2213-2242.

Cao, Z. and Wei, B., 2015. A facile route to metal oxides/single-walled carbon nanotube macrofilm nanocomposites for energy storage. *Frontiers in Materials*, 2, 40.

Celasco, E., Chaika, A. N., Stauber, T., Zhang, M., Ozkan, C. S., Ozkan, U. S., Palys, B. and Harun, S. W., 2019. Handbook of graphene.

Cen, Y., Sisson, R. D., Qin, Q. and Liang, J. J. C., 2018. Current progress of Si/graphene nanocomposites for lithium-ion batteries. *C*, 4 (1), 18.

Chang, K., Wang, Z., Huang, G., Li, H., Chen, W. and Lee, J. Y., 2012. Few-layer SnS2/graphene hybrid with exceptional electrochemical performance as lithium-ion battery anode. *Journal of Power Sources*, 201, 259-266.

Cheekati, S. L., 2011. Graphene based anode materials for Lithium-ion batteries.

Chen, G., Weng, W., Wu, D., Wu, C., Lu, J., Wang, P. and Chen, X. J. C., 2004. Preparation and characterization of graphite nanosheets from ultrasonic powdering technique. *Carbon,* 42 (4), 753-759.

Chen, J., Wang, Z., Mu, J., Ai, B., Zhang, T., Ge, W. and Zhang, L., 2019. Enhanced lithium storage capability enabled by metal nickel dotted NiO–graphene composites. *Journal of materials science*, 54 (2), 1475-1487.

Chen, J., Wu, X., Liu, Y., Gong, Y., Wang, P., Li, W., Mo, S., Tan, Q. and Chen, Y., 2017. Hierarchically-structured hollow NiO nanospheres/nitrogen-doped graphene hybrid with superior capacity retention and enhanced rate capability for lithium-ion batteries. *Applied Surface Science*, 425, 461-469.

Chen, J., Wu, X., Tan, Q. and Chen, Y., 2018. Designed synthesis of ultrafine NiO nanocrystals bonded on a three dimensional graphene framework for high-capacity lithium-ion batteries. *New Journal of Chemistry*, 42 (12), 9901-9910.

Chen, X., Xiao, F., Lei, Y., Lu, H., Zhang, J., Yan, M. and Xu, J. J. J. E. C., 2021. A novel approach for synthesis of expanded graphite and its enhanced lithium storage properties. *Journal of Energy Chemistry*, 59, 292-298.

Cheng, H., Shapter, J. G., Li, Y. and Gao, G., 2021. Recent progress of advanced anode materials of lithium-ion batteries. *Journal of Energy Chemistry*, 57, 451-468.

Cheng, Q., Okamoto, Y., Tamura, N., Tsuji, M., Maruyama, S. and Matsuo, Y. J. S. r., 2017. Graphene-like-graphite as fast-chargeable and high-capacity anode materials for lithium ion batteries. *Scientific reports*, 7 (1), 1-14.

Coleman, J. N., 2009. Liquid-phase exfoliation of nanotubes and graphene. *Advanced Functional Materials*, 19 (23), 3680-3695.

Concheso, A., Santamaría, R., Menéndez, R., Alcántara, R., Lavela, P. and Tirado, J., 2006. Influence of the oxidative stabilisation treatment time on the electrochemical performance of anthracene oils cokes as electrode materials for lithium batteries. *Journal of power sources*, 161 (2), 1324-1334.

da Silva Lima, L., Wu, J., Cadena, E., Groombridge, A. S. and Dewulf, J., 2023. Towards environmentally sustainable battery anode materials: Life cycle assessment of mixed niobium oxide (XNO™) and lithium-titanium-oxide (LTO). *Sustainable Materials and Technologies*, 37, e00654.

Dai, K., Wang, Z., Ai, G., Zhao, H., Yuan, W., Song, X., Battaglia, V., Sun, C., Wu, K. and Liu, G. J. J. o. P. S., 2015. The transformation of graphite electrode materials in lithium-ion batteries after cycling. *Journal of Power Sources*, 298, 349-354.

Dash, R. and Pannala, S., 2019. Theoretical Limits of Energy Density in Silicon-Carbon Composite Anode Based Lithium Ion Batteries (Retraction of Vol 6, art no 27449, 2016): NATURE PUBLISHING GROUP MACMILLAN BUILDING, 4 CRINAN ST, LONDON N1 9XW, ENGLAND.

De las Casas, C. and Li, W. J. J. o. P. S., 2012. A review of application of carbon nanotubes for lithium ion battery anode material. *Journal of Power Sources,* 208, 74-85.

Dell, R. and Rand, D. A. J., 2001. *Understanding batteries*. Royal society of chemistry.

Deng, Y., Fang, C. and Chen, G., 2016. The developments of SnO2/graphene nanocomposites as anode materials for high performance lithium ion batteries: a review. *Journal of Power Sources*, 304, 81-101.

Ding, X., Wang, H., Liu, X., Gao, Z., Huang, Y., Lv, D., He, P. and Huang, Y. J. R. a., 2017. Advanced anodes composed of graphene encapsulated nano-silicon in a carbon nanotube network. *RSC advances,* 7 (26), 15694-15701.

Diouf, B. and Pode, R. J. R. E., 2015. Potential of lithium-ion batteries in renewable energy. *Renewable Energy,* 76, 375-380.

Duan, J., Tang, X., Dai, H., Yang, Y., Wu, W., Wei, X. and Huang, Y. J. E. E. R., 2020. Building safe lithium-ion batteries for electric vehicles: a review. *Electrochemical Energy Reviews,* 3, 1-42.

Dubarry, M., Truchot, C., Cugnet, M., Liaw, B. Y., Gering, K., Sazhin, S., Jamison, D. and Michelbacher, C. J. J. o. p. s., 2011. Evaluation of commercial lithium-ion cells based on composite positive electrode for plug-in hybrid electric vehicle applications. Part I: Initial characterizations. *Journal of power sources,* 196 (23), 10328-10335.

Dubey, R., Zwahlen, M. D., Shynkarenko, Y., Yakunin, S., Fuerst, A., Kovalenko, M. V. and Kravchyk, K. V., 2021. Laser patterning of high-mass-loading graphite anodes for high-performance Li-ion batteries. *Batteries & Supercaps*, 4 (3), 464-468.

Espinosa-Villatoro, E., Weker, J. N., Ko, J. S. and Quiroga-González, E. J. J. o. E. C., 2021. Tracking the evolution of processes occurring in silicon anodes in lithium ion batteries by 3D visualization of relaxation times. *Electroanalytical Chemistry,* 892, 115309.

Fan, Z., Liang, J., Yu, W., Ding, S., Cheng, S., Yang, G., Wang, Y., Xi, Y., Xi, K. and Kumar, R. V., 2015. Ultrathin NiO nanosheets anchored on a highly ordered nanostructured carbon as an enhanced anode material for lithium ion batteries. *Nano Energy*, 16, 152-162.

Fang, S., Shen, L. and Zhang, X., 2017. Application of carbon nanotubes in lithium-ion batteries. *Industrial applications of carbon nanotubes.* Elsevier, 251-276.

Fang, T., Duh, J.-G. and Sheen, S.-R., 2005. Improving the electrochemical performance of LiCoO2 cathode by nanocrystalline ZnO coating. *Journal of the Electrochemical Society*, 152 (9), A1701.

Feng, Y., Zhang, H., Li, W., Fang, L. and Wang, Y., 2016. Targeted synthesis of novel hierarchical sandwiched NiO/C arrays as high-efficiency lithium ion batteries anode. *Journal of Power Sources*, 301, 78-86.

Fernando, N., Chinnappan, A., Aziz, A., Abdelkader, A., Ramakrishna, S. and Welland, M. E., 2021. Flexible free-standing Ni–Mn oxide antenna decorated CNT/nanofiber membrane for high-volumetric capacitance supercapacitors. *Nanoscale*, 13 (45), 19038-19048.

Fernando, N., Kannan, H., Hernandez, F. C. R., Ajayan, P. M., Meiyazhagan, A. and Abdelkader, A. M., 2023. Graphitic nanostructure integrated NiO composites for high-performance lithium-ion batteries. *Journal of Energy Storage*, 71, 108015.

Ferralis, N. J. J. o. m. s., 2010. Probing mechanical properties of graphene with Raman spectroscopy. *Journal of materials science,* 45, 5135-5149.

Ferrari, A. C., Meyer, J. C., Scardaci, V., Casiraghi, C., Lazzeri, M., Mauri, F., Piscanec, S., Jiang, D., Novoselov, K. S. and Roth, S. J. P. r. l., 2006. Raman spectrum of graphene and graphene layers. *Physical review letters*, 97 (18), 187401.

Ferrari, A. C. and Robertson, J. J. P. r. B., 2000. Interpretation of Raman spectra of disordered and amorphous carbon. *Physical review letters,* 61 (20), 14095.

Ferrari, A. C. J. S. s. c., 2007. Raman spectroscopy of graphene and graphite: Disorder, electron–phonon coupling, doping and nonadiabatic effects. *Solid state communications,* 143 (1-2), 47-57.

Fu, J., Kang, W., Guo, X., Wen, H., Zeng, T., Yuan, R. and Zhang, C., 2020. 3D hierarchically porous NiO/graphene hybrid paper anode for long-life and high rate cycling flexible Li-ion batteries. *Journal of Energy Chemistry*, 47, 172-179.

Gaines, L. J. S. m. and technologies, 2018. Lithium-ion battery recycling processes: Research towards a sustainable course. *Sustainable materials and technologies,* 17, e00068.

Gaskell, P. E., 2017. *Nanocomposite silicon and graphene composite negative electrode materials for lithium ion batteries*. McGill University (Canada).

Goodenough, J. B. and Kim, Y. J. C. o. m., 2010. Challenges for rechargeable Li batteries. *Chemistry of materials,* 22 (3), 587-603.

Goodenough, J. B. and Mizuchima, K., 1981. Electrochemical cell with new fast ion conductors: Google Patents.

Griffith, K. J., Harada, Y., Egusa, S., Ribas, R. M., Monteiro, R. S., Von Dreele, R. B., Cheetham, A. K., Cava, R. J., Grey, C. P. and Goodenough, J. B., 2020. Titanium niobium oxide: from discovery to application in fast-charging lithium-ion batteries. *Chemistry of Materials*, 33 (1), 4-18.

Global Graphene Group, 2024. https://www.theglobalgraphenegroup.com/.

Gu, M., He, Y., Zheng, J. and Wang, C. J. N. E., 2015. Nanoscale silicon as anode for Li-ion batteries: The fundamentals, promises, and challenges. *Nano Energy,* 17, 366-383.

Guo, J., Sun, A., Chen, X., Wang, C. and Manivannan, A. J. E. A., 2011. Cyclability study of silicon–carbon composite anodes for lithium-ion batteries using electrochemical impedance spectroscopy. *Electrochimica Acta*, 56 (11), 3981-3987.

Guo, Z., Zhu, J., Feng, J. and Du, S. J. R. a., 2015. Direct in situ observation and explanation of lithium dendrite of commercial graphite electrodes. *RSC advances,* 5 (85), 69514-69521.

Hadi, A., Zahirifar, J., Karimi-Sabet, J. and Dastbaz, A. J. U. s., 2018. Graphene nanosheets preparation using magnetic nanoparticle assisted liquid phase exfoliation of graphite: the coupled effect of ultrasound and wedging nanoparticles. *Ultrasonics sonochemistry*, 44, 204-214.

Han, Y., Zhou, J., Li, T., Yi, Z., Lin, N. and Qian, Y., 2018. Molten-salt chemical exfoliation process for preparing two-dimensional mesoporous Si nanosheets as high-rate Li-storage anode. *Nano Research*, 11 (12), 6294-6303.

Handwerker, M., Wellnitz, J. and Marzbani, H. J. H., 2021. Comparison of hydrogen powertrains with the battery powered electric vehicle and investigation of small-scale local hydrogen production using renewable energy. *Hydrogen,* 2 (1), 76-100.

Hu, J., Liu, Y., Liu, N., Li, J. and Ouyang, C. J. P. C. C. P., 2020. Theoretical prediction of T-graphene as a promising alkali-ion battery anode offering ultrahigh capacity. *Physical Chemistry Chemical Physics,* 22 (6), 3281-3289.

Hu, R., Sun, W., Chen, Y., Zeng, M. and Zhu, M. J. J. o. M. C. A., 2014. Silicon/graphene based nanocomposite anode: large-scale production and stable high capacity for lithium ion batteries. *Journal of Materials Chemistry A,* 2 (24), 9118-9125.

Huang, H.-D., Zhou, S.-Y., Ren, P.-G., Ji, X. and Li, Z.-M. J. R. a., 2015. Improved mechanical and barrier properties of low-density polyethylene nanocomposite films by incorporating hydrophobic graphene oxide nanosheets. *RSC advances*, 5 (98), 80739-80748.

Huang, W., Ding, S., Chen, Y., Hao, W., Lai, X., Peng, J., Tu, J., Cao, Y. and Li, X., 2017. 3D NiO hollow sphere/reduced graphene oxide composite for high-performance glucose biosensor. *Scientific reports*, 7 (1), 5220.

Huang, X., Qi, X., Boey, F. and Zhang, H., 2012. Graphene-based composites. *Chemical Society Reviews*, 41 (2), 666-686.

Huang, X., Xia, X., Yuan, Y. and Zhou, F., 2011. Porous ZnO nanosheets grown on copper substrates as anodes for lithium ion batteries. *Electrochimica Acta*, 56 (14), 4960-4965.

Huggins, R., 2008. *Advanced batteries: materials science aspects*. Springer Science & Business Media.

Huggins, R. A. and Huggins, R. A. J. E. S., 2010. Thermal energy storage. 21-27.

Iftikhar, M., Latif, S., Jevtovic, V., Ashraf, I., El-Zahhar, A. A., Saleh, E. A. M. and Abbas, S. M., 2022. Current advances and prospects in NiO-based lithium-ion battery anodes. *Sustainable Energy Technologies and Assessments*, 53, 102376.

Itagaki, M., Kobari, N., Yotsuda, S., Watanabe, K., Kinoshita, S. and Ue, M., 2004. In situ electrochemical impedance spectroscopy to investigate negative electrode of lithium-ion rechargeable batteries. *Journal of Power Sources*, 135 (1-2), 255-261.

Jang, D. H., Shin, Y. J. and Oh, S. M., 1996. Dissolution of spinel oxides and capacity losses in 4 V li/li x Mn2 O 4 cells. *Journal of the Electrochemical Society*, 143 (7), 2204.

Johra, F. T., Lee, J.-W., Jung, W.-G. J. J. o. I. and Chemistry, E., 2014. Facile and safe graphene preparation on solution based platform. *Industrial and Engineering Chemistry*, 20 (5), 2883-2887.

Jung, S., McCrory, C. C., Ferrer, I. M., Peters, J. C. and Jaramillo, T. F., 2016. Benchmarking nanoparticulate metal oxide electrocatalysts for the alkaline water oxidation reaction. *Journal of Materials Chemistry A*, 4 (8), 3068-3076.

Kafle, B. P., 2020. Introduction to nanomaterials and application of UV–Visible spectroscopy for their characterization. *Chemical analysis and material characterization by spectrophotometry*, 6, 147-198.

Kanakaiah, V., Latha, M., Sravan, B., Palanisamy, A. and Rani, J. V. J. J. o. T. E. S., 2014. Rechargeable magnesium carbon-fluoride battery with electrolyte gel of ionic liquid and low molecular weight gelator. *Journal of The Electrochemical Society,* 161 (10), A1586.

Karden, E., Ploumen, S., Fricke, B., Miller, T. and Snyder, K., 2007. Energy storage devices for future hybrid electric vehicles. *Journal of Power Sources*, 168 (1), 2-11.

Kasavajjula, U., Wang, C. and Appleby, A. J., 2007. Nano-and bulk-silicon-based insertion anodes for lithium-ion secondary cells. *Journal of power sources*, 163 (2), 1003-1039.

Khan, B. M., Oh, W. C., Nuengmatch, P. and Ullah, K., 2023. Role of graphene-based nanocomposites as anode material for Lithium-ion batteries. *Materials Science and Engineering: B*, 287, 116141.

Kordesch, K. V., 1977. Batteries. Volume II. Lead--acid batteries and electric vehicles.

Kottegoda, I. R., Idris, N. H., Lu, L., Wang, J.-Z. and Liu, H.-K., 2011. Synthesis and characterization of graphene–nickel oxide nanostructures for fast charge–discharge application. *Electrochimica Acta*, 56 (16), 5815-5822.

Laziz, N. A., Abou-Rjeily, J., Darwiche, A., Toufaily, J., Outzourhit, A., Ghamouss, F., Sougrati, M. T. J. J. o. E. S. and Technology, 2018. Li-and Na-ion storage performance of natural graphite via simple flotation process. *Journal of Electrochemical Science and Technology*, 9 (4), 320-329.

Lazzari, M. and Scrosati, B. J. J. o. T. E. S., 1980. A cyclable lithium organic electrolyte cell based on two intercalation electrodes. *Journal of The Electrochemical Society*, 127 (3), 773.

Lee, J. K., Smith, K. B., Hayner, C. M. and Kung, H. H., 2010. Silicon nanoparticles–graphene paper composites for Li ion battery anodes. *Chemical communications*, 46 (12), 2025-2027.

Lee, Y., Jeghan, S. M. N. and Lee, G. J. M. L., 2021. Boost charging lithium-ion battery using expanded graphite anode with enhanced performance. *Materials Letters*, 299, 130077.

Li, C., Shi, T., Yoshitake, H. and Wang, H. J. J. o. M. C. A., 2016a. Improved performance in micron-sized silicon anodes by in situ polymerization of acrylic acid-based slurry. *Journal of Materials Chemistry A,* 4 (43), 16982-16991.

Li, D., Wang, K., Tao, H., Hu, X., Cheng, S. and Jiang, K., 2016. Facile synthesis of an Fe 3 O 4/FeO/Fe/C composite as a high-performance anode for lithium-ion batteries. *RSC advances*, 6 (92), 89715-89720.

Li, G., Li, Y., Chen, J., Zhao, P., Li, D., Dong, Y. and Zhang, L., 2017. Synthesis and research of egg shell-yolk NiO/C porous composites as lithium-ion battery anode material. *Electrochimica Acta*, 245, 941-948.

Li, H., Zhao, Q., Li, X., Zhu, Z., Tade, M. and Liu, S. J. J. o. n. r., 2013. Fabrication, characterization, and photocatalytic property of α-Fe 2 O 3/graphene oxide composite. *Journal of nanoparticle research,* 15, 1-11.

Li, J.-Y., Xu, Q., Li, G., Yin, Y.-X., Wan, L.-J. and Guo, Y.-G. J. M. C. F., 2017b. Research progress regarding Si-based anode materials towards practical application in high energy density Li-ion batteries. *Electrochimica Acta*, 1 (9), 1691-1708.

Li, J., Li, J. and Li, M. J. M. L., 2007. Preparation of expandable graphite with ultrasound irradiation. *Materials Letters*, 61 (28), 5070-5073.

Li, J., Zhang, Y., Li, L., Wang, Y., Zhang, L., Zhang, B. and Wang, F., 2020. Formation of dumbbell and sphere-like CuO as high-performance anode materials for lithium ion batteries. *Materials Letters*, 261, 127058.

Li, M., Lu, J., Chen, Z. and Amine, K. J. A. M., 2018. 30 years of lithium-ion batteries. *Advanced Materials,* 30 (33), 1800561.

Li, P., Kim, H., Myung, S.-T. and Sun, Y.-K., 2021a. Diverting exploration of silicon anode into practical way: a review focused on silicon-graphite composite for lithium ion batteries. *Energy Storage Materials*, 35, 550-576.

Li, Q., 2016. *Silicon Anode Materials for Next Generation Lithium-Ion Batteries.* The University of Western Ontario (Canada).

Li, S., Liu, Y.-M., Zhang, Y.-C., Song, Y., Wang, G.-K., Liu, Y.-X., Wu, Z.-G., Zhong, B.-H., Zhong, Y.-J. and Guo, X.-D., 2021. A review of rational design and investigation of binders applied in silicon-based anodes for lithium-ion batteries. *Journal of Power Sources*, 485, 229331.

Li, X., Dhanabalan, A. and Wang, C., 2011. Enhanced electrochemical performance of porous NiO–Ni nanocomposite anode for lithium ion batteries. *Journal of Power Sources*, 196 (22), 9625-9630.

Li, X., Fan, L., Li, X., Shan, H., Chen, C., Yan, B., Xiong, D. and Li, D., 2018. Enhanced anode performance of flower-like NiO/RGO nanocomposites for lithium-ion batteries. *Materials chemistry and physics*, 217, 547-552.

Lian, P., Zhu, X., Liang, S., Li, Z., Yang, W. and Wang, H., 2010. Large reversible capacity of high quality graphene sheets as an anode material for lithium-ion batteries. *Electrochimica Acta*, 55 (12), 3909-3914.

Liang, C., Gao, M., Pan, H., Liu, Y. and Yan, M., 2013. Lithium alloys and metal oxides as high-capacity anode materials for lithium-ion batteries. *Journal of alloys and compounds*, 575, 246-256.

Ling, C., Setzler, G., Lin, M.-W., Dhindsa, K. S., Jin, J., Yoon, H. J., Kim, S. S., Cheng, M. M.-C., Widjaja, N. and Zhou, Z. J. N., 2011. Electrical transport properties of graphene nanoribbons produced from sonicating graphite in solution. *Nanotechnology,* 22 (32), 325201.

Liu, L., Li, X., Zhang, G., Zhang, Z., Fang, C., Ma, H., Luo, W. and Liu, Z., 2019. Enhanced stability lithium-ion battery based on optimized graphene/Si nanocomposites by templated assembly. *ACS omega*, 4 (19), 18195-18202.

Liu, N., Wu, H., McDowell, M. T., Yao, Y., Wang, C. and Cui, Y. J. N. l., 2012. A yolk-shell design for stabilized and scalable Li-ion battery alloy anodes. *Nano letters,* 12 (6), 3315-3321.

Liu, W., Lu, C., Wang, X., Liang, K. and Tay, B. K., 2015. In situ fabrication of three-dimensional, ultrathin graphite/carbon nanotube/NiO composite as binder-free electrode for high-performance energy storage. *Journal of Materials Chemistry A*, 3 (2), 624-633.

Liu, W., Wang, J., Wang, J., Guo, X. and Yang, H., 2021. Three-dimensional nitrogen-doped carbon coated hierarchically porous silicon composite as lithium-ion battery anode. *Journal of Alloys and Compounds*, 874, 159921.

Liu, X., Zheng, M., Xiao, K., Xiao, Y., He, C., Dong, H., Lei, B. and Liu, Y., 2014. Simple, green and high-yield production of single-or few-layer graphene by hydrothermal exfoliation of graphite. *Nanoscale*, 6 (9), 4598-4603.

Liu, Y., Peng, W., Zhang, J., Li, S., Hu, R., Yuan, B. and Chen, G., 2022. Tuning the electronic properties of NiO anode by in-situ introducing metallic Cu for high capacity and long life-span lithium-ion batteries. *Journal of Alloys and Compounds*, 918, 165693.

Lu, G., Meng, G., Liu, Q., Feng, L., Luo, J., Liu, X., Luo, Y. and Chu, P. K., 2023. Advanced strategies for solid electrolyte interface design with MOF materials. *Advanced Powder Materials*, 100154.

Lu, X., 2015. *The Improvement of Electrochemical Performance of SnO 2-Based Nanocomposites As Anodes for Lithium Ion and Sodium Ion Batteries*. The University of Manchester (United Kingdom).

Luo, J., Zhao, X., Wu, J., Jang, H. D., Kung, H. H. and Huang, J., 2012. Crumpled graphene-encapsulated Si nanoparticles for lithium ion battery anodes. *The journal of physical chemistry letters*, 3 (13), 1824-1829.

Macdonald, J. R. and Barsoukov, E., 2018. *Impedance spectroscopy: theory, experiment, and applications*. John Wiley & Sons.

Mai, Y., Shi, S., Zhang, D., Lu, Y., Gu, C. and Tu, J. J. J. o. P. S., 2012. NiO–graphene hybrid as an anode material for lithium ion batteries. *Journal of Power Sources,* 204, 155-161.

Mao, C., Wood, M., David, L., An, S. J., Sheng, Y., Du, Z., Meyer, H. M., Ruther, R. E. and Wood, D. L. J. J. o. T. E. S., 2018. Selecting the best graphite for long-life, high-energy Li-ion batteries. *Journal of The Electrochemical Society,* 165 (9), A1837.

Marka, S. K. and Srikanth, V. V., 2015. Graphene and Graphene/Binary Transition Metal Oxide Compos-ites as Anode Materials in Li-Ion Batteries. *Nanoscience & Nanotechnology*, 5 (2), 91.

Martinet, S. J. N. f. S. E., 2016. Nanomaterials for rechargeable lithium batteries. *Nanomaterials for Sustainable Energy,* 471-512.

Mazar Atabaki, M. and Kovacevic, R. J. E. M. L., 2013. Graphene composites as anode materials in lithium-ion batteries. *Electronic Materials Letters*, 9, 133-153.

McAllister, M. J., Li, J.-L., Adamson, D. H., Schniepp, H. C., Abdala, A. A., Liu, J., Herrera-Alonso, M., Milius, D. L., Car, R. and Prud'homme, R. K., 2007. Single sheet functionalized graphene by oxidation and thermal expansion of graphite. *Chemistry of materials*, 19 (18), 4396-4404.

Modarres, M. H., 2018. *Reduced graphene oxide nanoparticle hybrids and their assembly for lithium-ion battery anodes.*

Mukanova, A., Nurpeissova, A., Kim, S. S., Myronov, M. and Bakenov, Z. J. C., 2018. N-Type Doped Silicon Thin Film on a Porous Cu Current Collector as the Negative Electrode for Li-Ion Batteries. *ChemistryOpen*, 7 (1), 92-96.

Nadimpalli, S. P., Sethuraman, V. A., Dalavi, S., Lucht, B., Chon, M. J., Shenoy, V. B. and Guduru, P. R. J. J. o. P. S., 2012. Quantifying capacity loss due to solid-electrolyte-interphase layer formation on silicon negative electrodes in lithium-ion batteries. *Journal of Power Sources,* 215, 145-151.

Nagaura, T. J. P. i. B. and Cells, S., 1990. Lithium ion rechargeable battery. *Journal of Power Sources*, 9, 209.

Nazri, G.-A. and Pistoia, G., 2008. *Lithium batteries: science and technology*. Springer Science & Business Media.

Ngala, J. K., Chernova, N. A., Ma, M., Mamak, M., Zavalij, P. Y. and Whittingham, M. S., 2004. The synthesis, characterization and electrochemical behavior of the layered LiNi 0.4 Mn 0.4 Co 0.2 O 2 compound. *Journal of materials chemistry*, 14 (2), 214-220.

Nguyen, H. T., Yao, F., Zamfir, M. R., Biswas, C., So, K. P., Lee, Y. H., Kim, S. M., Cha, S. N., Kim, J. M. and Pribat, D., 2011. Highly interconnected Si nanowires for improved stability Li-ion battery anodes. *Advanced energy materials*, 1 (6), 1154-1161.

Nishijima, M., Ootani, T., Kamimura, Y., Sueki, T., Esaki, S., Murai, S., Fujita, K., Tanaka, K., Ohira, K., Koyama, Y. and Tanaka, I., 2014. Accelerated discovery of cathode materials with prolonged cycle life for lithium-ion battery. *Nature Communications*, 5 (1), 4553.

Nitta, N., Wu, F., Lee, J. T. and Yushin, G., 2015. Li-ion battery materials: present and future. *Materials today*, 18 (5), 252-264.

Novoselov, K. S., Geim, A. K., Morozov, S. V., Jiang, D.-e., Zhang, Y., Dubonos, S. V., Grigorieva, I. V. and Firsov, A. A., 2004. Electric field effect in atomically thin carbon films. *science*, 306 (5696), 666-669.

Oh, J., Jin, D., Kim, K., Song, D., Lee, Y. M. and Ryou, M.-H. J. A. O., 2017. Improving the cycling performance of lithium-ion battery Si/graphite anodes using a soluble polyimide binder. *Acs Omega*, 2 (11), 8438-8444.

Ou, J., Wu, S., Yang, L. and Wang, H., 2021. Facile preparation of NiO@ graphene nanocomposite with superior performances as anode for Li-ion batteries. *Acta Metallurgica Sinica (English Letters)*, 1-11.

Pan, D., Wang, S., Zhao, B., Wu, M., Zhang, H., Wang, Y. and Jiao, Z. J. C. o. M., 2009. Li storage properties of disordered graphene nanosheets. *Chemistry of materials*, 21 (14), 3136-3142.

Pancaldi, G., 2005. *Volta: Science and culture in the age of enlightenment*. Princeton University Press.

Park, S.-H. and Lee, W.-J., 2015. Coaxial carbon nanofiber/NiO core–shell nanocables as anodes for lithium ion batteries. *RSC advances*, 5 (30), 23548-23555.

Qian, W., Hao, R., Hou, Y., Tian, Y., Shen, C., Gao, H. and Liang, X., 2009. Solvothermal-assisted exfoliation process to produce graphene with high yield and high quality. *Nano Research*, 2, 706-712.

Qiao, X., Liao, S., You, C. and Chen, R. J. C., 2015. Phosphorus and nitrogen dual doped and simultaneously reduced graphene oxide with high surface area as efficient metal-free electrocatalyst for oxygen reduction. *Catalysts,* 5 (2), 981-991.

Qin, D., Yan, P., Li, G., Wang, Y., An, Y. and Xing, J., 2014. Synthesis of hierarchical CoO nano/microstructures as anode materials for lithium-ion batteries. *Journal of Nanomaterials*, 2014.

Qiu, X., Bouchiat, V., Colombet, D. and Ayela, F. J. R. a., 2019. Liquid-phase exfoliation of graphite into graphene nanosheets in a hydrocavitating 'lab-on-a-chip'. *RSC advances,* 9 (6), 3232-3238.

Quan, J., Zhao, S., Song, D., Wang, T., He, W. and Li, G., 2022. Comparative life cycle assessment of LFP and NCM batteries including the secondary use and different recycling technologies. *Science of The Total Environment*, 819, 153105.

R-Smith, N. A.-Z., Leitner, M., Alic, I., Toth, D., Kasper, M., Romio, M., Surace, Y., Jahn, M., Kienberger, F. and Ebner, A. J. J. o. P. S., 2021. Assessment of lithium ion battery ageing by combined impedance spectroscopy, functional microscopy and finite element modelling. *Journal of Power Sources*, 512, 230459.

Raccichini, R., Varzi, A., Passerini, S. and Scrosati, B., 2015. The role of graphene for electrochemical energy storage. *Nature materials*, 14 (3), 271-279.

Raccichini, R., Varzi, A., Wei, D. and Passerini, S., 2017. Critical insight into the relentless progression toward graphene and graphene-containing materials for lithium-ion battery anodes. *Advanced materials*, 29 (11), 1603421.

Rahman, M. A., Rahman, M. M. and Song, G., 2022. A review on binder-free NiO-Ni foam as anode of high performance lithium-ion batteries. *Energy Storage*, 4 (3), e278.

Rai, A. K., Anh, L. T., Park, C.-J. and Kim, J., 2013. Electrochemical study of NiO nanoparticles electrode for application in rechargeable lithium-ion batteries. *Ceramics International*, 39 (6), 6611-6618.

Randviir, E. P., Brownson, D. A. and Banks, C. E., 2014. A decade of graphene research: production, applications and outlook. *Materials Today*, 17 (9), 426-432.

Rao, K. S., Senthilnathan, J., Liu, Y.-F. and Yoshimura, M. J. S. r., 2014. Role of peroxide ions in formation of graphene nanosheets by electrochemical exfoliation of graphite. *Scientific reports,* 4 (1), 4237.

Reddy, M., Rao, G. S. and Chowdari, B., 2010. Long-term cycling studies on 4 V-cathode, lithium vanadium fluorophosphate. *Journal of Power Sources*, 195 (17), 5768-5774.

Ren, H., Wen, Z., Chen, S., Liu, J., Joo, S. W. and Huang, J., 2019. Preparation of reduced graphene oxide@ nickel oxide nanosheets composites with enhanced lithium-ion storage performance. *Materials Chemistry and Physics*, 232, 229-239.

Ren, J.-G., Wang, C., Wu, Q.-H., Liu, X., Yang, Y., He, L. and Zhang, W., 2014. A silicon nanowire–reduced graphene oxide composite as a high-performance lithium ion battery anode material. *Nanoscale*, 6 (6), 3353-3360.

Ren, Y., Liu, Z., Pourpoint, F., Armstrong, A. R., Grey, C. P. and Bruce, P. G., 2012. Nanoparticulate TiO 2 (B): an anode for lithium-ion batteries. *Angewandte Chemie International Edition*, 9 (51), 2164-2167.

Rizwan, M. and Gwenin, C., 2021. Nanomaterials in renewable energy: UV-Visible spectroscopy characterization and applications. *Nano Tools and Devices for Enhanced Renewable Energy.* Elsevier, 103-120.

Rodrigues, M.-T. F., Kalaga, K., Babu, G. and Ajayan, P. M. J. E. A., 2018. Coulombic inefficiency of graphite anode at high temperature. *Electrochimica Acta,* 285, 1-8.

Sakunthala, A., Reddy, M., Selvasekarapandian, S., Chowdari, B. and Selvin, P. C., 2011. Energy storage studies of bare and doped vanadium pentoxide,(V 1.95 M 0.05) O 5, M= Nb, Ta, for lithium ion batteries. *Energy & Environmental Science*, 4 (5), 1712-1725.

Salah, M., Murphy, P., Hall, C., Francis, C., Kerr, R. and Fabretto, M., 2019. Pure silicon thin-film anodes for lithium-ion batteries: A review. *Journal of Power Sources*, 414, 48-67.

Salverda, M., Thiruppathi, A. R., Pakravan, F., Wood, P. C. and Chen, A. J. M., 2022. Electrochemical Exfoliation of Graphite to Graphene-Based Nanomaterials. *Molecules*, 27 (24), 8643.

Sasanka Hewathilake, H., Karunarathne, N., Wijayasinghe, A., Balasooriya, N. and Arof, A. J. I., 2017. Performance of developed natural vein graphite as the anode material of rechargeable lithium ion batteries. *Ionics*, 23, 1417-1422.

Sehrawat, P., Shabir, A., Julien, C. and Islam, S., 2021. Recent trends in silicon/graphene nanocomposite anodes for lithium-ion batteries. *Journal of Power Sources*, 501, 229709.

Shi, W., Zhang, Y., Key, J. and Shen, P. K., 2018. Three-dimensional graphene sheets with NiO nanobelt outgrowths for enhanced capacity and long term high rate cycling Li-ion battery anode material. *Journal of Power Sources*, 379, 362-370.

Siddiqui, S.-E.-T., Rahman, M. A., Kim, J.-H., Sharif, S. B. and Paul, S., 2022. A review on recent advancements of Ni-NiO nanocomposite as an anode for high-performance lithium-ion battery. *Nanomaterials*, 12 (17), 2930.

Sivakkumar, S. R., Nerkar, J. and Pandolfo, A., 2010. Rate capability of graphite materials as negative electrodes in lithium-ion capacitors. *Electrochimica Acta*, 55 (9), 3330-3335.

Smith, A., Stüble, P., Leuthner, L., Hofmann, A., Jeschull, F. and Mereacre, L., 2023. Potential and limitations of research battery cell types for electrochemical data acquisition. *Batteries & Supercaps*, 6 (6), e202300080.

Sole, C. G., 2017. *Application of few layer graphene and exfoliated graphite materials in lithium ion batteries*. The University of Liverpool (United Kingdom).

Sorensen, B., 2004. *Renewable energy*. Elsevier.

Stankovich, S., Dikin, D. A., Piner, R. D., Kohlhaas, K. A., Kleinhammes, A., Jia, Y., Wu, Y., Nguyen, S. T. and Ruoff, R. S. J. c., 2007. Synthesis of graphene-based nanosheets via chemical reduction of exfoliated graphite oxide. *carbon,* 45 (7), 1558-1565.

Sun, L., Liu, Y., Shao, R., Wu, J., Jiang, R. and Jin, Z., 2022. Recent progress and future perspective on practical silicon anode-based lithium ion batteries. *Energy Storage Materials*, 46, 482-502.

Sun, W., Hu, R., Liu, H., Zeng, M., Yang, L., Wang, H. and Zhu, M., 2014. Embedding nano-silicon in graphene nanosheets by plasma assisted milling for high capacity anode materials in lithium ion batteries. *Journal of Power Sources*, 268, 610-618.

Sun, W., Hu, R., Zhang, H., Wang, Y., Yang, L., Liu, J. and Zhu, M., 2016a. A long-life nano-silicon anode for lithium ion batteries: supporting of graphene nanosheets exfoliated from expanded graphite by plasma-assisted milling. *Electrochimica Acta*, 187, 1-10.

Sun, W., Hu, R., Zhang, H., Wang, Y., Yang, L., Liu, J. and Zhu, M. J. E. A., 2016b. A long-life nano-silicon anode for lithium ion batteries: supporting of graphene nanosheets exfoliated from expanded graphite by plasma-assisted milling. *Electrochimica Acta,* 187, 1-10.

Sun, Y.-K., Han, J.-M., Myung, S.-T., Lee, S.-W. and Amine, K. J. E. c., 2006. Significant improvement of high voltage cycling behavior AlF3-coated LiCoO2 cathode. *Electrochemistry communications*, 8 (5), 821-826.

Sun, Y., Liu, N. and Cui, Y., 2016c. Promises and challenges of nanomaterials for lithium-based rechargeable batteries. *Nature Energy*, 1 (7), 1-12.

Sundar, L. S., Mir, M. A., Ashraf, M. W. and Djavanroodi, F., 2023. Synthesis and characterization of graphene and its composites for Lithium-Ion battery applications: A comprehensive review. *Alexandria Engineering Journal*.

Tang, Z., Zhuang, J. and Wang, X., 2010. Exfoliation of graphene from graphite and their self-assembly at the oil− water interface. *Langmuir*, 26 (11), 9045-9049.

Tao, L., Zai, J., Wang, K., Wan, Y., Zhang, H., Yu, C., Xiao, Y. and Qian, X., 2012. 3D-hierarchical NiO–graphene nanosheet composites as anodes for lithium ion batteries with improved reversible capacity and cycle stability. *RSC advances*, 2 (8), 3410-3415.

Tarascon, J.-M. and Armand, M. J. n., 2001. Issues and challenges facing rechargeable lithium batteries. *nature*, 414 (6861), 359-367.

Tran, M.-K., DaCosta, A., Mevawalla, A., Panchal, S. and Fowler, M., 2021. Comparative study of equivalent circuit models performance in four common lithium-ion batteries: LFP, NMC, LMO, NCA. *Batteries*, 7 (3), 51.

Tuinstra, F. and Koenig, J. L. J. T. J. o. c. p., 1970. Raman spectrum of graphite. *The Journal of chemical physics*, 53 (3), 1126-1130.

Vadivel, S., Tejangkura, W. and Sawangphruk, M. J. A. o., 2020. Graphite/graphene composites from the recovered spent Zn/carbon primary cell for the high-performance anode of lithium-ion batteries. *ACS omega,* 5 (25), 15240-15246.

Valapa, R. B., Pugazhenthi, G. and Katiyar, V. J. R. A., 2015. Effect of graphene content on the properties of poly (lactic acid) nanocomposites. *Rsc Advances,* 5 (36), 28410-28423.

Vu, D.-L., Kwon, Y. J., Lee, S. C., Lee, J. U. and Lee, J.-W. J. C. L., 2019. Exfoliated graphene nanosheets as high-power anodes for lithium-ion batteries. *Carbon Letters,* 29 (1), 81-87.

Wakihara, M. J. M. S. and Reports, E. R., 2001. Recent developments in lithium ion batteries. *Materials Science and Engineering: R: Reports*, 33 (4), 109-134.

Wang, C., Kakwan, I., Appleby, A. J. and Little, F. E., 2000. In situ investigation of electrochemical lithium intercalation into graphite powder. *Journal of electroanalytical chemistry*, 489 (1-2), 55-67.

Wang, G., Shen, X., Yao, J. and Park, J., 2009. Graphene nanosheets for enhanced lithium storage in lithium ion batteries. *Carbon*, 47 (8), 2049-2053.

Wang, H.-q., Fan, X.-p., Zhang, X.-h., Huang, Y.-g., Wu, Q., Pan, Q.-c. and Li, Q.-y., 2017. In situ growth of NiO nanoparticles on carbon paper as a cathode for rechargeable Li–O 2 batteries. *RSC advances*, 7 (38), 23328-23333.

Wang, J.-Z., Zhong, C., Chou, S.-L. and Liu, H.-K., 2010. Flexible free-standing graphene-silicon composite film for lithium-ion batteries. *Electrochemistry communications*, 12 (11), 1467-1470.

Wang, J., Feng, C.-q., Sun, Z.-q., Chou, S.-l., Liu, H.-K. and Wang, J.-z. J. S. R., 2014. In-situ one-step hydrothermal synthesis of a lead germanate-graphene composite as a novel anode material for lithium-ion batteries. *Scientific Reports*, 4 (1), 1-7.

Wang, W., Tian, M., Wei, Y., Lee, S.-H., Lee, Y.-C. and Yang, R., 2013. Binder-free three-dimensional silicon/carbon nanowire networks for high performance lithium-ion battery anodes. *Nano Energy*, 2 (5), 943-950.

Wang, X., Zhang, L., Zhang, Z., Yu, A. and Wu, P., 2016. Growth of 3D hierarchical porous NiO@ carbon nanoflakes on graphene sheets for high-performance lithium-ion batteries. *Physical Chemistry Chemical Physics*, 18 (5), 3893-3899.

Whittingham, M. S. J. S., 1976. Electrical energy storage and intercalation chemistry. *Science,* 192 (4244), 1126-1127.

Writer, B. and Batteries, L.-i., 2019. a Machine-generated Summary of Current Research: Springer, Cham, Switzerland.

Wu, D., Zhao, W., Wu, H., Chen, Z., Li, H. and Zhang, L. Y., 2020. Holey graphene confined hollow nickel oxide nanocrystals for lithium ion storage. *Scripta Materialia*, 178, 187-192.

Wu, H. and Cui, Y., 2012. Designing nanostructured Si anodes for high energy lithium ion batteries. *Nano today*, 7 (5), 414-429.

Wu, J., Cao, Y., Zhao, H., Mao, J. and Guo, Z. J. C. E., 2019. The critical role of carbon in marrying silicon and graphite anodes for high-energy lithium-ion batteries. *Carbon Energy,* 1 (1), 57-76.

Wu, J. J. and Bennett, W. R., 2012. Fundamental investigation of Si anode in Li-ion cells, *2012 IEEE Energytech* (pp. 1-5): IEEE.

Wu, S., Ge, R., Lu, M., Xu, R. and Zhang, Z., 2015. Graphene-based nano-materials for lithium–sulfur battery and sodium-ion battery. *Nano Energy*, 15, 379-405.

Xiao, J., Li, Q., Bi, Y., Cai, M., Dunn, B., Glossmann, T., Liu, J., Osaka, T., Sugiura, R., Wu, B., Yang, J., Zhang, J.-G. and Whittingham, M. S., 2020. Understanding and applying coulombic efficiency in lithium metal batteries. *Nature Energy*, 5 (8), 561-568.

Xu, C., Xu, B., Gu, Y., Xiong, Z., Sun, J., Zhao, X. J. E. and Science, E., 2013. Graphene-based electrodes for electrochemical energy storage. *Energy & Environmental Science,* 6 (5), 1388-1414.

Xu, K. J. C. r., 2004. Nonaqueous liquid electrolytes for lithium-based rechargeable batteries. *Chemical reviews,* 104 (10), 4303-4418.

Xu, M., Sun, H., Shen, C., Yang, S., Que, W., Zhang, Y. and Song, X. J. N. R., 2015. Lithium-assisted exfoliation of pristine graphite for few-layer graphene nanosheets. *Nano Research*, 8, 801-807.

Yang, S., Yue, W., Huang, D., Chen, C., Lin, H. and Yang, X. J. R. A., 2012. A facile green strategy for rapid reduction of graphene oxide by metallic zinc. *Rsc Advances,* 2 (23), 8827-8832.

Yang, S., Zhuo, K., Zhang, Z., Liu, J., Bai, G. and Wang, J., 2019. Sodium fluoride-assisted hydrothermal exfoliation of graphite into graphene as filler of epoxy resin coating to protect aluminum. *The Journal of Physical Chemistry C*, 123 (45), 27969-27977.

Yao, Y.-X., Yan, C. and Zhang, Q., 2020. Emerging interfacial chemistry of graphite anodes in lithium-ion batteries. *Chemical Communications*, 56 (93), 14570-14584.

Yao, Y., McDowell, M. T., Ryu, I., Wu, H., Liu, N., Hu, L., Nix, W. D. and Cui, Y., 2011. Interconnected silicon hollow nanospheres for lithium-ion battery anodes with long cycle life. *Nano letters*, 11 (7), 2949-2954.

Yasmin, A., Luo, J.-J., Daniel, I. M. J. C. S. and Technology, 2006. Processing of expanded graphite reinforced polymer nanocomposites. *Composites Science and Technology,* 66 (9), 1182-1189.

Yazami, R. and Touzain, P. J. J. o. P. S., 1983. A reversible graphite-lithium negative electrode for electrochemical generators. *Journal of Power Sources*, 9 (3), 365-371.

Ye, M., Dong, Z., Hu, C., Cheng, H., Shao, H., Chen, N. and Qu, L., 2014a. Uniquely Arranged Graphene-on-Graphene Structure as a Binder-Free Anode for High-Performance Lithium-Ion Batteries. *Small*, 10 (24), 5035-5041.

Ye, Y.-S., Huang, Y.-J., Cheng, C.-C. and Chang, F.-C., 2010. A new supramolecular sulfonated polyimide for use in proton exchange membranes for fuel cells. *Chemical communications*, 46 (40), 7554-7556.

Ye, Y.-S., Xie, X.-L., Rick, J., Chang, F.-C. and Hwang, B.-J., 2014b. Improved anode materials for lithium-ion batteries comprise non-covalently bonded graphene and silicon nanoparticles. *Journal of Power Sources*, 247, 991-998.

Yi, M. and Shen, Z., 2016. Fluid dynamics: an emerging route for the scalable production of graphene in the last five years. *Rsc Advances*, 6 (76), 72525-72536.

Yu, Y., Chen, C. H., Shui, J. L. and Xie, S., 2005. Nickel-foam-supported reticular CoO–Li2O composite anode materials for lithium ion batteries. *Angewandte Chemie International Edition*, 44 (43), 7085-7089.

Zhang, H., Yang, Y., Ren, D., Wang, L. and He, X. J. E. S. M., 2021. Graphite as anode materials: Fundamental mechanism, recent progress and advances. *Energy Storage Materials*, 36, 147-170.

Zhang, J.-G., Wang, W., Xiao, J., Xu, W., Graff, G. L., Yang, G., Choi, D., Wang, D., Li, X. and Liu, J., 2012. Silicon-Based AnodesLi-ion battery, see also lithium-ion batterysilicon-based anodesfor Li-Ion BatteriesLi-ion battery, see also lithium-ion battery. *In:* Meyers, R. A., ed. *Encyclopedia of Sustainability Science and Technology.* New York, NY: Springer New York, 9293-9316.

Zhang, J., Zhang, L., Sun, F. and Wang, Z., 2018. An overview on thermal safety issues of lithium-ion batteries for electric vehicle application. *Ieee Access*, 6, 23848-23863.

Zhang, K., Xia, Y., Yang, Z., Fu, R., Shen, C. and Liu, Z. J. R. a., 2017. Structure-preserved 3D porous silicon/reduced graphene oxide materials as anodes for Li-ion batteries. *RSC advances,* 7 (39), 24305-24311.

Zhang, S., Ding, M. S., Xu, K., Allen, J., Jow, T. R. J. E. and Letters, S.-S., 2001. Understanding solid electrolyte interface film formation on graphite electrodes. *Electrochemical and Solid-State Letters*, 4 (12), A206.

Zhang, Y., Zhu, Y., Fu, L., Meng, J., Yu, N., Wang, J. and Wu, Y. J. C. J. o. C., 2017b. Si/C composites as negative electrode for high energy lithium ion batteries. *Chinese Journal of Chemistry*, 35 (1), 21-29.

Zhang, Z.-J., Zeng, Q.-Y., Chou, S.-L., Li, X.-J., Li, H.-J., Ozawa, K., Liu, H.-K. and Wang, J.-Z. J. E. A., 2014. Tuning three-dimensional TiO2 nanotube electrode to achieve high utilization of Ti substrate for lithium storage. *Electrochimica Acta,* 133, 570-577.

Zhang, Z., Zhang, X., You, X., Zhang, M., Walle, M. D., Wang, J., Li, Y. and Liu, Y.-N., 2016. 3D well-interconnected NiO–graphene–carbon nanotube nanohybrids as high-performance anode materials for Li-ion batteries. *Journal of Nanoparticle Research*, 18, 1-11.

Zhang, Z. J. and Ramadass, P., 2012. Lithium-ion battery systems and technology. *Batteries for Sustainability: Selected Entries from the Encyclopedia of Sustainability Science and Technology.* Springer, 319-357.

Zhao, L., Ding, B., Qin, X. Y., Wang, Z., Lv, W., He, Y. B., Yang, Q. H. and Kang, F. J. A. M., 2022. Revisiting the Roles of Natural Graphite in Ongoing Lithium-Ion Batteries. *Advanced Materials,* 34 (18), 2106704.

Zhao, R., Zhang, S., Liu, J. and Gu, J., 2015. A review of thermal performance improving methods of lithium ion battery: Electrode modification and thermal management system. *Journal of Power Sources*, 299, 557-577.

Zhao, Y., Li, X., Yan, B., Xiong, D., Li, D., Lawes, S. and Sun, X., 2016. Recent developments and understanding of novel mixed transition-metal oxides as anodes in lithium ion batteries. *Advanced Energy Materials*, 6 (8), 1502175.

Zheng, J., Di, C.-a., Liu, Y., Liu, H., Guo, Y., Du, C., Wu, T., Yu, G. and Zhu, D., 2010. High quality graphene with large flakes exfoliated by oleyl amine. *Chemical communications*, 46 (31), 5728-5730.

Zhong, M., Yan, J., Wu, H., Shen, W., Zhang, J., Yu, C., Li, L., Hao, Q., Gao, F. and Tian, Y., 2020. Multilayer graphene spheres generated from anthracite and semi-coke as anode materials for lithium-ion batteries. *Fuel processing technology*, 198, 106241.

Zhong, Y. L., Tian, Z., Simon, G. P. and Li, D., 2015. Scalable production of graphene via wet chemistry: progress and challenges. *Materials Today*, 18 (2), 73-78.

Zhou, M., Tian, T., Li, X., Sun, X., Zhang, J., Cui, P., Tang, J. and Qin, L.-C. J. I. J. E. S., 2014. Production of graphene by liquid-phase exfoliation of intercalated graphite. *International journal of electrochemical science,* 9 (2), 810-820.

Zhou, X., Cao, A.-M., Wan, L.-J. and Guo, Y.-G., 2012. Spin-coated silicon nanoparticle/graphene electrode as a binder-free anode for high-performance lithium-ion batteries. *Nano Research*, 5, 845-853.

Zhou, X., Liu, Y., Du, C., Ren, Y., Li, X., Zuo, P., Yin, G., Ma, Y., Cheng, X. and Gao, Y., 2018. Free-standing sandwich-type graphene/nanocellulose/silicon laminar anode for flexible rechargeable lithium ion batteries. *ACS applied materials & interfaces*, 10 (35), 29638-29646.

Zhu, J., Ding, Y., Ma, Z., Tang, W., Chen, X. and Lu, Y., 2022. Recent progress on nanostructured transition metal oxides as anode materials for lithium-ion batteries. *Journal of Electronic Materials*, 51 (7), 3391-3417.

Zhu, X.-J., Hu, J., Dai, H.-L., Ding, L. and Jiang, L., 2012. Reduced graphene oxide and nanosheet-based nickel oxide microsphere composite as an anode material for lithium ion battery. *Electrochimica acta*, 64, 23-28.

Zhuang, Q.-C., Qiu, X.-Y., Xu, S.-D., Qiang, Y.-H. and Sun, S.-G. J. L. I. B. N. D., 2012. Diagnosis of electrochemical impedance spectroscopy in lithium-ion batteries. *Lithium Ion Batteries—New Developments,* 8, 189-227.

Zólyomi, V., Koltai, J. and Kürti, J. J. p. s. s., 2011. Resonance Raman spectroscopy of graphite and graphene. *physica status solidi (b)*, 248 (11), 2435-2444.

Zou, Y. and Wang, Y. J. N., 2011. NiO nanosheets grown on graphene nanosheets as superior anode materials for Li-ion batteries. *Nanoscale,* 3 (6), 2615-2620.

Appendix

SEM images from hydrothermal exfoliation of graphite and Si.

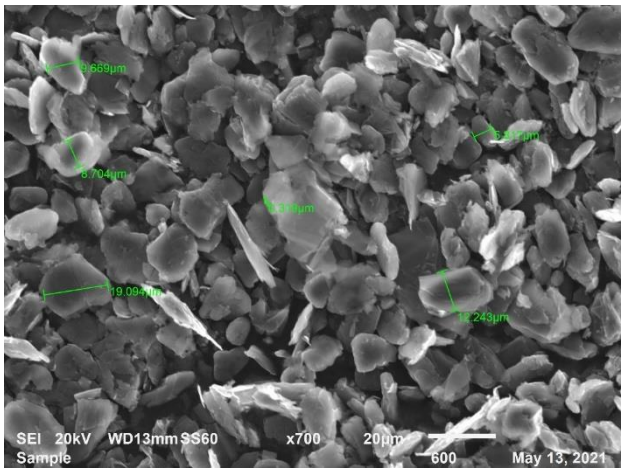

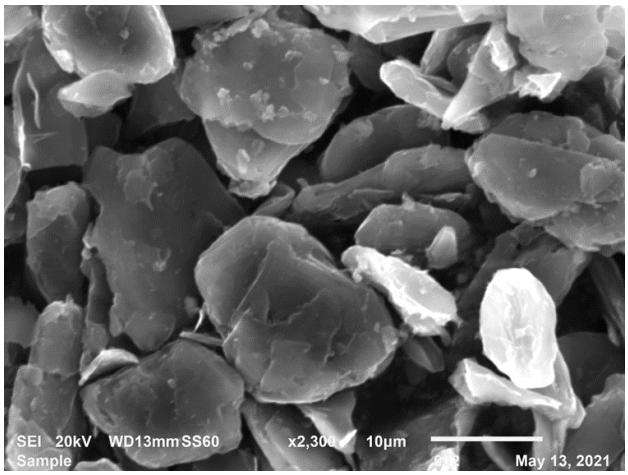

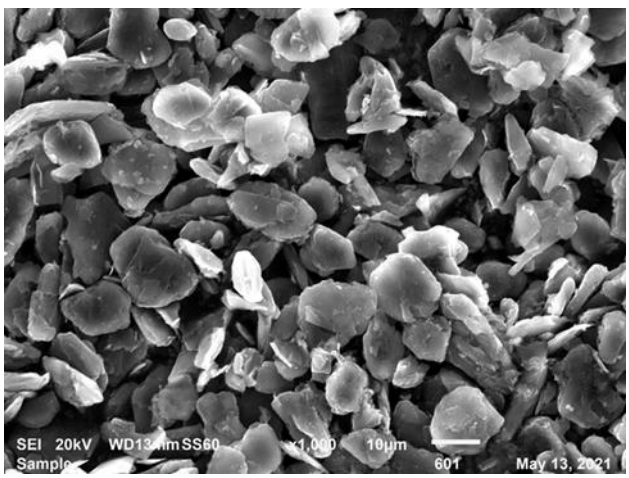

SEM images from hydrothermal exfoliated graphene.

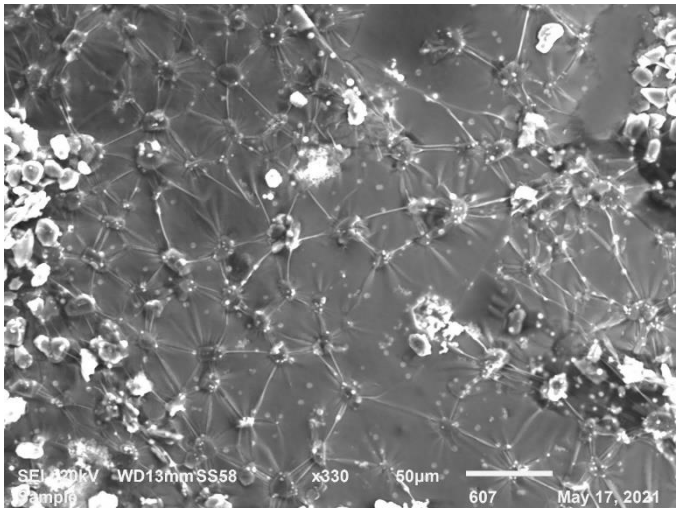

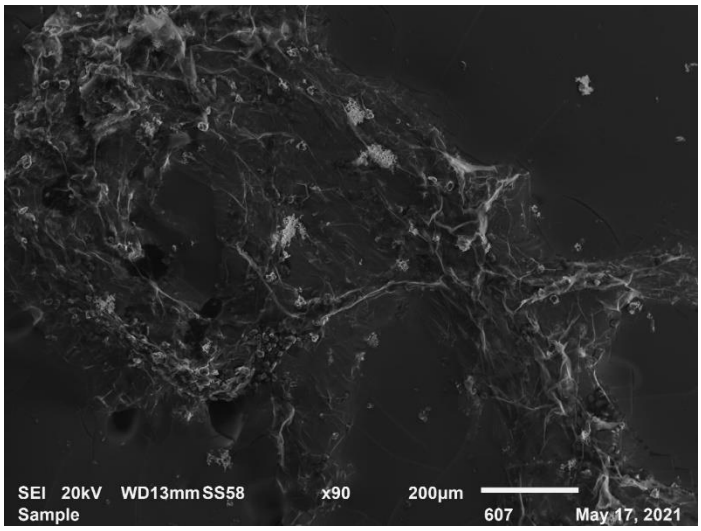

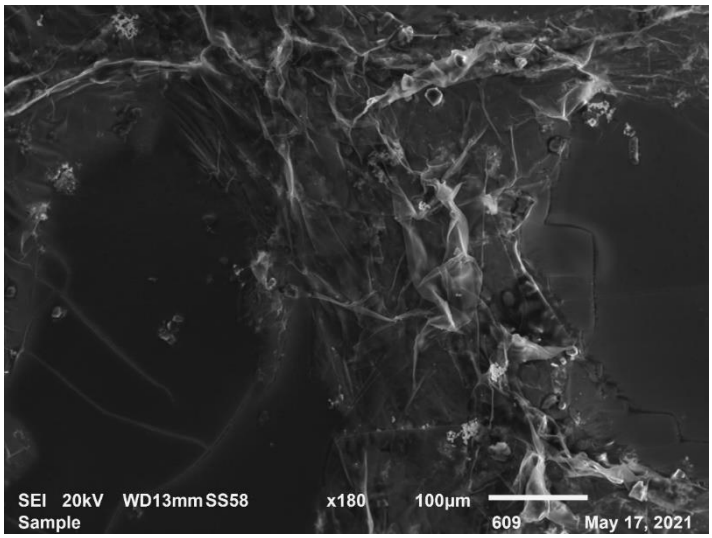

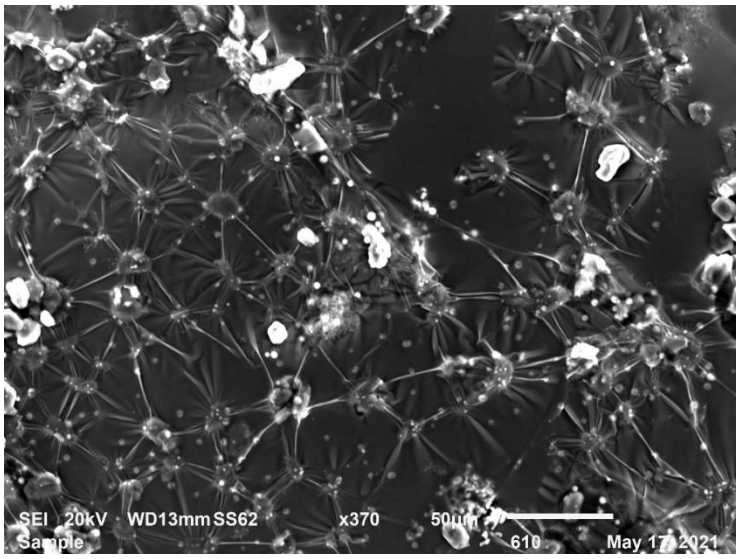

SEM images of porous Luffa

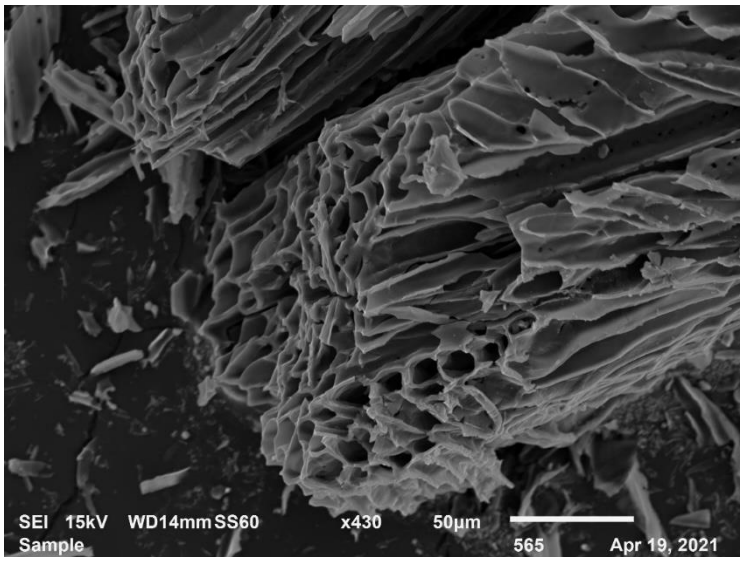

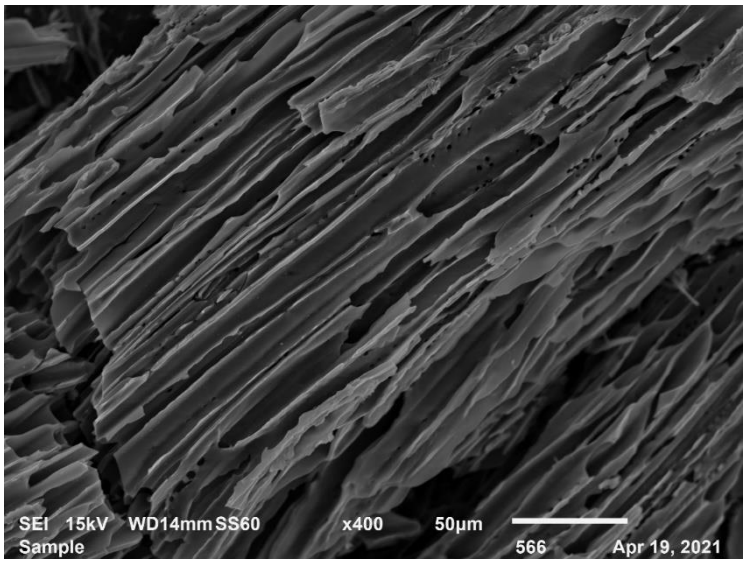


SEI 15kV WD14mm SS60 x90 200µm
Sample 563 Apr 19, 2021

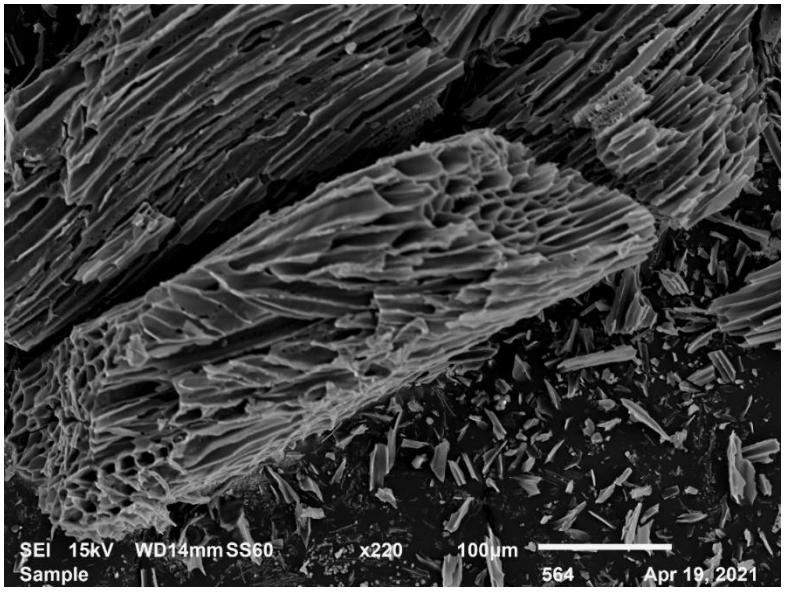
SEI 15kV WD14mm SS60 x220 100µm
Sample 564 Apr 19, 2021

SEM images of Si/graphene composite

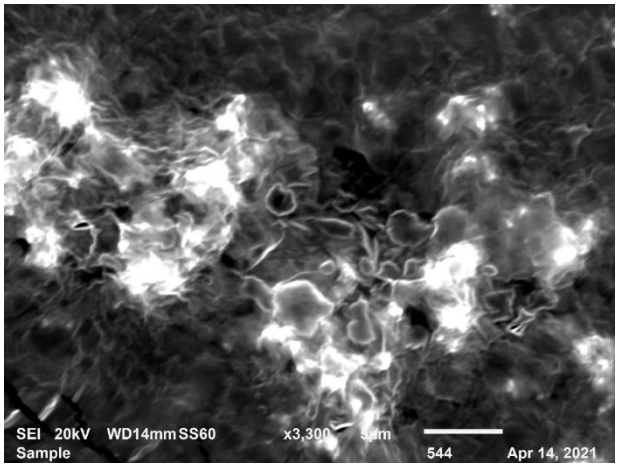

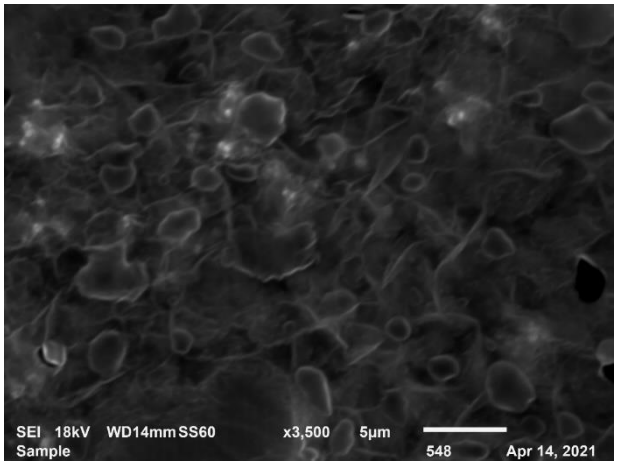

SEM images of green tea exfoliated graphene

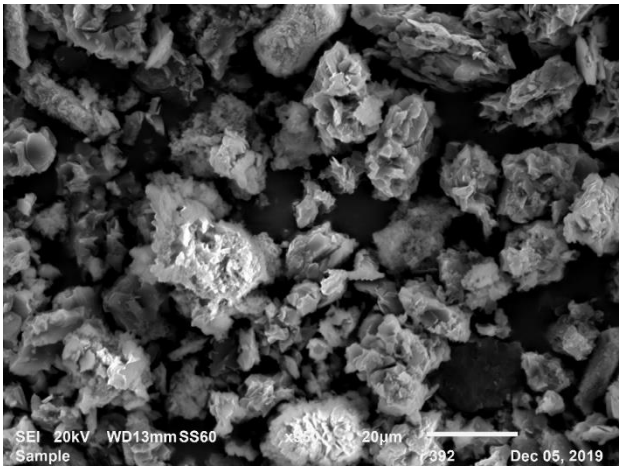

SEM images of NiO/graphene composite

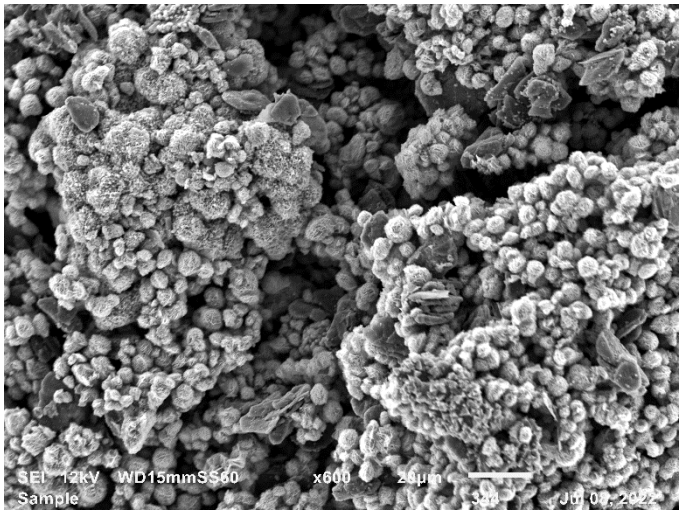

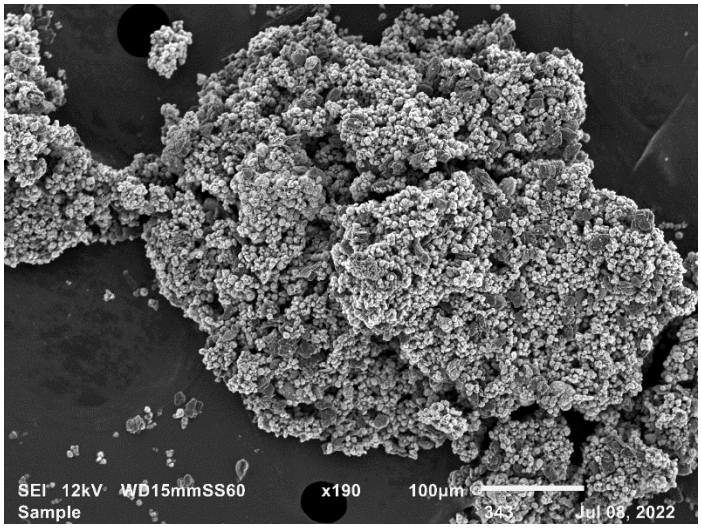

Bournemouth University

Risk Assessment Form

About You & Your Assessment

Name	Drying oven
Email	nweerahannadige@bournemouth.ac.uk
Your Faculty/Professional Service	Faculty of Science and Technology
Is Your Risk Assessment in relation to Travel or Fieldwork?	No
Status	Approved
Date of Assessment	08/11/2021
Date of the Activity/Event/Travel that you are Assessing	

What, Who & Where

Describe the activity/area/process to be assessed	Drying oven
Locations for which the assessment is applicable	DG38
Persons who may be harmed	Staff, Student

Hazard & Risk

Hazard	high temperature
Severity of the hazard	Medium
How Likely the hazard could cause harm	Medium
Risk Rating	Medium
Control Measure(s) for high temperature: The visual check is carried out prior to use and Ensures oven controls function correctly prior to use	
With your control measure(s) in place - if the hazard were to cause harm, how severe would it be? Low	
With your control measure(s) in place - how likely is it that the hazard could cause harm? Low	
The residual risk rating is calculated as: Low	
Hazard	Fire and burns

Severity of the hazard	Medium
How Likely the hazard could cause harm	Medium
Risk Rating	Medium

Control Measure(s) for Fire and burns:

Personal protective equipment (PPE) is used as necessary

Control of material placed in oven

With your control measure(s) in place - if the hazard were to cause harm, how severe would it be? Low

With your control measure(s) in place - how likely is it that the hazard could cause harm? Low

The residual risk rating is calculated as: Low

Review & Approval

Any notes or further information you wish to add about the assessment	
Names of persons who have contributed	
Approver Name	Amor Abdelkader
Approver Job Title	Associate Professor
Approver Email	aabdelkader@bournemouth.ac.uk
Review Date	08/11/2021

Uploaded documents

No document uploaded

Bournemouth University

Risk Assessment Form

About You & Your Assessment

Name	Niranjala
Email	nweerahannadige@bournemouth.ac.uk
Your Faculty/Professional Service	Faculty of Science and Technology
Is Your Risk Assessment in relation to Travel or Fieldwork?	No
Status	Approved
Date of Assessment	16/05/2023
Date of the Activity/Event/Travel that you are Assessing	

What, Who & Where

Describe the activity/area/process to be assessed	Electrodes casting, coin cell assembling and testing using a battery tester
Locations for which the assessment is applicable	PG71b
Persons who may be harmed	Staff, Student

Hazard & Risk

Hazard	Electric hazard from the cables if short circuit
Severity of the hazard	Low
How Likely the hazard could cause harm	Medium
Risk Rating	Low
Control Measure(s) for Electric hazard from the cables if short circuit: set a control current on the potentiostat/power supply, preferably under 0.5 A	
With your control measure(s) in place - if the hazard were to cause harm, how severe would it be? Low	
With your control measure(s) in place - how likely is it that the hazard could cause harm? Low	
The residual risk rating is calculated as: Low	
Hazard	LiPF6 organic electrolyte

Severity of the hazard	Medium
How Likely the hazard could cause harm	Medium
Risk Rating	Medium

Control Measure(s) for LiPF6 organic electrolyte :

handle the electrolyte in glove box

Should wear protective gloves and lab coats

With your control measure(s) in place - if the hazard were to cause harm, how severe would it be? Low

With your control measure(s) in place - how likely is it that the hazard could cause harm? Low

The residual risk rating is calculated as: Low

Hazard	working alone in the lab
Severity of the hazard	Low
How Likely the hazard could cause harm	Low
Risk Rating	Low

Control Measure(s) for working alone in the lab:

obtained the proper training and experience (i have been working in the lab for now 2 years and I am well experienced with the proposed lab work here)

check-in times with Poole House reception and Resource Assistant, Duncan Hall

With your control measure(s) in place - if the hazard were to cause harm, how severe would it be? Low

With your control measure(s) in place - how likely is it that the hazard could cause harm? Low

The residual risk rating is calculated as: Low

Hazard	COVID-19
Severity of the hazard	High
How Likely the hazard could cause harm	High
Risk Rating	High

Control Measure(s) for COVID-19 :

Frequent hand washing using soap and hot water

Follow catch it, Bin it, kill it using crook of elbow or tissues when coughs and sneezes and avoid touching face, eyes, nose or mouth with unclean hands

Wearing of face-covering with three-layer construction. FFP2 masks when 2m social distancing cannot be maintained

Maintain 2-metre social distancing

Conduct two rapid lateral flow device (LFD) tests per week in university prior to the lab

When possible have increased ventilation in the lab Frequently clean and disinfect equipment, tools and surfaces before and after use using provided 70% IPA wipes or 70% IPA on blue roll tissue
With your control measure(s) in place - if the hazard were to cause harm, how severe would it be? Medium
With your control measure(s) in place - how likely is it that the hazard could cause harm? Medium
The residual risk rating is calculated as: Medium

Review & Approval

Any notes or further information you wish to add about the assessment	
Names of persons who have contributed	
Approver Name	Dr Amor Abdelkader
Approver Job Title	Associate Professor In Advanced Materials
Approver Email	aabdelkader@bournemouth.ac.uk
Review Date	16/05/2024

Uploaded documents

No document uploaded

Bournemouth University

Risk Assessment Form

About You & Your Assessment

Name	Niranjala
Email	nweerahannadige@bournemouth.ac.uk
Your Faculty/Professional Service	Faculty of Science and Technology
Is Your Risk Assessment in relation to Travel or Fieldwork?	No
Status	Approved
Date of Assessment	16/05/2023
Date of the Activity/Event/Travel that you are Assessing	

What, Who & Where

Describe the activity/area/process to be assessed	Scanning electron Microscope
Locations for which the assessment is applicable	DG
Persons who may be harmed	Staff, Student

Hazard & Risk

Hazard	Emission of X-rays from electron microscope
Severity of the hazard	Medium
How Likely the hazard could cause harm	Medium
Risk Rating	Medium

Control Measure(s) for Emission of X-rays from electron microscope:

Use by registered and trained staff and users only.

Microscope is completely shielded to avoid X-ray emission

The microscope is monitored frequently by service engineers

With your control measure(s) in place - if the hazard were to cause harm, how severe would it be? Low

With your control measure(s) in place - how likely is it that the hazard could cause harm? Low

The residual risk rating is calculated as: Low

Hazard	High voltage
Severity of the hazard	Medium
How Likely the hazard could cause harm	Medium
Risk Rating	Medium

Control Measure(s) for High voltage :

should use by trained staff and users only

The microscope is completely shielded and should carry out all imaging in vacuum mode

should wear Lab coats, gloves, and safety eyewear

Don't leave the microscope with the filament on

Any modification of microscope is strictly forbidden

With your control measure(s) in place - if the hazard were to cause harm, how severe would it be? Low

With your control measure(s) in place - how likely is it that the hazard could cause harm? Low

The residual risk rating is calculated as: Low

Review & Approval

Any notes or further information you wish to add about the assessment	
Names of persons who have contributed	
Approver Name	Amor Abdelkader
Approver Job Title	Associate Professor
Approver Email	aabdelkader@bournemouth.ac.uk
Review Date	

Uploaded documents

No document uploaded

Bournemouth University

Risk Assessment Form

About You & Your Assessment

Name	Niranjala
Email	nweerahannadige@bournemouth.ac.uk
Your Faculty/Professional Service	Faculty of Science and Technology
Is Your Risk Assessment in relation to Travel or Fieldwork?	No
Status	Approved
Date of Assessment	01/11/2021
Date of the Activity/Event/Travel that you are Assessing	

What, Who & Where

Describe the activity/area/process to be assessed	Vertical furnace, molten salt graphite exfoliation at high temperature
Locations for which the assessment is applicable	PG71b
Persons who may be harmed	Staff, Student

Hazard & Risk

Hazard	Burns to hands with contact with hot oven/furnace or heated material
Severity of the hazard	Medium
How Likely the hazard could cause harm	Medium
Risk Rating	Medium
Control Measure(s) for Burns to hands with contact with hot oven/furnace or heated material: Use of thermal gloves, lab coats, safety goggles, cover feet	
With your control measure(s) in place - if the hazard were to cause harm, how severe would it be? Low	
With your control measure(s) in place - how likely is it that the hazard could cause harm? Low	
The residual risk rating is calculated as: Low	

Review & Approval

Any notes or further information you wish to add about the assessment	
Names of persons who have contributed	
Approver Name	Dr Amor Abdelkader
Approver Job Title	Associate Professor In Advanced Materials
Approver Email	aabdelkader@bournemouth.ac.uk
Review Date	

Uploaded documents

No document uploaded